Università degli Studi di Napoli Federico II

Ph.D. Thesis in

Information Technology and Electrical Engineering

Dynamics of coupled mechanical oscillators with friction

Christian Erazo Ordoñez

Tutor: Prof. Mario Di Bernardo

XXIX Ciclo

Acknowledgments

Although this Thesis is related to the scientific part of my PhD, this section is dedicated to the people that make it happen. First of all, I would thank to my supervisor Prof. Dr. Mario Di Bernardo by his confidence and constant encouraging words that allowed me to complete my research. His constructive comments and feedbacks at group meeting sessions were instrumental in my academic formation. Thanks to my colleagues and friends at SIN-CRO research group who made my stay in Napoli enjoyable and happy.

The invitation of Prof. Martin Homer to visit the Department of Engineering Mathematics, University of Bristol, gave me the opportunity to discover many valuable topics and to meet outstanding researchers at the seminaries of the research group, I feel particularly grateful for this. Special thanks to Prof. M. Homer for his valuable suggestions and feedbacks about the results of Chapter 3 and Chapter 4, his support was valuable in the development of this Thesis. I would also like to thank Dr. Petri Piiroinen at the University of Ireland, Galway for the fruitful discussions about the numerical complexity in simulating piecewise smooth systems.

I would like to thank the members of my doctoral evaluation committee; Prof. Josep M. Olm and Prof. Gerard Olivar Tost for their constructive comments and remarks that have improved the quality of this Thesis. I would also like to thank my former Professors and colleagues at the Percepción y Control Inteligente PCI research group at Universidad Nacional de Colombia, for providing me their friendship and encourage me to pursue my doctoral studies. Especially, to my former supervisor Prof. Dra. Fabiola Angulo Garcia, whose lectures of classical control inspired me and triggered my passion for the research in the area of Dynamical Systems and Control.

I would like to thank to my family, Nestor Patricia Lisney and David for their love, support and encouragement, and my girlfriend Claudia for her love and patience. The long-time friendship from Dr. Daniel Burbano is a big part of the reason why my doctoral studies started, and for this I am forever indebted.

Contents

List of Figures

List of Tables

■

ix

Abstract

Complex phenomena such as stick-slip vibrations, chaos and self-organized dynamics are frequently encountered in several mechanical systems with friction. Some applications include control of robot manipulators, distribution of earthquakes, suspension dynamics in vehicles, among others. These systems are strongly nonlinear. Spring-mass oscillators with friction have emerged as a simple jet effective model capturing the dynamics of much more complex system. In this dissertation, we study stability and dynamics of single and coupled mechanical oscillators with friction, mathematically described by differential equations with discontinuous right-hand sides. One particular problem in discontinuous systems is the computation of the basins of attraction of their stable equilibria or other attractors ; for example, they provide important information about complex behavior caused by friction or damping, useful in the design of mechanical devices. To cope with this problem, we implemented an algorithm for the computation of basins of attraction in discontinuous systems based on the Simple Cell Mapping method, which has been evaluated via a set of representative applications. In the second part of the thesis, a piecewise smooth analysis of two coupled oscillators was carried out, finding out some conditions that guarantee the stability of the sliding dynamics in the presence of one or more intersecting surfaces. Finally, the dynamics of a network of N mechanical oscillators was studied from the point of view of synchronization, where the goal was to steer the positions and velocities of each oscillator in the network towards a common behavior. In particular, an extensive numerical analysis for studying synchronization in chaotic friction oscillators was performed, characterizing the influence of dynamic coupling and providing an estimation of the synchronization region in terms of the coupling parameters. Initially, we considered the simple case of two coupled oscillators, then we extended the analysis to the case of larger networks of coupled systems with different network topologies. Moreover, preliminary analytical results of the convergence on a network of N friction oscillators based on contraction analysis are investigated. The results were also validated through a representative example.

Introduction

Switching dynamics arise in wide-ranging applications, relays in electronic circuits [90], friction in mechanical systems [76], biochemical valves in biological systems [84]. Stick-slip vibrations excited by friction are a common phenomenon underlying the behavior of several mechanical systems, for example in drill-string systems [61, 73], electromechanical systems [90], earthquake models [39, 40], and many more. These vibrations are typically harmful and undesirable, especially in extreme cases when they can result in the destruction of the vibrating object. In contrast, there are situations in which one wants high friction as in clutches and brakes.

These classical examples have been studied within the theory of piecewise smooth systems PWS, where the smooth evolutions are modeled by sets of differential equations while thresholds and abrupt changes are modeled as discontinuity surfaces [24, 37]. The solutions of such PWS systems are understood in the sense of Filippov [37], who suggested to replace the PWS system with a suitable differential inclusion. The resulting method is known as Filippov convexification.

The computation of the basins of attraction of Filippov systems is a very relevant problem in applications; for example, it provides useful information about complex behavior caused by friction impacts or damping, in the design of mechanical devices [71, 70, 100]. In the context of control theory, the problem of computing basins of attraction (or regions of asymptotic stability) in such systems is often addressed by Lyapunov methods, where regions of attraction are estimated as sublevel sets of a given Lyapunov function; see e.g. [23, 46]. However, Lyapunov methods provide conservative results meaning that the computed region is smaller

than the exact basin of attraction.

Cell mapping methods (CM) provide a computationally efficient way to analyze the long term behavior of dynamical systems [47]. Their key characteristic is the approximation of the continuous state space via a discrete array of cells known as *cell-state space*. Then, a cell-to-cell map is created by performing short-time integrations, from the center of each cell, to the cell which contains the endpoint of the trajectory. The first cell mapping method presented in the literature is the *Simple Cell Mapping* (SCM) [47], which has been the basis for many cell mapping methods developed in the following years [95, 87]. Some modifications to cell mapping methods allow the computation of basins in discontinuous systems. In [96] a numerical study of an impact-friction oscillator is performed via interpolated cell mapping (ICM), where an event divergent cell is included in order to detect the grazing boundary. Other cell mapping techniques consider the switching surface, i.e. the manifold where the vector field is not differentiable, as the Poincaré mapping surface for computing basins of periodic orbits [94, 12, 42]. Basins of attractions of mechanical systems have also been computed via cell mapping applications by using discrete maps instead of direct numerical integrations [71, 43].

Fewer results using cell mapping methods have been reported in discontinuous systems with sliding solutions, mainly due to the fact that standard integration routines are inaccurate or inefficient, or both, in the region where discontinuities in the derivatives occur. For example, a possible source of numerical problems is the presence of small oscillations around the discontinuity boundary (numerical chattering) that may arise during sliding. A disadvantage of existing algorithms based on cell-to-cell mapping is the fact that the region of interest is pre-defined by the user which implies that extra computations are required if it is desired to explore a different region of state space. Parallel processing capabilities of modern architectures have also been exploited, in the case of smooth and high order systems to consider different cell dimensions and several refinement stages within cell mapping methods [59, 9]. However these techniques have not been extended, as far as we are aware, for discontinuous systems.

Another interesting problem is to understand the dynamics of systems with multiple switches. In the case of a single discontinuity manifold of co-dimension 1, Filippov methodology has provided a widely accepted mathematical framework to understand the dynamics on the discontinuity surface [24, 18]. However when, we consider high order discontinuity surfaces

an ambiguity arises in the construction of the sliding vector field. This problem has been extensively studied see for example [50, 30, 28]. In the case of Filippov systems of co-dimension 2, there exist in the literature two systematic proposal to avoid the ambiguity in the Filippov convex method, they are the *bilinear combination* [1] and a recent approach called the *moments method* [29]. A nonlinear formulation to construct the sliding vector field called the *Hidden dynamics* has been presented in [51]. This formulation has shown to be effective in modeling real mechanical phenomena like stiction, not captured by applying Filippov's method [52, 53, 54]. In [75] the authors investigate how the regularization of the discontinuous systems can be extended to the nonlinear sliding vector fields, while in [54] and [53] the authors perform an analysis of bifurcation of the hidden dynamics and also illustrate the strange effects induced by the nonlinear dynamics.

Switching systems have also been studied from the point of view of synchronization, where the goal is that all states of each agent in the network, converge towards each other. Examples of networks of piecewise dynamical systems can be found in biochemical reactions [88], power grids [32] and arrays of mechanical oscillators with friction [93]. It is therefore of great importance to derive conditions to guarantee synchronization in networks of discontinuous systems. Currently, most of the literature focuses on networks with switching topologies [101, 80]. The problem of considering networks in which each agent is described by piecewise system is challenging and some preliminary results have been proposed in the literature [20, 82, 78, 64].

The aim of this thesis is to study the dynamics of systems with discontinuous vector fields, taking as an example the case of coupled friction oscillators. Indeed, mechanical systems with friction constitute an important example of discontinuous systems and therefore they are used as key applications throughout this thesis. To deal with the problem of computing basins of attraction we extend the cell mapping method for computing basins of attraction in systems with sliding. Moreover, we exploit the hidden dynamics approach [51] for modeling stiction friction in two coupled friction oscillators. Finally, the synchronization in networks of mechanical oscillators with friction is analyzed via extensive numerical simulations.

1.0.1 Thesis outline

Chapter 2 introduces linear and nonlinear sliding Filippov solutions, together with the method of regularization of PWS dynamical systems. We also explain the basic concepts of contraction theory for smooth systems and a extension to the case of bimodal Filippov systems. Finally, we provide a brief introduction of the synchronization problem in coupled

networks with diffusive coupling.

Chapter 3 introduces a numerical tool for computing basins of attraction in Filippov systems. An extension of the simple cell mapping algorithm for planar Filippov systems is presented, detailing how the grid is selected and describing the numerical integration method used for dealing with sliding motions. The effectiveness of the algorithm is shown by computing the basins of attraction of a sliding control problem and a mechanical system with dry friction.

In Chapter 4, a piecewise smooth analysis of two coupled mechanical oscillators subjected to dry friction is addressed. We make use of nonlinear sliding vector fields to model stiction friction force in systems with two discontinuity surfaces. This analysis provide a full characterization of the nonlinear siding dynamics of co-dimension 1 and higher order sliding modes, and more importantly the ambiguity in selecting the nonlinear sliding vector field in the co-dimension 2 surface is resolved by using the regularization approach.

In Chapter 5 we study the synchronization phenomena in networks of mechanical systems with friction coupled dynamically through different topologies. The effect of regularization in the synchronization of networks of friction oscillators is discussed. Preliminary results of the convergence of a network of N friction oscillators along with an example validating the obtained results are presented. The conclusions are drawn in Chapter 6.

The results of Chapter 3 were obtained in collaboration with Dr. Martin Homer (Department of Engineering Mathematics,University of Bristol, Uk) and Dr. Petri Piiroinen (School of Mathematics, Statistics and Applied Mathematics, National University of Ireland, Galway, Ireland) and were partially presented in [15] and are extended in [34]. The results in Chapters 4 have been developed together with Prof. Martin Homer and Emmanuel Lorenzano (University of Bologona) and will be reported in [35] (in preparation).

Preliminaries and Background

We provide some the definitions of important classes of dynamical systems that will be analyzed in the thesis.

2.1 Piecewise systems

Following [24] p.73, we define a piecewise smooth dynamical system as follows.

Definition 2.1.1. *A dynamical system $\dot{x} = f(t, x)$, with $f : [t_0, +\infty) \times D \mapsto \mathbb{R}^n$, is called a piecewise smooth dynamical system (PWS) when it is defined by a set of ODEs*

$$\dot{x} = f_i(t, x), \qquad x \in R_i, i = 1, \dots, n. \tag{2-1}$$

where $\cup_i R_i = D \subset \mathbb{R}^n$ and each R_i has non-empty interior. The intersection $\Sigma_{ij} = \bar{R}_i \cap \bar{R}_j$ is either an $\mathbb{R}^{n-1}$-dimensional manifold included in the boundaries ∂R_j and ∂R_i, or is the empty set. Each vector field f_i is smooth in both the state x and the time t for any $x \in R_i$. Furthermore, each $f_i(t, x)$ is continuously extended on the boundary ∂R_i.

Piecewise smooth dynamical systems can exhibit complex behaviors that do not appear in smooth systems, [24, 55, 11, 91]. A notable example is that of sliding mode solutions in which the evolution of the PWS dynamical system belongs to the zero-set of a scalar function $h(x) : \mathbb{R}^n \mapsto \mathbb{R}$ (the so-called Filippov systems, see e.g. [37, 90]).

Two approaches exist in literature for the description of the dynamics at the discontinuity boundary. These are Utkin equivalent control method [90] and Filippov convex method [37]. In this section, we provide a general definition of sliding dynamics for multimodal systems (i.e. PWS systems with $i = 1, \dots, r$ switching surfaces). The following definition is

closely related to the equivalent control method [90]. Notice that continuously differentiable dynamical systems are also piecewise smooth systems, however in this thesis we consider discontinuous dynamical systems.

2.1.1 Bimodal piecewise smooth systems

A brief characterization of bimodal piecewise systems is given below. We assume that the state space consists of two regions $R_1 \subset \mathbb{R}^n$ and $R_2 \subset \mathbb{R}^n$ separated by a discontinuity surface Σ defined as a zero set of a smooth scalar function $h(x) : \mathbb{R}^n \mapsto \mathbb{R}$. A bimodal piecewise smooth system is then described as

$$\dot{x} = f(x, s_1) = \begin{cases} f_1(x) & \text{for} \quad x \in R_1, \\ f_2(x) & \text{for} \quad x \in R_2, \end{cases} \tag{2-2}$$

where $f_1(x) : \mathbb{R}^n \mapsto \mathbb{R}^n$ and $f_2(x) : \mathbb{R}^n \mapsto \mathbb{R}^n$ are smooth vector fields. The regions R_1, R_2 and the switching manifold Σ are expressed by

$$R_1 = \{x \in \mathbb{R}^n : h(x) > 0\}, \; R_2 = \{x \in \mathbb{R}^n : h(x) < 0\}, \tag{2-3}$$

$$\Sigma = \{x \in \mathbb{R}^n : h(x) = 0.\} \tag{2-4}$$

If the vector fields f_1 and f_2 both point towards the switching manifold Σ at any given point, the dynamics are locally constrained to the surface $h(x)$, and the motion on Σ is said to be sliding. The open subset $\widehat{\Sigma} \subset \Sigma$ where the vector fields are both pointing towards Σ is often referred to as the *sliding surface*, which is attractive if

$$\mathcal{L}_{f_1 - f_2}(h)(x) < 0, \quad x \in \widehat{\Sigma}, \tag{2-5}$$

and repelling if

$$\mathcal{L}_{f_1 - f_2}(h)(x) > 0, \quad x \in \widehat{\Sigma}. \tag{2-6}$$

Here, $\mathcal{L}_f h(x) := \nabla h(x) \cdot f(x)$ is the *Lie derivative* of $h(x)$ with respect to the vector field f. According to Definition 2.1.2, the dynamical system (2-2) can be extended to include the vector field on the sliding surface such that

$$\dot{x} = f_\Sigma(x), \quad x \in \widehat{\Sigma}, \tag{2-7}$$

where

$$f_\Sigma(x) = \frac{f_1(x) + f_2(x)}{2} + \frac{f_1(x) - f_2(x)}{2} s_1(x), \tag{2-8}$$

and $-1 \leq s_1(x) \leq 1$. Since the motion is constrained to $\widehat{\Sigma}$, f_Σ must be tangent to $\widehat{\Sigma}$, i.e. $\mathcal{L}_{f_\Sigma}(h)(x) = 0$, which yields

$$s_1(x) = -\frac{\mathcal{L}_{f_1+f_2}(h)(x)}{\mathcal{L}_{f_1-f_2}(h)(x)}. \tag{2-9}$$

We can now define the sliding surface as

$$\widehat{\Sigma} = \{x \in \Sigma : |s_1(x)| < 1\}, \tag{2-10}$$

with boundaries

$$\partial\Sigma^+ = \{x \in \Sigma : s_1(x) = 1\}, \quad \partial\Sigma^- = \{x \in \Sigma : s_1(x) = -1\}. \tag{2-11}$$

From the geometric point of view, the procedure of finding the sliding equations consist in to direct the velocity vector in the system state space along the discontinuity surface or the intersection of discontinuity surfaces in multimodal systems, as shown in Figure **2-1**.
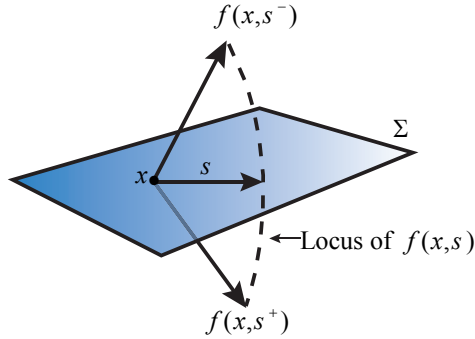
Figure 2-1: Sliding vector field, for a given a point x on the switching surface, with vector fields $f(x, s^+)$, $f(x, s^-)$ pointing to that point.

2.1.2 Multimodal piecewise smooth systems

Definition 2.1.2. *Consider the multimodal piecewise smooth dynamical system*

$$\dot{x} = f(x, s(h)), \quad s_i = \text{sgn}(h_i(x)), \tag{2-12}$$

for some $i = 1, 2, \ldots, r$, where f is a vector field with smooth dependence on the variables $x = (x_1, x_2, \ldots, x_n)$, $s = (s_1, s_2, \ldots, s_r)$ is a vector of switching parameters and $h(x) = (h_1(x), h_2(x), \ldots, h_r(x))$ is a vector of the scalar functions. Then if there exist some $s^* \in [-1, +1]$ that solves

$$\begin{cases} \vec{0}_n = Dh(x) \cdot f(x, s^*) \\ \vec{0}_r = h(x), \end{cases} \tag{2-13}$$

with $Dh(x) = \frac{\partial h}{\partial x}$, then the system

$$\dot{x} = f_\Sigma(x) = f(x, s^*), \tag{2-14}$$

defines the sliding modes of (2-12). Moreover, if $f(x, s)$ depends linearly on s, we call these linear sliding modes, while if s is nonlinear, they are nonlinear sliding modes.

For later use, we adopt the notation f_2 and f_1 to simply denote the set of points for which we have $h(x) < 0$ and $h(x) > 0$, respectively.

2.2 Hidden dynamics

The term *hidden dynamics* introduced in [51], refers to what happens on Σ, specifically to behaviors governed by nonlinear set-valued terms (i.e. terms with a nonlinear dependence of s) that disappear outside the switching manifold Σ hence they are *hidden* in (2-2). In particular, in [51] it was shown that the use of nonlinear set-valued dynamics on the discontinuity surface $h(x) = 0$, introduces multiple sliding modes, extending the sliding surface over the crossing regions. Considering the bimodal PWS systems (2-2), the sliding equations under the hidden dynamics approach reads

$$\dot{x} = f_\Sigma^{nl} = \frac{1}{2}\left[1 + s_1\right] f_1(x) + \frac{1}{2}\left[1 - s_1\right] f_2(x) + G(s_1)\gamma(s_1), \quad \text{for} \quad x \in \Sigma. \tag{2-15}$$

where $G(s_1)$ is any nonlinear function in s_1 and $\gamma(s_1)$ satisfies

$$\gamma(s_1) \in \left\{ \begin{array}{ccc} 0 & \text{if} & |s_1| = 1 \\ [0, 1] & \text{if} & |s_1| < 1 \end{array} \right.. \tag{2-16}$$

Some examples of $\gamma(s_1)$ that satisfy (2-16) are $(1 - s_1{}^2)$, $\sin(1 - s_1{}^2)$, or $1 - s_1{}^{2l}$ for any natural number l. Clearly, according to the Definition 2.1.2, equation (2-15) provides multiple solutions for s_1^*, and each one defines a different sliding mode on $h(x) = 0$. To determine if such dynamics are attractive or repellent, we can check whether the trajectories outside of $h(x)$ converge toward the sliding surface or not. This can be evaluated through the following relation

$$z(x, s_1) := \frac{\partial}{\partial s_1}(f(x, s_1) \cdot \nabla h(x)) < 0 \tag{2-17}$$

where (2-15) is attracting if $z(x, s)$ is negative, and repelling if $z(x, s)$ is positive. Places where there exists solutions to (2-13) define regions where the vector field f is tangent to Σ

for one or more values of s_1^*, allowing the flow slides along Σ, as shown in Figure **2-2**. The nonlinear sliding region is given by

$$\widehat{\Sigma}^{nl} = \left\{ x \in \Sigma : f(x, s_1) \cdot \nabla h(x) \neq \vec{0} \right\}. \tag{2-18}$$

Places where (2-13) has no solutions define the nonlinear crossing regions,

$$\Sigma^{nc} = \left\{ x \in \Sigma : f(x, s_1) \cdot \nabla h(x) = \vec{0} \right\}. \tag{2-19}$$

such that, $\Sigma = \widehat{\Sigma}^{nl} \cup \Sigma^{nc}$.

(a)   (b)
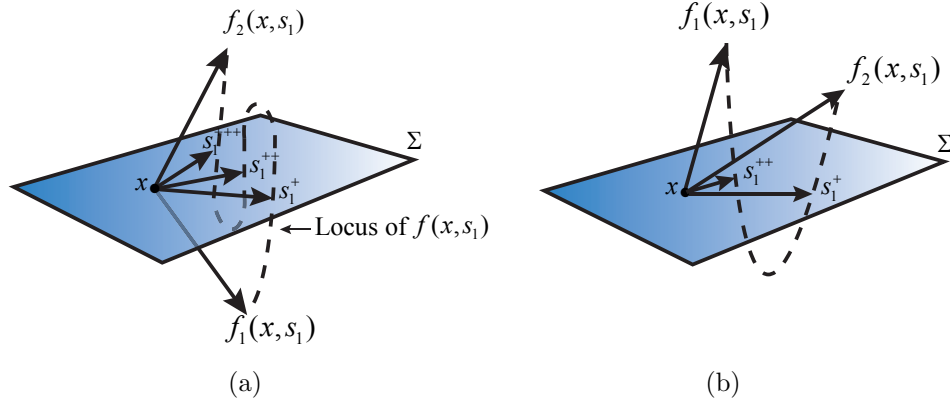
Figure 2-2: Nonlinear sliding dynamics. Panel (a) illustrates multiple sliding modes $f(x, s_1^+)$, $f(x, s_1^++)$ and $f(x, s_1^++)$, provided by a cubic polynomial function in s_1. "Forced" sliding dynamics along a crossing region is shown in panel (b).

2.2.1 Regularization of PWS systems: slow-fast analysis

One way of studying the sliding dynamics equations is to model the discontinuity as the limit of a boundary layer i.e. $|h(x)| \leq \varepsilon$, with $\varepsilon > 0$ being a small parameter. In [85, 65] it has been shown that the dynamics of (2-7) persist when the discontinuity is regularized by a class of transition functions $\Phi : \mathbb{R} \mapsto \mathbb{R}$. Recently, in [75] regularization analysis was extended to nonlinear sliding modes, specially the authors show that the regularization of the nonlinear sliding dynamics (2-15) also exhibits slow invariant dynamics that recovers the dynamics of the discontinuous system (2-8).

In this section, we introduce the regularization of PWS (2-2) via the slow-fast systems [60]. Let us consider the regularized version of (2-2),

$$\dot{x} = f(x, s(h(x)/\varepsilon)). \tag{2-20}$$

By setting $z = h(x)/\varepsilon$ the system (2-20) becomes

$$\dot{x} = f(x, s(z))$$
$$\varepsilon \dot{z} = \nabla h(x)^T \cdot f(x, s(z)), \tag{2-21}$$

where the variable z is called the *fast variable* while x is said to be the *slow variable*. System (2-21) is called slow-system since it is expressed in terms of the derivative of slow times scale $\dot{()} = d/dt$. Now if we denote the derivative with respect to the fast time scale as $()' = d/d\tau$ where $\tau = t/\varepsilon$, we get the fast system

$$x' = \varepsilon f(x, s(z))$$
$$z' = f(x, s(z)) \cdot \nabla h(x). \tag{2-22}$$

To determine the stability of system (2-21)-(2-22) we need to study the limiting dynamics of the slow-fast system, in doing so, by setting $\varepsilon = 0$, the limiting dynamics are given by

$$\dot{x} = f(x, s(z))$$
$$0 = f(x, s(z)) \cdot \nabla h(x), \tag{2-23}$$

known as the *reduced model* while

$$x' = 0$$
$$z' = f(x, s(z)) \cdot \nabla h(x) \tag{2-24}$$

is known as the *boundary layer model*. The set $\mathbb{C} = \{(x, z) : \nabla h(x) \cdot f(x, s(z)) = 0\}$ is called the *critical manifold*, and its elements are in one-to-one correspondence with the equilibrium points of the boundary layer model (2-24). These equilibrium points are normally hyperbolic if

$$\frac{d}{ds} \left(\nabla h(x) \cdot f(x, s) \right) \neq 0 \tag{2-25}$$

Notice that, the boundary layer model coincides with the sliding dynamics (2-13) for $r = 1$. We conclude this section with an example contrasting the linear and nonlinear sliding modes.

2.2.1.1 Example

Let us consider the second order system

$$\dot{x}_1 = x_2 - 1$$
$$\dot{x}_2 = -s_1 - 2\pi s_1(1 - s_1^2) - x_1 - 0.3(x_2 - 1) \tag{2-26}$$

where $s_1 = \text{sgn}(x_2)$. In terms of the quantities (2-16), we have $G(s_1) = 2\pi s_1$ and $\gamma(s_1) = (1 - s^2)$. In the linear sliding model, we ignore the term $1 - s^2$ and thus we consider $f_\Sigma \in [-1, +1]$ on $x_2 = 0$. By using the Definition (2-8), the linear sliding equations read

$$\dot{x}_1 = -x_1$$
$$\dot{x}_2 = 0 \tag{2-27}$$

with the sliding region defined by $-0.7 < x_2 < 1.3$. The time response and phase portrait are shown in Figure **2-4** (a) and Figure **2-4** (c), respectively. By considering the nonlinear sliding model (2-26), we have a larger sliding region defined by $-2.7 < x_2 < 3.3$, as shown in Figure **2-4** (b) and Figure **2-4** (d). Specifically, regarding the regularized system of (2-26) with $z = x_2 \varepsilon^{-1}$ we have

$$\begin{aligned}
\dot{x}_1 &= \varepsilon z - 1 \\
\varepsilon \dot{z} &= -s_1(z) - 2\pi s_1(z)(1 - s_1(z)^2) - x_1 - 0.3(\varepsilon z - 1)
\end{aligned} \tag{2-28}$$

where x_1 and z are the slow and fast variables. The critical manifold $\mathbb{C}_1$ is obtained by setting $\varepsilon = 0$ in this formulation,

$$\mathbb{C}_1 = \{(x, y) \in \mathbb{R} \times \mathbb{R} : -s_1(z) - 2\pi s_1(z)(1 - s_1(z)^2) - x_1 + 0.3 = 0\} \tag{2-29}$$

In Figure (**2-3**) we see that the critical manifold has an attractive branch for $-2.7 < x_2 < 3.3$ (black curve) and thus once a trajectory solution reaches $\mathbb{C}_1$ it evolves there, until it loses hyperbolicity near -2.7. The repelling branches correspond to $-2.7 < x_2 < -1$ and $1 < x_2 < 3.3$.
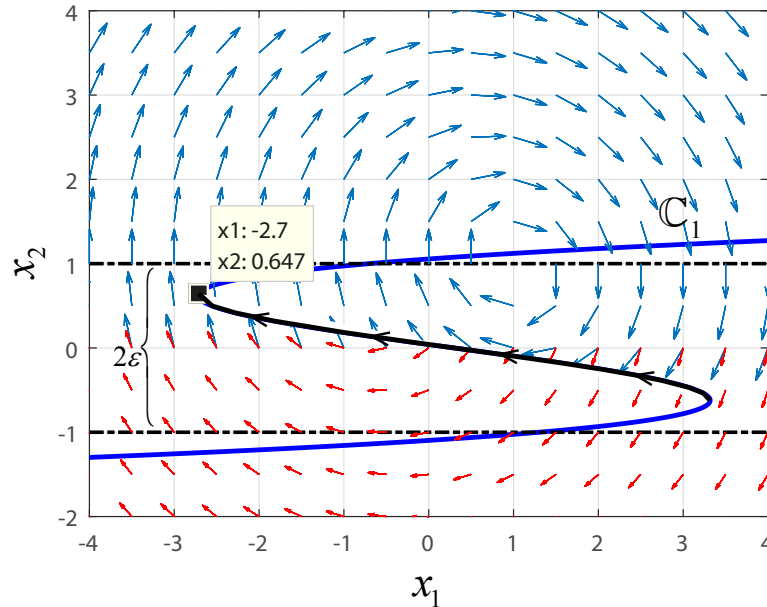
Figure 2-3: Critical manifold $\mathbb{C}_1$ (blue curve) of system (2-28). The slow flow is indicated by the black arrows on $\mathbb{C}_1$ while the arrows outside the critical manifold represent the fast dynamics. The boundary layer $|x_2| < \varepsilon$ is indicated by the dash-line.

Specifically, the sliding region follows from

$$\frac{d}{ds_1}\left[3x_1 - 5s_1 + 10\pi s_1(1 - s_1^2)\right] < 0 \tag{2-30}$$

then,

$$s_1^2 < \frac{1 + 2\pi}{6\pi} \tag{2-31}$$

$$-0.64 < s_1 < 0.64. \tag{2-32}$$

Now, by replacing the value of s_1 in (2-29) we obtain an attracting invariant region between $-2.7 < x_2 < 3.3$. This is confirmed by numerical simulations shown in Figure **2-4**.

(a)

(b)

(c)

(d)
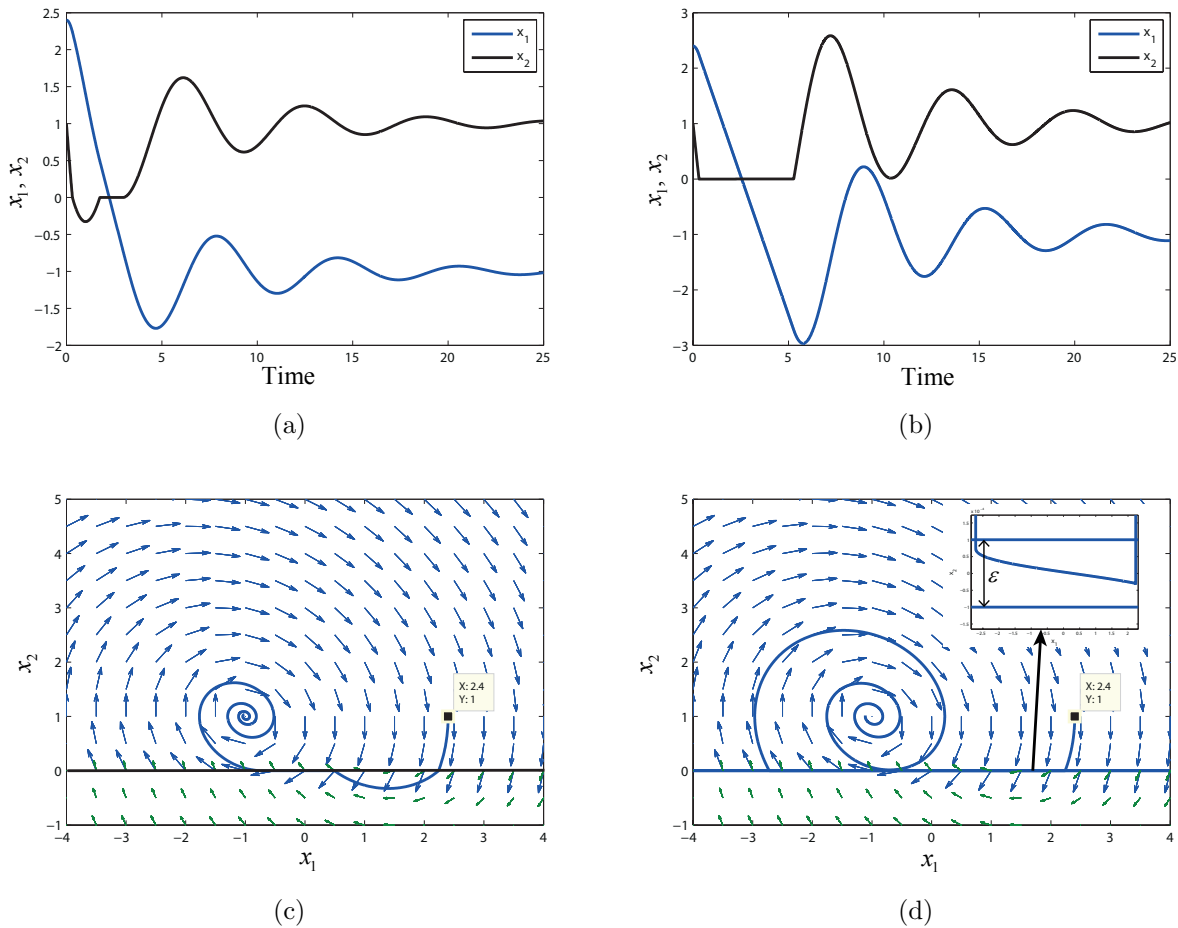
Figure 2-4: Numerical simulations of (2-26) regarding linear sliding modes. By setting $(1 - s_1)^2 = 0$: (a) time evolution and (c) phase portrait. Smoothed nonlinear sliding model panels (b) and (d) corresponding to a boundary layer $|x_2| < 10^{-6}$ show the nonlinear sliding modes. In the panel (d) we zoom the boundary layer, showing a trajectory evolving on the critical manifold. The trajectory solution starts with initial condition $(x_1, x_2) = (1, 2.4)$.

2.3 Tools for studying convergence in discontinuous systems

In this Section we introduce the basic results on contraction analysis for nonlinear systems [66] and a extension of contraction analysis for switching systems [38].

Table 2-1: Standard Matrix measures

Vector Norm, $\lvert \cdot \rvert$	Induce Matrix Norm $\lVert \cdot \rVert$	Matrix Measure $\mu(\,\cdot\,)$
$\lvert x \rvert_1 = \sum_{i=1}^{n} \lvert x_i \rvert$	$\lVert A \rVert_{i1} = \max_{j} \sum_{i=1}^{n} \lvert a_{ij} \rvert$	$\mu_1(A) = \max_{j}\left[a_{jj} + \sum_{i=j} \lvert a_{ij} \rvert\right]$
$\lvert x \rvert_2 = \left(\sum_{i=1}^{n} \lvert x_i \rvert^2\right)^{1/2}$	$\lVert A \rVert_{i2} = \left[\lambda_{\max}(A^T A)\right]^{1/2}$	$\mu_2(A) = \lambda_{\max}\frac{A^T + A}{2}$
$\lvert x \rvert_\infty = \max_{1 < i < n} \lvert x_i \rvert$	$\lVert A \rVert_{i\infty} = \max_{i} \sum_{j=1}^{n} \lvert a_{ij} \rvert$	$\mu_\infty(A) = \max_{i}\left[a_{ii} + \sum_{j=i} \lvert a_{ij} \rvert\right]$

2.3.1 Basic contraction analysis

Contraction analysis is a powerful and systematic tool for proving exponential convergence in dynamical systems. The basic idea can be traced back at least to work of D.C. Lewis see [63, 44]. In control theory, the work of Lohmiller and Slotine [66] has gain much attention, and some developments to study observer problems, nonlinear regulation and synchronization have been reported in the literature, [21, 67, 22].

We consider a generic n-dimensional deterministic dynamical systems of the form

$$\dot{x} = f(t, x), \quad x(t_0) = x_0. \tag{2-33}$$

where the vector field $f : \mathbb{R}^+ \times \mathbb{R}^n \to \mathbb{R}^n$ is assumed to be smooth. We denote $\phi(t - t_0, t_0, x_0)$ the value of the solution x. We say that a set $\mathcal{C} \subset \mathbb{R}$ is a *forward invariant* set for the system (2-33), if for every $t \geq 0$, $x(t_0) = x_0 \in \mathcal{C}$ implies $\phi(t - t_0, t_0) \in \mathcal{C}$ for all $t \geq t_0$.

The idea is to characterize within some metric the distance between any two arbitrary solutions of the system. We refer to this property as *incremental stability*.

Definition 2.3.1. *[57] A scalar continuous function $\alpha(r)$ defined for $r \in [a, 0)$ is said to belong to a class $\mathcal{K}$ if it is strictly increasing and $\alpha(0) = 0$. It is said to belong to class $\mathcal{K}_\infty$ if it is defined for all $r \geq 0$ and*

$$\lim_{r \to \infty} \alpha(r) = \infty$$

Definition 2.3.2. *[3] System (2-33) is said to be Incrementally Asymptotically Stable (δ AS) in a forward invariant set $\mathcal{C} \subset \mathbb{R}^n$ if there exist a class $\mathcal{KL}$ function β_s such that for any $x_0, y_0 \in \mathcal{C}$ and $t_0 \geq 0$ any two trajectories, $x(t)$ and $y(t)$ verify*

$$|x(t) - y(t)| \leq \beta\left(|x_0 - y_0|, t - t_0\right) \tag{2-34}$$

Moreover, if there exist real numbers $c > 0$; $K \geq 1$ such that for all $t \geq 0$

$$|x(t) - y(t)| \leq K |x_0 - y_0| e^{-c(t-t_0)}. \tag{2-35}$$

We say the system (2-33) is Incrementally Exponentially Stable (δES).

Due to the function $f(t, x)$ is continuously differentiable, from the differential analysis we have the exact relation

$$\dot{\delta x} = \frac{\partial f}{\partial x}(x)\delta x. \tag{2-36}$$

where δx is an infinitesimal displacement between two trajectories. Formally, equation (2-36) is known as the variational equation of the system (2-33).

Consider now two trajectories of (2-33) and the displacement δx between them. The distance between these two trajectories can be characterized by any norm given in Table **2-1**. In particular, by choosing the Euclidean distance between these two trajectories i.e., $\delta x^T \delta x$, the rate of change of the squared norm derived from (2-36) is

$$\frac{d}{dt}(\delta x^T \delta x) = 2\delta x^T \dot{\delta x} = 2\delta x^T \frac{\partial f}{\partial x}(t, x)\delta x. \tag{2-37}$$

Denoting $\lambda_{\max}(t, x)$ the largest eigenvalue of the symmetric part of the Jacobian $\frac{\partial f}{\partial x}(t, x)$ we have:

$$\begin{aligned} \frac{d}{dt}(\delta x^T \delta x) = 2\delta x^T \frac{\partial f}{\partial x}\delta x &= 2\delta x^T \left(\frac{\partial f}{\partial x}^T + \frac{\partial f}{\partial x}\right)\delta x \\ &\leq 2\lambda_{\max}(t, x)\delta x^T \delta x \end{aligned} \tag{2-38}$$

and hence,

$$\delta x^T \delta x \leq \delta x_0{}^T \delta x_0 e^{\int_{t_0}^{t} \lambda_{\max}(t, x)d\tau}. \tag{2-39}$$

Now, if we assume that $\lambda_{\max}$ is uniformly negative definite, i.e. $\exists c > 0, \forall x, \forall t \geq 0, \lambda_{\max}(t, x) < -c$, then from (2-39) any infinitesimal length converges exponentially to zero, at a rate c, this in turn implies that any two trajectories of the system (2-33) converge to each other at an exponential rate. Formally, according to the matrix measures given in Table **2-1** we have the following definition [25].

Definition 2.3.3. *System (2-33) is said to be infinitesimally contracting on a set $\mathcal{C} \in \mathbb{R}^n$ if there exits a norm in $\mathcal{C}$, with associated matrix measure $\mu(.)$, such that, for some constant $c > 0$ (termed as contraction rate), it holds that:*

$$\mu\left(\frac{\partial f}{\partial x}(t, x)\right) \leq -c \quad \forall x \in \mathcal{C}. \tag{2-40}$$

2.3.2 Generalized contraction

The definition 2.3.3 provides a sufficient condition to show the contractivity of the system (2-33). A more general result can be obtained by using a general definition of length, in particular by expressing the vector δx in terms of the coordinate transformation

$$\delta z = \Theta(t, x)\delta x \tag{2-41}$$

with $\Theta(t, x)$ being a squared uniformly invertible matrix. Therefore, the variational equation of the system (2-33) in terms of δz-coordinates becomes

$$\dot{\delta z} = \mathbf{F}(t, x)\delta z \tag{2-42}$$

where $\mathbf{F}$ is termed as *generalized Jacobian* and is given by

$$\mathbf{F} = \left(\dot{\Theta} + \Theta\frac{\partial f}{\partial x}\right)\Theta^{-1} \tag{2-43}$$

Again, the distance between trajectories of the (2-48) and the generalized distance δz can also be characterized in terms of the measure matrices. Here, we consider the generalization of the squared length in terms of δz:

$$\delta z^T \delta z = \delta x^T M(t, x)\delta x \tag{2-44}$$

where the matrix $M(t, x) = \Theta^T\Theta$ is continuously differentiable and formally defines a Riemann space [68]. The rate of change of the squared length in terms of the new coordinates can be written as

$$\frac{d}{dt}\left(\delta z^T \delta z\right) = 2\delta z^T \dot{\delta z} = 2\delta z^T\left(\dot{\Theta} + \Theta\frac{\partial f}{\partial x}\right)\Theta^{-1}\delta z \tag{2-45}$$

or equivalently

$$\begin{aligned}
\frac{d}{dt}\left(\delta x^T M\delta x\right) &= \dot{\delta x}^T M\delta x + \delta x^T(\dot{M}\delta x + M\dot{\delta x}) \\
&= \delta x^T\frac{\partial f}{\partial x}^T M\delta x + \delta x^T \dot{M}\delta x + \delta x^T M\frac{\partial f}{\partial x}\delta x) \\
&= \delta x^T\left(\frac{\partial f}{\partial x}^T M + \dot{M} + M\frac{\partial f}{\partial x}\right)\delta x
\end{aligned} \tag{2-46}$$

Therefore, if $\mathbf{F}$ is uniformly negative definite, then $\delta z^T \delta z$ exponentially converges to zero, implying in turn that $\delta x^T \delta x$ exponentially converges to zero. This motivates the following definition.

Definition 2.3.4. *The system $\dot{x} = f(x,t)$, is infinitesimal contractive in a region $\mathcal{C} \in \mathbb{R}^n$, if there exits a norm in $\mathcal{C}$, with associated matrix measured $\mu(.)$, an invertible matrix $\Theta(t,x)$ and strictly positive constant β_M such that*

$$\mu\left(\dot{\Theta}\Theta^{-1} + \Theta\frac{\partial f}{\partial x}(x)\Theta^{-1}\right) \leq -\beta_M, \quad \forall x \in \mathbb{C}. \tag{2-47}$$

In general, the set-valued matrix $\Theta(t,x)$ depends on the system dynamics, and it is still an open problem to find a general methodology to obtain it. A methodology for polynomial nonlinear systems based on *sum-of-squares* optimization and euclidean metrics has been proposed in [6]. In [83], the authors introduced a graphical method for checking or imposing contraction using matrix norms. In this method a constant matrix Θ is constructed by setting some conditions on the elements of the Jacobian matrix $\frac{\partial f}{\partial x}$ that guarantees that the given system is contracting.

2.3.3 Partial contraction

A powerful extension of contraction theory to study synchronization of a network of agents is the concept of *partial* contraction firstly introduced in [97], further references can be found [25, 56]. This is based on the use of some auxiliary system or virtual system whose particular solutions are the solutions of each node in the network. Then if the virtual system is proved to be contracting then all trajectories of the nodes in the network converge exponentially to each other. The basic result of partial contraction can be state as follows (see [56] for the relative proof).

Theorem 2.3.1. *Consider a nonlinear system of the form*

$$\dot{x} = f(x,x,t) \tag{2-48}$$

and assume that the auxiliary system

$$\dot{y} = f(y,x,t) \tag{2-49}$$

is contracting with respect to y. If a particular solution of the auxiliary system (2-49) is a solution of (2-48), then all trajectories of the system (2-48) verify this property exponentially. The original system is said to be partially contracting

2.3.4 Contraction analysis for switching systems

There are a few results on the incremental stability of piecewise smooth systems; notably for piecewise affine (PWA) systems and piecewise smooth continuous (PWSC) systems. In this section, we introduce a contraction analysis of switched systems via regularization, originally proposed in [38]. First of all, we introduce some technical results..

Theorem 2.3.2. *[27] Let $\mathcal{C}$ be a forward invariant set. Consider a piecewise continuous system such that it fulfills conditions for the existence and uniqueness of a Caratéodory solution. If there exist a unique matrix measure such that for some positive constants c_i*

$$\mu\left(\frac{\partial f_i}{\partial x}(x,t)\right) \leq -c_i, \tag{2-50}$$

for all $x \in R_i$, for all $t \geq t_0$ and for all i, then the system is incremental exponentially stable in $\mathcal{C}$ with convergence rate $\min_i c_i$.

Definition 2.3.5. *The Φ-regularization of a bimodal piecewise smooth system (2-8) is the one parameter family, of PWSC functions $f_\varepsilon : U \to \mathbb{R}^n$ given, for $\varepsilon > 0$ by*

$$f_\varepsilon(x) = \frac{1}{2}\left[1 + \Phi\left(\frac{H(x)}{\varepsilon}\right)\right]f_1(x) + \frac{1}{2}\left[1 + \Phi\left(\frac{H(x)}{\varepsilon}\right)\right]f_2(x). \tag{2-51}$$

The key idea in [38] is to prove exponentially incremental stability of the regularized vector field (2-51), which in turn implies exponentially incrementally stability of the bimodal piecewise system (2-8). The main result of the paper is state as follows.

Theorem 2.3.3. *Let $\mathcal{C}$ be a forward invariant set. The piecewise bimodal system (2-8) is incremental exponentially stable in $\mathcal{C}$, with convergence rate $c := \min\{c_1, c_2\}$, if there exist some norm in $\mathcal{C}$ with associated matrix measure $\mu(\cdot)$, such that for some positive constants c_1 and c_2*

$$\mu\left(\frac{\partial f_1}{\partial x}(x)\right) \leq -c_1, \quad \forall x \in \bar{R}_1 \tag{2-52}$$

$$\mu\left(\frac{\partial f_2}{\partial x}(x)\right) \leq -c_2, \quad \forall x \in \bar{R}_2 \tag{2-53}$$

$$\mu\left([f_1(x) - f_2(x)] \cdot \nabla h(x)\right) = 0, \quad \forall x \in \Sigma. \tag{2-54}$$

Proof: The regularized vector field (2-51) can be written as

$$f_\varepsilon(x) = \alpha(x)f_1(x) + \beta(x)f_2(x) \tag{2-55}$$

with

$$\alpha(x) := \frac{1}{2}\left[1 + \Phi\left(\frac{h(x)}{\varepsilon}\right)\right], \quad \beta(x) := \frac{1}{2}\left[1 - \Phi\left(\frac{h(x)}{\varepsilon}\right)\right]$$

Now, taking the time derivative with respect to x, we obtain

$$\frac{\partial f_\varepsilon}{\partial x}(x) = f_1(x)\frac{\partial \alpha}{\partial x}(x) + \alpha(x)\frac{\partial f_1}{\partial x}(x) + f_2(x)\frac{\partial \beta}{\partial x}(x) + \beta(x)\frac{\partial f_2}{\partial x}(x) \tag{2-56}$$

where

$$\frac{\partial \alpha}{\partial x}(x) = \frac{1}{2\varepsilon}\Phi'\left(\frac{h(x)}{\varepsilon}\right)\frac{\partial}{\partial x}\left[\frac{h(x)}{\varepsilon}\right] \tag{2-57}$$

$$\frac{\partial \beta}{\partial x}(x) = -\frac{1}{2\varepsilon}\Phi'\left(\frac{h(x)}{\varepsilon}\right)\frac{\partial}{\partial x}\left[\frac{h(x)}{\varepsilon}\right] \tag{2-58}$$

Now collecting all the terms into a unique expression and setting

$$\gamma(x) = \frac{1}{2\varepsilon}\Phi'\left(\frac{h(x)}{\varepsilon}\right), \tag{2-59}$$

the Jacobian $\frac{\partial f_\varepsilon}{\partial x}(x)$ is

$$\frac{\partial f_\varepsilon}{\partial x}(x) = \alpha(x)\left(\frac{\partial f_1}{\partial x}(x)\right) + \beta(x)\left(\frac{\partial f_2}{\partial x}(x)\right) + \gamma(x)\left[f_1(x) - f_2(x)\right]\nabla h(x) \tag{2-60}$$

Now, regarding the resulting regularized vector field f_ε is continuous, Theorem 2.3.2 can be applied directly. Therefore, we have that f_ε is contracting in $\mathcal{C}$ if there exist positive constants c_1, c_2 and c_3, such that,

$$\mu\left(\frac{\partial f_1}{\partial x}(x)\right) \leq -c_1 \quad \forall x \in R_1 \tag{2-61}$$

$$\mu\left(\frac{\partial f_2}{\partial x}(x)\right) \leq -c_2 \quad \forall x \in R_2 \tag{2-62}$$

$$\mu\left([f_1(x) - f_2(x)] \cdot \nabla h(x)\right) = 0, \quad \forall x \in \Sigma. \tag{2-63}$$

2.3.4.1 Example

Consider the bimodal PWS system (2-2) with

$$f_1(x) = \begin{bmatrix} -14x_1 + 2 \\ -9x_1 - 7x_2 - x_2^4 + 4 \end{bmatrix}, \quad f_2(x) = \begin{bmatrix} -14x_1 + 2 \\ -9x_1 - 7x_2 + x_2^4 + 7 \end{bmatrix} \tag{2-64}$$

and $h(x) = x_2$. For the first condition of the Theorem (2.3.3) we have

$$\mu_1\left(\frac{\partial f_1}{\partial x}(x)\right) = \max\left\{-5, -7 - 4x_2^3\right\} = -5 \tag{2-65}$$

because $-7 - 4x_2^3 < -7, \forall x \in R_1$. Similarity for the second equation we have

$$\mu_1\left(\frac{\partial f_2}{\partial x}(x)\right) = \max\left\{-5, -7 + 4x_2^3\right\} = -5 \tag{2-66}$$

Finally for the last condition we have

$$\mu_1\left([f_1 - f_2] \cdot \nabla h(x)\right) = \mu_1\left(\begin{bmatrix} 0 & 0 \\ 0 & -2x_2^4 - 3 \end{bmatrix}\right) \max\left\{0, -2x_2^4 - 3\right\} = 0 \qquad (2\text{-}67)$$

Therefore the considered PWS system is incrementally exponentially stable with rate convergence $c = 5$. In Figure **2-5** is shown the analytical estimation of the convergence rate against the numerical results.
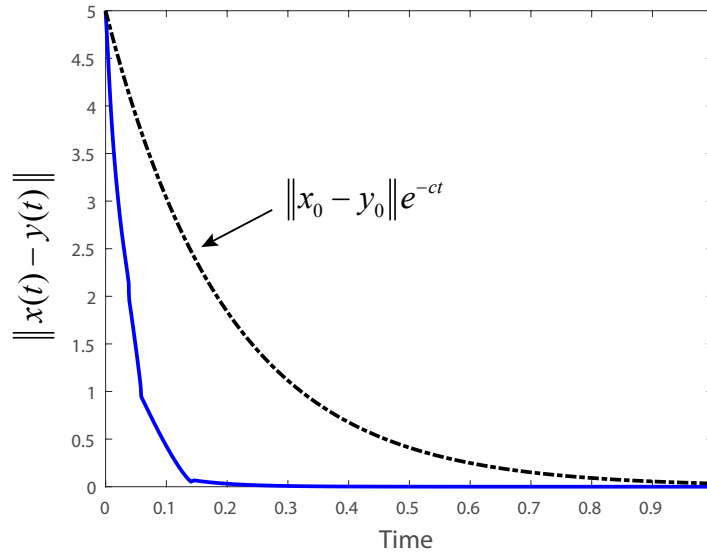
Figure 2-5: Norm of the error between two trajectories $x(t)$ and $y(t)$ in the Example (2.3.4.1) with initial conditions $x_0 = [2\ 2]$ and $y_0 = [3 - 2]$

2.4 Synchronization in complex networks

A complex network consists of a set of dynamical systems interconnected between each other through a communication protocol. In graph theory, each dynamic system corresponds to a node and the communication protocol consist of a set of links between the nodes following some rule. A mathematical description of a complex network of N nodes under diffusive protocol [22] is given by

$$\dot{x}(t) = f(x_i) - \sigma \sum_{j=1}^{N} (x_i(t) - x_j(t)), \quad \forall i \in [1, N] \qquad (2\text{-}68)$$

where $x_i \in \mathbb{R}^n$ represents the state of the i-th node with $f(t, x) : \mathbb{R}^n \mapsto \mathbb{R}^n$ modeling the dynamics of each node in the network. The parameter σ is the coupling gain which determines the strength of interaction between the nodes.

Definition 2.4.1. *Let* $\mathfrak{S}$ *be the* synchronization manifold

$$\mathfrak{S} := \left\{ x \in \mathbb{R}^{nN} \; : \; \|x_j(t) - x_i(t)\| = 0, \; \forall i, j \in [1, N] \right\}$$

then, network (2-68) *is said to reach synchronization if, for any initial conditions* $x_i(0) = x_{i0}$,

$$\lim_{t \to \infty} x(t) \in \mathfrak{S}, \quad \forall t \geq 0, \; i \in [1, N]. \tag{2-69}$$

2.4.1 Example

Chaos synchronization provides potential applications to communications and signal processing [99, 36]. Here, we illustrate the synchronization of a network of five Chua's circuits coupled diffusively via numerical simulations. We consider the network (2-68), where the nonlinear vector field modeling the dynamics of each node is described by

$$f(x) = \begin{pmatrix} -\frac{7}{4}(x_2 - q(x_1)) \\ x_1 - x_2 + x_3 \\ -18x_1 \end{pmatrix}, \quad q(x_1) = (|x_1 - 1| - |x_1 + 1|) \tag{2-70}$$

The system parameters were selected such that single system exhibits chaos as shown in Figure 2-6.

(a)   (b)
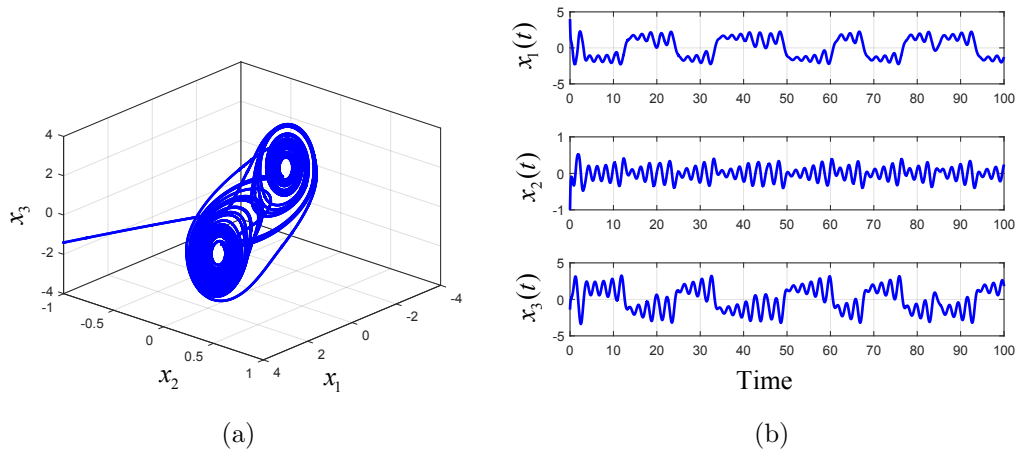
Figure 2-6: Numerical simulations of the single system (2-70) : (a) Chaotic attractor and (b) Time response.

We assume that the network is full coupled, i.e. all the state components are connected between each other. In this example we consider two network topologies, an all-to-all configuration in which, each agent in the network is connected with all agents in the network

and a path-graph topology. Figure **2-7** (b) shows the time evolution for each component of the Chua's oscillators x_{i1}, x_{i2} and x_{i3}. It is possible to observe that after a transient the network synchronize to a particular solution of the single system.

(a)   (b)
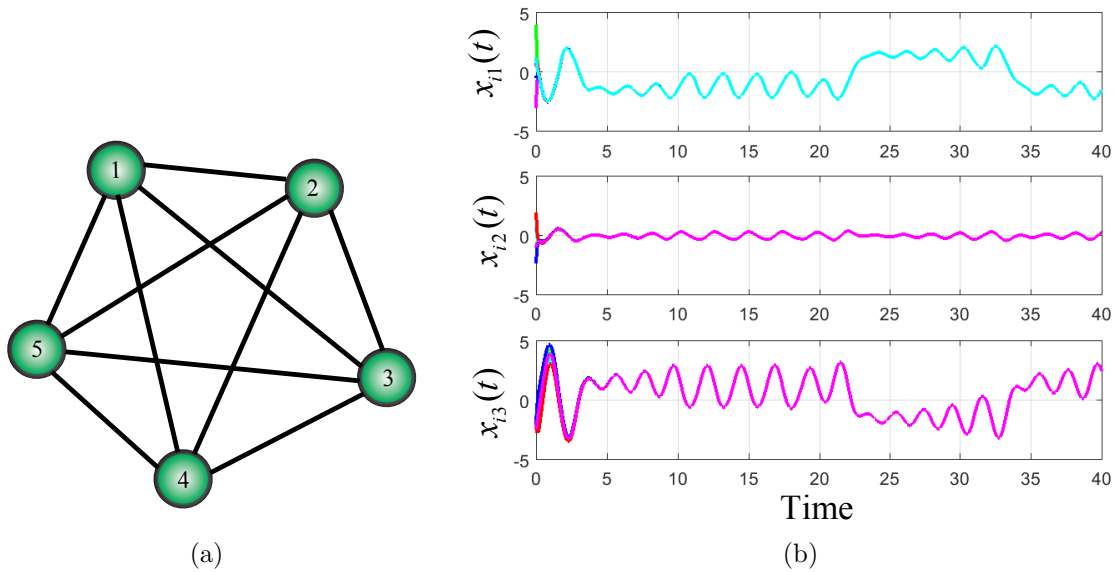
Figure 2-7: Numerical simulation of a network of five Chua's circuits for a coupling parameter $\sigma = 2$, with random initial conditions. (a) all-to-all topology, (b) time evolution of each component $x_i(t)$

In Figure **2-8** (b) it is displayed the time evolution of all state components regarding a path-graph topology. The simulations indicate that the network reaches synchronization regardless of the network topology, however in the path graph network has a larger transient than the all-to-all network.

(a)   (b)
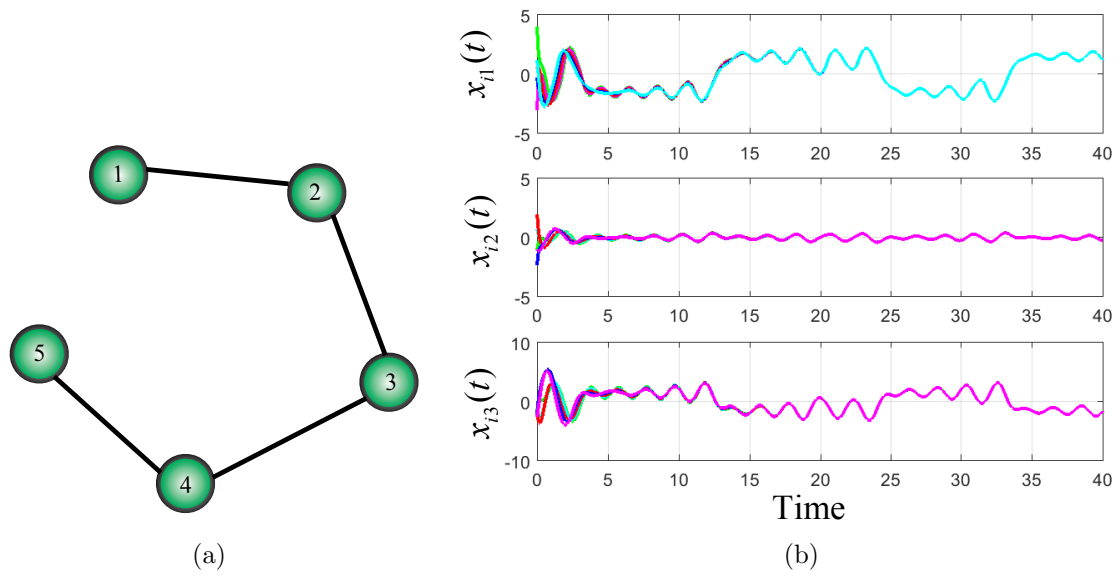
Figure 2-8: (a) Path-graph topology, (b) time evolution of each component $x_i(t)$

Computation of basins of attraction in discontinuous switching systems

In this Chapter we present a numerical routine for computing basins of attraction (BA) in bimodal Filippov systems. In particular we extend the Simple Cell Mapping (SCM) method to cope with the presence of sliding solutions by exploiting an event-driven numerical integration routine specifically written for Filippov switched systems. Our algorithm encompasses a dynamic construction of the *cell-state-space* so that, a lower number of integration steps are required. Moreover, we incorporate an adaptive strategy of the simulation time to render more efficient the computation of basins of attraction of such systems. Throughout this Chapter, the algorithm is illustrated via a set of representative examples including sliding control systems and periodically forced Filippov systems.

The outline of this Chapter is as follows. In Section 3.2 we introduce the concept of the simple cell mapping method. In Section 3.3, an extension of the simple cell mapping algorithm for planar Filippov systems is presented, detailing how the grid is selected and describing the numerical integration method used for dealing with sliding motions. In Section 3.4, the effectiveness of the algorithm is shown by computing the basins of attraction of a sliding control problem and a mechanical system subject to friction. Finally, advantages and disadvantages of the algorithm and possible future extensions for its improvement are discussed.

3.1 Problem formulation

As we pointed out in the last Chapter, the problem of computing basins of attractions in switching systems is mostly addressed by Lyapunov methods in the context of control

theory, where regions of attraction are estimated as sub-level sets of a given Lyapunov function. However, this method provides conservative results meaning that the estimated region is smaller than the exact basin of attraction. A methodology based on Lyapunov methods [69], aimed at estimating regions of attraction in a class of nonlinear piecewise smooth systems is briefly introduced in order to compare with the cell mapping method.

Definition 3.1.1. *Let us consider a positive definite function $v(x) : \mathbb{R}^n \to \mathbb{R}$ for the system $\dot{x} = f(x)$ such that $\exists \gamma > 0 : \dot{v}(x) < 0 : 0 < \|x\| < \gamma$ and assume the origin is an equilibrium point of interest. An estimation of the region of attraction of the origin of such system is given by*

$$\mathcal{P}(\gamma) = \{x \in \mathbb{R}^n : v(x) < \gamma\}. \tag{3-1}$$

Theorem 3.1.1. *Let $v(x) : \mathbb{R}^n \to \mathbb{R}$ be radially unbounded and positive definite function. Let γ be a positive real number, and let i, $1 \le i \le n$, be an integer. If $i \le n - 1$, suppose that there exist polynomial functions $q_i, s_i : \mathbb{R}^n \to \mathbb{R}$ such that*

$$\left.\begin{array}{r} \dot{v}_i(x) + q_i(x)(\gamma - v(x)) + s_i(x)h_i(x) < 0 \\ q_i(x) > 0 \\ s_i(x) \ge 0 \end{array}\right\} \forall x \in \mathbb{R}^n \tag{3-2}$$

while if $i = n$, suppose that there exist functions $q_i, t_i, \ldots, t_{n-1} : \mathbb{R}^n \to \mathbb{R}$ such that

$$\left.\begin{array}{r} \dot{v}_n(x) + q_n(x)(\gamma - v(x)) - \sum_{j=1}^{n-1} t_j(x)h_j(x) < 0 \\ q_i(x) > 0 \\ t_j(x) \ge 0 \end{array}\right\} \begin{array}{c} \forall j = 1, \ldots, n - 1. \\ \forall x \in R^n \end{array} \tag{3-3}$$

Then, $\dot{v}_i(x) < 0 \quad \forall x \in \mathcal{P}_i(\gamma)$ where $\mathcal{P}_i(\gamma) = \mathcal{P}(\gamma) \cap R_i$. Moreover if (3-2) and (3-3) holds, then $v(x)$ is a Lyapunov function for the origin.

Theorem 3.1.1 can be used for computing the largest level set of $v(x)$ such that the negativity of its time-derivative with respect to each subsystem $f_i(x)$ is verified only when such dynamics are active.

Note that $v(x) = x_1^2 + x_2^2$ is not a common Lyapunov function for both subsystems in (3-4), but there exist some regions of the state space in which the negativity of the time derivative of v is verified for each subsystem.

Example: Let us consider a switching system of the form (2-1) with the vector fields given by

$$f_1(x) = \begin{pmatrix} -x_1 + 2x_1^3 x_2 \\ -x_2 - x_1 x_2^2 \end{pmatrix}, \qquad f_2(x) = \begin{pmatrix} -x_1 + x_1 x_2^2 \\ -x_2 + x_1 x_2 + x_1^3 \end{pmatrix} \tag{3-4}$$

and with $\Sigma_1 = \{x \in \mathbb{R}^2 : x_1 = 0\}$. The state space is partitioned in two regions described by

$$R_1 = \{x \in \mathbb{R}^2 : x_1 \geq 0\} \qquad R_2 = \{x \in \mathbb{R}^2 : x_1 < 0\}. \qquad (3\text{-}5)$$

Here, the goal is to estimate the basin of attraction of the origin by computing a level set of a quadratic Lyapunov $v(x) = x_1^2 + x_2^2$.

The conditions of Theorem 3.1.1 can be easily checked by making use of the Matlab toolbox SeDuMi [86]. We computed the level sets obtaining $\gamma_1 = 1.55$ and $\gamma_2 = 2.64$. In Figure **3-1** are shown the corresponding level sets.

(a)   (b)
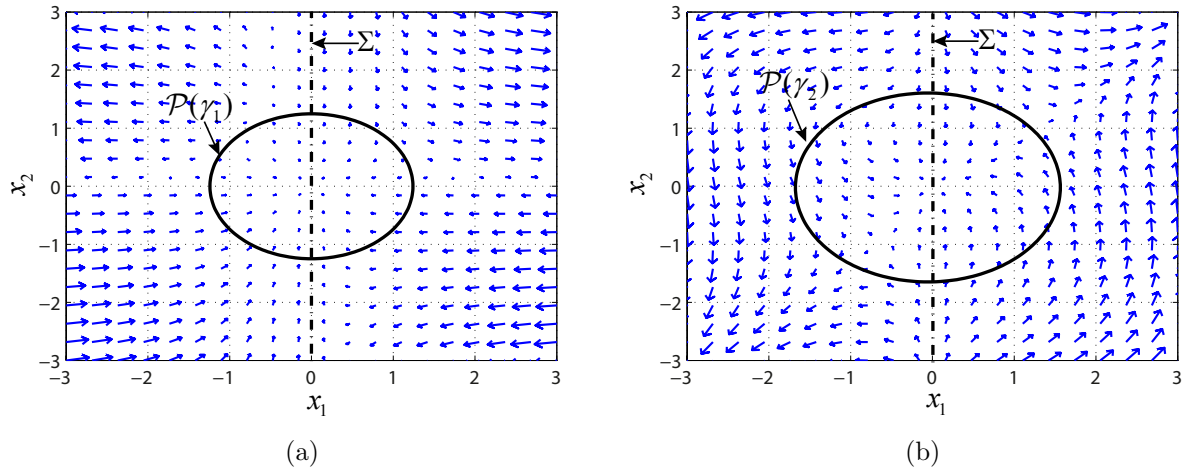
Figure 3-1: Estimation of largest level sets of $v(x) = x_1^2 + x_2^2$ for each subregion of the state space. The blue arrows indicate the direction of vector field f_1 in (a) and f_2 in (b).

In Figure **3-1** (a) is shown how the level set $\mathcal{P}(\gamma_\infty)$ reaches the boundary of the basin of attraction for $x_1 > 0$ where the vector field f_1 is active, the counterpart is shown in Figure **3-1** (b) for $x_1 < 0$. Note that the minimum γ_i, $i = 1, 2$ that satisfies $\dot{v}_i(x) < 0 \quad \forall x \in \mathcal{P}_i(\gamma)$ is $\mathcal{P}(\gamma_1)$, and therefore an estimation of the basin of attraction of the origin for the system (3-4) is given by $\mathcal{P}(\gamma_1) = \{x \in \mathbb{R}^2 : x_1^2 + x_2^2 \leq 1.55\}$.

The basin of attraction of the system (3-4) computed via the cell mapping method is shown in Figure **3-2**. We can observe that the estimation obtained by $\mathcal{P}(\gamma_1)$ represents only a small portion of the basin of attraction.
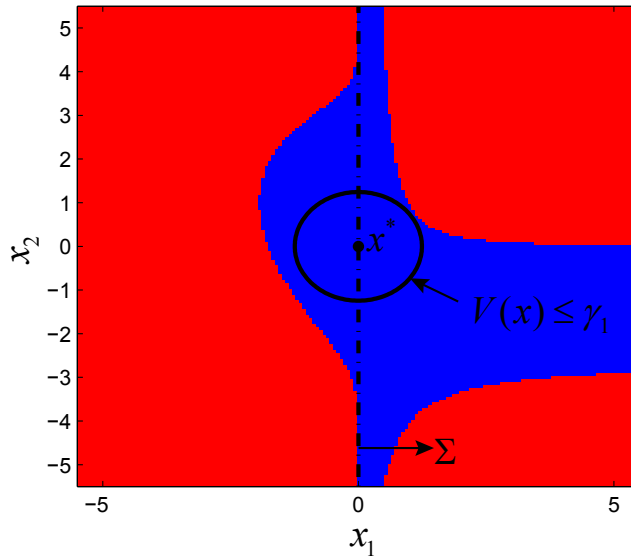
Figure 3-2: Comparison of the numerical techniques used for computing basin of attraction of the system (3-4). The blue region corresponds basin of attraction of the origin using cell mapping method while the region inside the black circle corresponds the estimation provided by the Lyapunov method.

As we saw in the above example, the cell mapping method is an efficient technique for computing basins of attraction in continuous systems. However, fewer results using cell mapping methods have been reported in discontinuous systems with sliding solutions, mainly due to the fact that standard integration routines are inaccurate or inefficient, or both, in the region where discontinuities in the derivatives occur. For example, a possible source of numerical problems is the presence of small oscillations around the discontinuity boundary (numerical chattering behavior) that may arise during sliding mode. Another limitation of existing algorithms based on cell-to-cell mapping is the fact that the region of interest is pre-defined by the user which implies that extra computations are required if it is desired to explore a different region of state space. In this case an adaptive extension of the state space will be more suitable to reduce the computational cost due to the extra CM applications.

In order to overcome these difficulties, we introduce an algorithm based on the simple cell mapping method which exploits the event-driven integration routine proposed in [79], that can automatically cope with the presence of sliding solutions and correct for possible numerical drifts, due to the high frequency switching nature of the discretization of these solutions. Moreover, our algorithm encompasses a dynamic selection of the region to be investigated,

such that a lower number of integration steps are needed in contrast to the case where the region is fixed and preselected by the user. Specifically, after an initial application of SCM in a relatively small number of cells around the equilibrium, or periodic solution of interest, extra layers of cells are added and examined iteratively. The mapping information is stored and used at each iteration, such that numerical integration is required starting just from the extra set of cells that were added. At the end of the process a refinement stage is performed over the basin boundary in order to better identify its limiting region and reduce the error due to the discretization of the state space.

3.2 Simple Cell Mapping

In cell mapping methods the state space of a dynamical system is restricted to a bounded region $\Omega \subset \mathbb{R}^N$ partitioned into regular cells, called *cell state space*. Specifically such space is given by

$$\Omega = \left\{ x \in \mathbb{R}^N : x_i^{(\mathrm{l})} \leq x_i \leq x_i^{(\mathrm{u})}, \ i = 1, \dots, N \right\}, \tag{3-6}$$

where $x_i^{(\mathrm{l})}$ and $x_i^{(\mathrm{u})}$ indicate the lower and upper limit of each of the N state variables of the system. The partition of Ω into rectangular cells is performed by dividing each interval $[x_i^{(\mathrm{l})}, x_i^{(\mathrm{u})}]$ into M_i intervals of equal length δ_i, that is

$$\delta_i = \frac{x_i^{(\mathrm{u})} - x_i^{(\mathrm{l})}}{M_i}, \quad i = 1, \dots, N.$$

In this way, Ω is divided into M rectangular cells, with

$$M = \prod_{i=1}^{N} M_i.$$

Each cell is denoted by an index $j \in 1, \dots, M$. We describe some properties and definitions related to the Simple Cell Mapping which are used throughout the paper.

- *Cell*: An element of the cell state space represented by a center point and lengths along each dimension.

- *Cell index* (*index*, for short): A unique identifier for each cell.

- *Image*: A mapping from one cell to another. The mapping is obtained by integrating the system using the center point of the given cell as initial condition, until the trajectory enters into a new cell.

- *Periodic group* (PG): A set of cells that have been already processed, denoted as n-P group, where $n \in \mathbb{Z}^+$ indicates the period to which those set of cells belong. A cell belonging to an n-P group is denoted as an n-P cell.

- *Transient cell*: A cell or a set of cells that after some mapping end up into an n-P cell.

- *Adjoint cells*: Cells that have at least one corner point in common.

- *Group number*: A unique identifier for each periodic group.

- *Sink cell*: A special cell indicating that the trajectory is being mapped outside of the cell state space.

For a system described by a set of ordinary differential equations (ODEs), the mapping procedure starts by integrating the system using the center point of a cell as the initial condition, until the trajectory leaves the cell and enters in a new cell. If the cell in which the trajectory ends has not already been processed, a new trajectory is initiated from the center of the new cell. This sequence is repeated until a trajectory ends within a cell that has already been processed, indicating that an n-P cell has been found which within SCM implies the existence of a system solution. This process is carried out for each regular cell belonging to the cell state space until all cells have been processed, see Figure **3-3** for a graphical interpretation of the mapping process.

3.3 Enhanced SCM for Filippov systems

Due to the fact that existing cell mapping methods are not able to address the presence of discontinuities in Filippov systems and particularly the occurrence of sliding mode solutions, here we extend the simple cell mapping method by embedding the numerical routine to integrate bimodal Filippov systems described in [79]. In addition, we consider the dynamic evolution of the cell state space with a refinement stage over the basin boundary cells in order to cover the basin of the region under investigation and to reduce the discretization error. Two stop integration criteria are incorporated so that, during the first stage of the algorithm, the integration is terminated as the trajectory leaves the initial cell, as shown in Figure **??** (a). While in the refinement stage, the numerical integration carried out over the cells lying on the boundary of the basins of attraction, is allowed until the trajectory reaches some cell that is not part of the basin boundary cells as shown in Figure **??** (b). This modification, along with the dynamic construction of the state space allow us to drastically
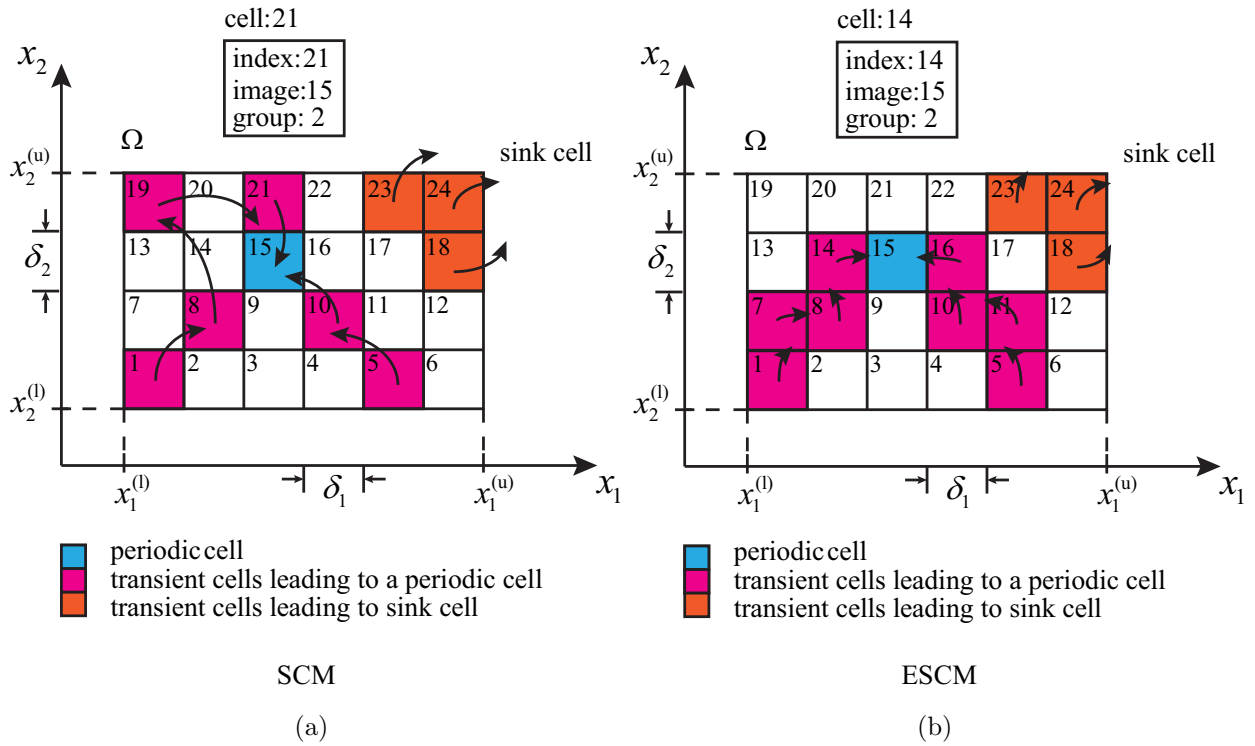
Figure 3-3: Example illustrating the mapping process and some cell's properties (cell:21, cell:14) within SCM and ESCM. Two mapping processes are initialized in cells labeled with indexes 1 and 5, in both methods. Some mapping steps indicate the presence of a stable fixed point inside of the 2-P cell with index 15. Unlike the SCM (a), an adaptive strategy for the simulation time is incorporated in ESCM (b) making the integration time as lows as possible.

reduce the computational cost. Next, we describe in greater detail each of the two proposed innovations leading to an enhanced SCM for Filippov systems.

3.3.1 Integration method

Standard numerical methods for solving ODEs are based on truncation error schemes, however these methods may become inaccurate or inefficient when discontinuities occur [31]. For example, undesired behaviors such as small oscillations around Σ (numerical chattering behavior) must be properly taken into account. One strategy to solve this problem is to use event-detection routines, in which the discontinuity is considered as an event function such that when a numerical solution reaches the discontinuity surface Σ, a new vector field (the so-called sliding or Filippov vector field (2-7)) is constrained to evolve over Σ until certain conditions are satisfied. This event-driven scheme was successfully implemented for simulating Filippov systems for a single discontinuity surface in [79], resulting in an automatic and robust algorithm for studying a wide variety of problems, [31, 62, 13]. The event functions considered in [79] are

$$e_1(t,x) := h(x), \quad e_2(t,x) := \mathcal{L}_{f_1}h(x), \quad e_3(t,x) := \mathcal{L}_{f_2}h(x)$$

where $e_1(t,x)$ locates intersection points between the flow and the discontinuity boundary Σ, checking the possible existence of sliding dynamics, while $e_2(t,x)$ and $e_3(t,x)$ allow to keep track the sliding flow when it enters into R_1 or R_2, respectively. A description of the tasks accomplished by the numerical routine is given below:

- Smooth vector fields outside of Σ, R_1 or R_2 are integrated in time by standard numerical integration routines.

- Their intersection points with the discontinuity boundary are precisely located as trajectories reach Σ.

- The vector field on $\widehat{\Sigma}$ is used to integrate sliding mode solutions (2-8) in time.

- Possible numerical drifts while evolving in $\widehat{\Sigma}$ are carefully avoided by monitoring transversality conditions and by means of an appropriate numerical extension of the Filippov vector field (see [79] for further details).

- While in Σ conditions are constantly monitored to decide whether to remain on the switching boundary or to leave it.

The numerical routine proposed in [79] is mostly used for Filippov systems with a single discontinuity surface, limiting the computation of the basins of attraction for such kind of systems. Nevertheless, it is straightforward to extend the integration routine for an arbitrary number of discontinuity surfaces as discussed in [79]. For example, in the case of biological and mechanical systems with two discontinuity surfaces where the sliding vector field at the intersection between surfaces is well-defined, the equivalent control method [90] and the analytical results of the entry and exit points of co-dimension 2 sliding vector fields reported in [28] can be straightforwardly implemented for simulating accurately such systems. The main disadvantage with this approach is that the number of surfaces and event locations grow quickly with the number of discontinuity surfaces which naturally increases the simulation time.

3.3.1.1 Integration stopping criterion

One limitation of the SCM is that the integration time is global, and selected arbitrarily beforehand. This may introduces spurious mapping results when the integration time is relatively short, since the trajectory may remain within the same cell from where the simulation started instead of reaching the image cell, which under SCM will indicate erroneously the presence of a new attractor. On the other hand, if the integration time is relatively large, then the computational cost of the algorithm might become unnecessarily large.

Therefore, to avoid these limitations, we introduce two integration stop criteria to render the selection of the simulation time adaptive. Before the refinement stage, the numerical integration is terminated only once the trajectory reaches the image cell. In particular, we introduce an extra event function in the numerical integration routine defined as

$$e_4(t, x) = \|x(t_n) - x(t_0)\|_\infty - \frac{\delta_i}{2} + \varepsilon, \tag{3-7}$$

where $x(t_0)$ and $x(t_n)$ denote the current initial point and the current end point of the trajectory, respectively, ε is a small positive parameter which guarantees that the trajectory has left the initial cell and $\|\cdot\|_\infty$ is the infinity vector norm. The extra event function allows to keep track of the flow so that integration continues until the trajectory reaches a threshold determined by the predefined cell-width δ_i. Instead, during the refinement stage, the integration continues until the flow reaches a cell that has been already tagged in earlier iterations, provided that it is not part of the boundary cells, as shown in Figure 3-6 (b).

In the flow chart in Figure 3-4 we present an overview of the algorithm for simulating

Filippov systems with one discontinuity surface. A description of the tasks accomplished by the numerical integration routine is given below:

Algorithm 1 A description of the numbered boxes in the flow chart in Fig 1 is given here.

1: Initialize the program with the solver properties, vector fields, IC and provide an initial simulation time $Tspan$.
2: Determine the initial state of the system, Σ, R_1 or R_2.
3: Solve the current ODE until an event e_i occurs.
4: Check if time is equal to the final time.
5: Check region of the state space in which the system is, according to the event function e_i.
6: Set the corresponding vector field f_1, f_2 or f_Σ and go to 4.
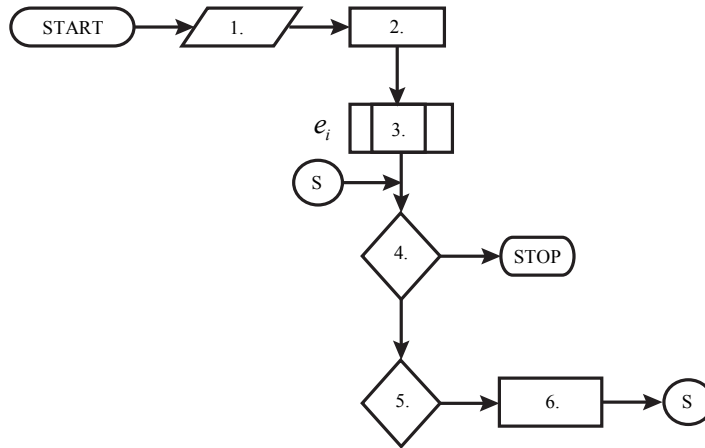
Figure 3-4: A schematic flow chart of the algorithm for simulation of Filippov systems with one discontinuity surface. A description of the numbered boxes is given in Algorithm 1.

In principle, the integration time can be selected considerably big since once the trajectory has reached some cell outside of the boundary region the integration is terminated.

3.3.2 Cell state space construction

When applying the SCM, the discretization of the state space introduces some errors due to a possible inconsistency between the end point of a trajectory segment within a cell and the start of the subsequent trajectory segment. Hsu [47] claims that this problem can be solved by using a more refined grid, but this increases the computational cost of the algorithm. To overcome this problem and render our method more efficient, we propose the use of a

dynamically allocated cell grid, which starting from a small area contained in the basin of attraction of the attractor of interest, is grown so as to map the entire basin of attraction and isolate its boundaries.

Specifically, the algorithm constructs an initial cell state space with the information provided by the user (for example a point in the phase space). Then after a first application of SCM, the algorithm automatically adds and examines layers of cells according to whether or not the cells lie in the basin of attraction. The algorithm uses information about earlier iterations such as group numbers and indexes to determine if the extra set of cells belongs to the basin of attraction. For example, when a trajectory starting in the extra set of cells enters into a cell that has been tagged as part of the basin of attraction, the extra cell is also tagged with the same periodic group and therefore tagged as belonging to the basins of attraction. A graphical representation of the stages of the algorithm is shown in Figure **3-5**.

It is worth nothing that the construction of the cell state space is independent of the location of the discontinuity surface. Therefore, there is no need for a special treatment of those cells that cover the switching manifold.
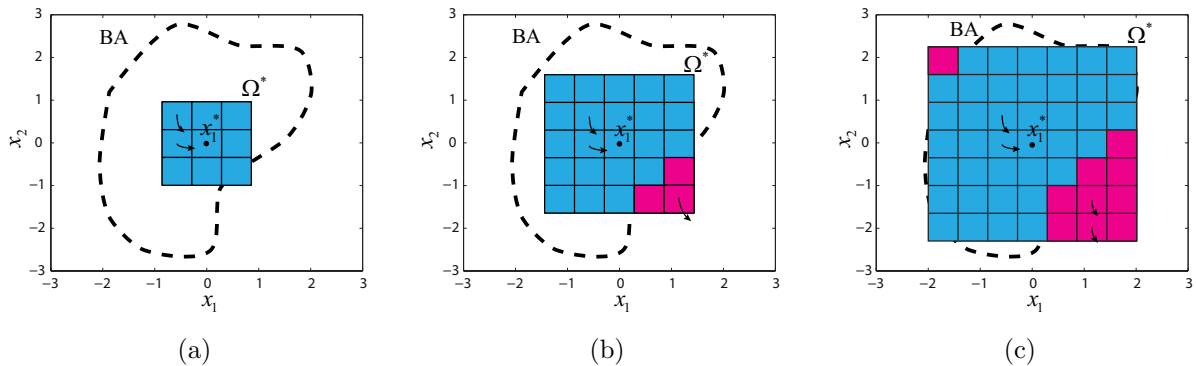
Figure 3-5: Illustration of initial steps of ESCM algorithm before the refinement stage, for a fixed point x_1^*. The boundary of the basin of attraction of x_1^* is represented by the black dash line while arrows stand for trajectories mapping inside and outside of the studied region Ω^*. An initial region covering the attractor is examined by ESCM at the first step graph (a), subsequently in step 2 and 3 layers of cells are added and examined in (b) and (c).

Finally, a routine to isolate and to redefine the cells that lie on the boundary of the basin of attraction is incorporated into the main program. Under the ESCM algorithm described

previously, cells that are located on the boundary of two or more attractors satisfy two properties. The first is that they have different group numbers, and the second is other property is that they are adjoint, i.e., the distance between the center points of the cells is equal to the cell size δ_i. Once the boundary cells have been found, they are subdivided and investigated by applying again our enhanced SCM algorithm as shown in Figure. **3-6**.

(a)   (b)
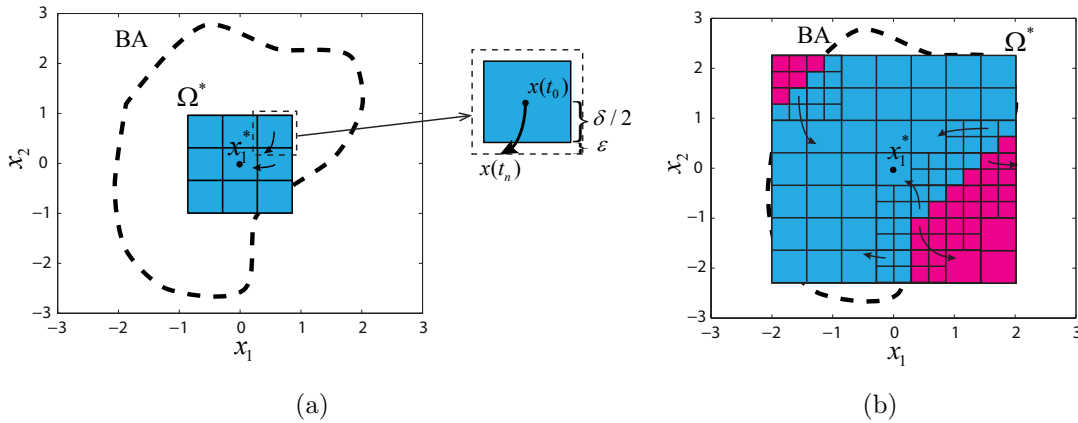
Figure 3-6: Boundary refinement of the previous example. In this illustration, boundary cells are subdivided into a 4×4 grid of cells and each of which is investigated by the ESCM algorithm. Some mapping processes evidence the difference between the stop-integration criterion used in the first applications of the algorithm (a) and the one used in the refinement stage (b). In this example we assume equal partitions of the state space, i.e. $\delta = \delta_1 = \delta_2$.

3.4 Applications

Next, we present two representative examples, to illustrate the effectiveness of our proposed algorithm. The two main stages of our algorithm, that is, the construction of the cell state space and the cell size refinement are validated by computing the domains of attraction of a sliding control problem and a dry friction oscillator. In all examples the ODE-solver `ode45` (4th-order Runge Kutta) has been used with Matlab's routines. The software used in these examples can be downloaded from `https://sites.google.com/site/dibernardogroup/download`.

3.4.1 Sliding control system

Sliding mode control is a well known nonlinear control strategy which is used in a wide range of technical domains, mainly due its simple implementation and remarkable robustness

properties [91, 45]. Here, we consider a second order system with a linear sliding surface. Choosing some representative parameter values, we select the closed loop system

$$\dot{x} = \begin{pmatrix} -1 & 1 \\ 0 & 3 \end{pmatrix} x + \begin{pmatrix} 0 \\ 1 \end{pmatrix} u, \tag{3-8}$$

where the discontinuous control is given by $u = -10\,\mathrm{sgn}(x_1 + x_2)$. The control strategy is designed to steer the system dynamics to the zero equilibrium point, which is lying on the discontinuity manifold and can therefore be classified as a pseudo equilibrium according to [24]. Now, by adopting the formalism of Filippov systems (see Sec. 5.2), the vector fields corresponding to each partition of the state space can be written as

$$f_1(x) = \begin{pmatrix} -x_1 + x_2 \\ 3x_2 - 10 \end{pmatrix}, \quad f_2(x) = \begin{pmatrix} -x_1 + x_2 \\ 3x_2 + 10 \end{pmatrix}, \tag{3-9}$$

with the zero-level set $\Sigma_1 = \{x \in \mathbb{R}^2 : x_1 + x_2 = 0\}$ defined as the switching manifold. Clearly, simple computations show that each of the vector fields f_1 and f_2 has an hyperbolic equilibrium point. Nevertheless, the interaction between each other along Σ_1 gives rise to an invariant set limited by the stable manifolds of the saddle solutions, with the zero equilibrium as a fixed point.

(a)   (b)
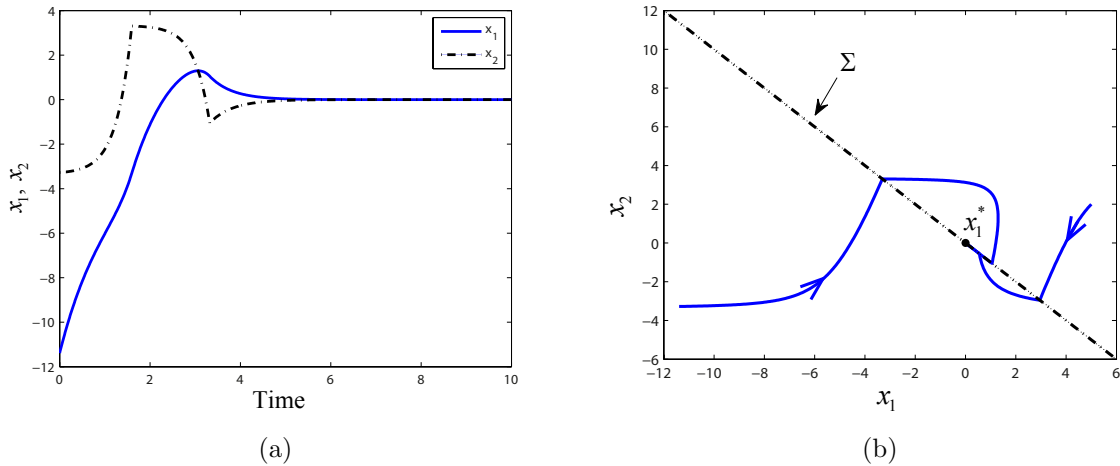
Figure 3-7: Solutions of the sliding control system (3-8). In (a) is shown the time evolution for a random initial condition while in (b) the phase portrait of two trajectories initialized in different regions of the state space.

To analyze the basin of attraction of the control system, we apply the ESCM. Some of the steps of the algorithm used to construct the BA of interest are shown in Figure 3-8, while the final result is depicted in Figure 3-9.
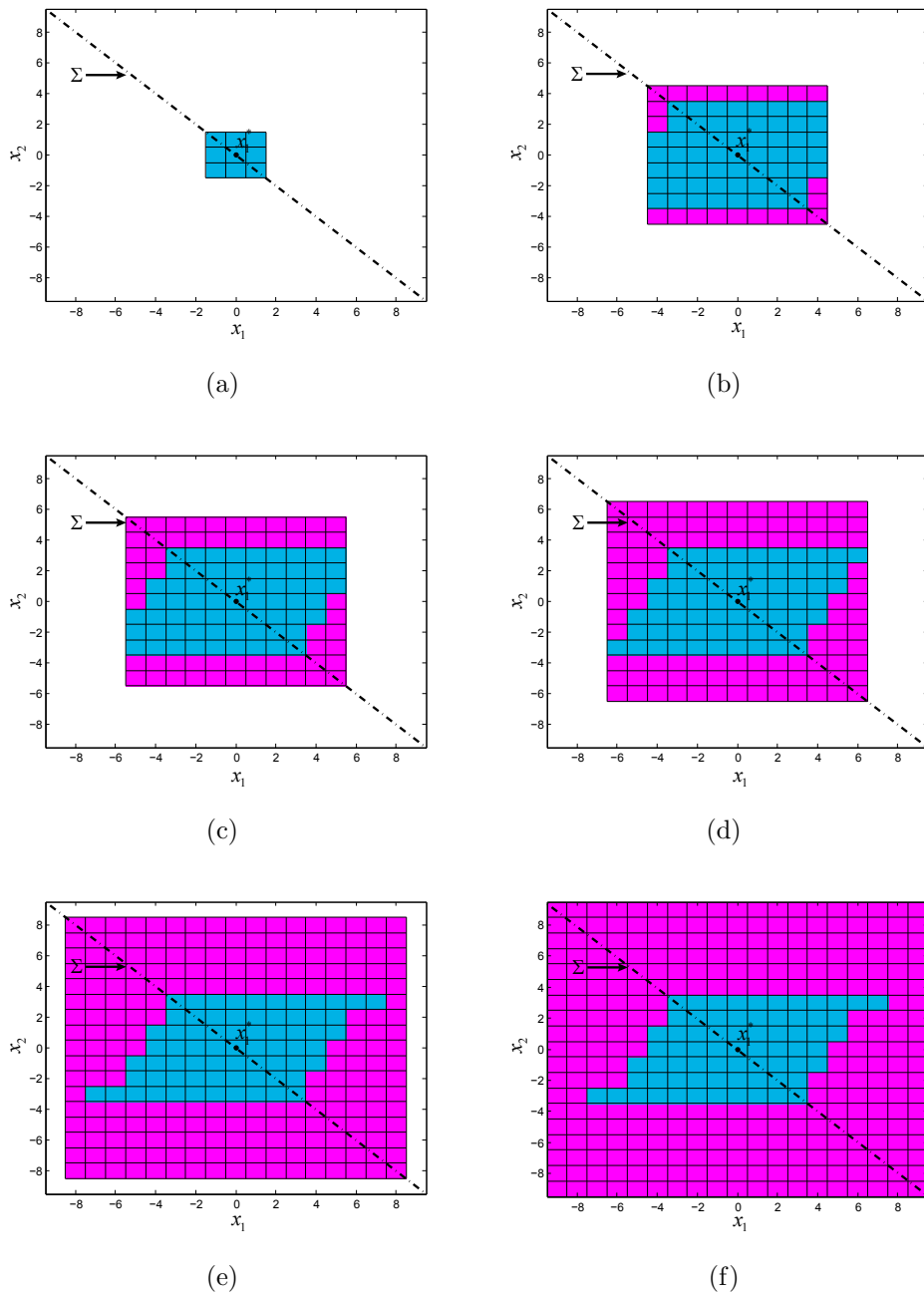
Figure 3-8: Sequence of the dynamic construction of the cell state space, by assuming regular cells, i.e. $\delta = \delta_1 = \delta_2$. The black lines are used to represent the cell state space, so that each square represents a cell. The black dash-line corresponds to Σ. The initial region (blue cells) used in the first iteration is shown in (a). The 3nd, 4th, 5th and 6th iterations of the algorithm are shown in (b)-(e), respectively. A first (coarse) approximation of the basins in the 7th iteration is shown in (f).

Cells colored in blue belong to the basin of attraction of the equilibrium $x_1^* = (0,0)$, while initial conditions in the magenta cells are mapped outside the basin of attraction. The total number of cells investigated by the ESCM at the end of the first stage is 361, as shown in Figure 3-8 (f). Nevertheless, it is worth noting that, at each step of the algorithm just a small group of regular cells is investigated, since starting from a small set of cells around the origin, extra layers of cells are only added and examined iteratively. Once the entire basin has been mapped a refinement stage is performed in order to get more accurate results, in which the boundary the boundary cells are split, and the ESCM is applied again as described above.
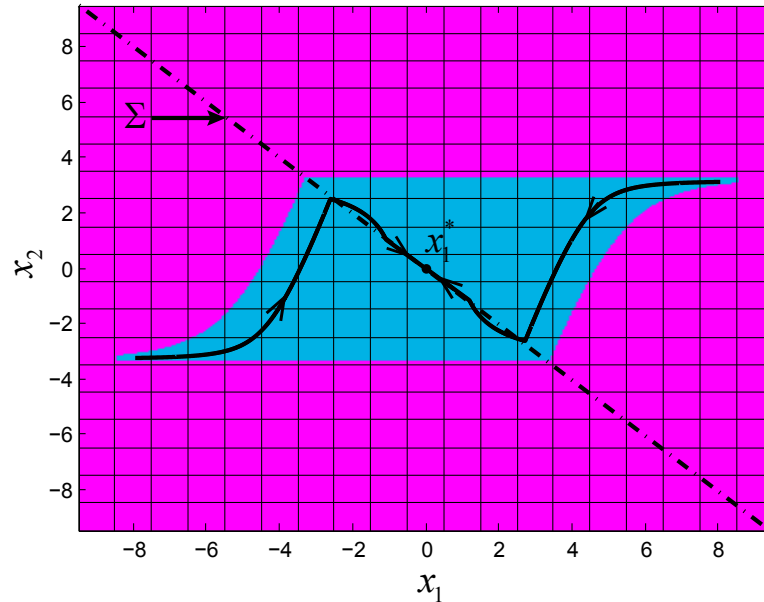
Figure 3-9: Basins of attraction for the sliding control problem (3-8) using ESCM, for an initial resolution of 19×19 grid of cells, initial cell size of $\delta^* = 1$ (initial stages) and $\delta^{**} = 0.083$ for the refinement stage. Black curves stand for trajectories inside of BA of x_1^*, for initial conditions $(x_1, x_2) = (8, 3.3)$ and $(x_1, x_2) = (-8, -3.3)$ while the dash-line indicates the switching manifold.

Another advantage of the refinement is that the initial cell dimensions can be relatively large, so that a bigger region of state space can be explored with a relatively lower number of iterations of the algorithm being required.

To provide a validation of the ESCM performance, in terms of the number of investigated cells and the total CPU time spent in the mapping process, the BA shown in Figure **3-9** was computed using the SCM and the ESCM with fixed integration time (ESCM-Ts). The computation times and the number of investigated cells for the sliding control example (3-8) are shown in Table **3-1**. The results indicate a reduction of at least 50% of the computational cost spent by the classical SCM applications, even using the ESCM with fixed integration-time. These results suggest that the strategy of combining different cell sizes and adaptive schemes of the integration times within cell mapping methods is effective not only for reducing the computational cost, but also for finding new invariant regions in Filippov systems.
It is worth nothing that, in all three cases, we set the algorithm parameters so as to obtain

Table 3-1: Total number of investigated cells within SCM, ESCM-Ts and ESCM. The CPU time used in all three methods is reported below.

Method	Integration time (s)	Number of cells			CPU time (s)
		$\delta^* = 1$	$\delta^{**} = 0.083$	Total	
SCM	4	0	51948	121104	1315
ESCM-Ts	4	361	13536	20713	409
ESCM	adaptive	361	13536	20713	229

the same diagram shown in Figure **3-9**. Thus, in the case of the SCM we set a grid with the same dimension chosen in the final refinement stage of the ESCM. Thus, since we considered a grid of cells of 19×19 in the initial stage of the algorithm (Figure **3-8** (a)-(f)) and a grid of cells of 12×12 in the refinement process 12×12, we set a 228×228 grid of cells in the SCM application.

To further test the efficiency of the ECSM, we computed the same basin of attraction using the ESCM with different fixed integration times. The CPU times for different integration times are listed in Table **5-1**, indicating that even with fixed integration time, the ESCM is superior to the classical cell mapping methods. The lack of available numerical tools for computing basins of attraction in piecewise smooth systems makes it difficult to perform a comparison of our algorithm with respect to other strategies, however it is clear that, a better approximation is achieved in terms of the proportion of the basins found, rather than those achieved by means of other more conservative methods (e.g. Lyapunov based approaches).

Table 3-2: Comparison of the CPU time for different values of the simulation time.

Integration time	CPU time (s)		
	SCM	ESCM-Ts	ESCM
4	1315	409	229
8	2107	633	229
16	3739	1121	229

3.4.2 Dry friction oscillator

Dry friction is a very common phenomenon underlying many physical applications e.g. rigid body impact, pneumatic actuators, brakes and gears, and is therefore extremely relevant in different fields of engineering. Here we consider a single-degree-of-freedom nonsmooth oscillator under external excitation which has been widely studied [24, 58, 51] since it exhibits complex dynamics due to its discontinuous nature. The nonsmooth mechanical system of interest is shown in Figure **3-10**. It is composed by a block of mass m which is supported by a belt moving with constant velocity v. The block is connected to a fixed support by a linear elastic spring of stiffness k and is subject to an external harmonic force of magnitude A and frequency ω.
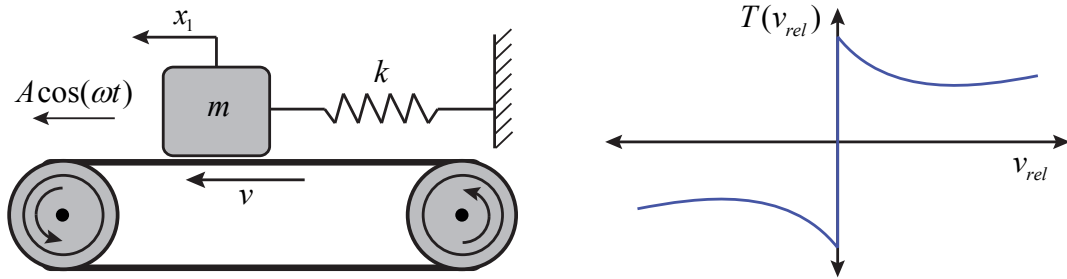
Figure 3-10: The dry friction oscillator along with the adopted nonsmooth friction model, $v_{rel} = x_2 - v$.

If the block is in the stick phase (i.e. the block is moving at the same speed as the belt), the interaction between the spring force, applied harmonic force and friction force cause the block to start slipping (i.e. the block is moving at a different speed relative to the belt) and vice versa. The equations of motion can be expressed as

$$\begin{aligned}
\dot{x}_1 &= x_2 \\
\dot{x}_2 &= -\frac{k}{m}x_1 + \frac{A}{m}\cos(\omega t) + T(x_2 - v),
\end{aligned} \tag{3-10}$$

where x_1 and x_2 represent the position and the velocity of the block. The function $T(x_2 - v)$ describes the friction between the mass and the belt and is formulated as

$$T(x_2 - v) = \begin{cases} -g\left(\frac{\alpha}{1-\gamma(x_2 - v_{dr})} + \beta + \eta(x_2 - v)^2\right) & \text{if} \quad x_2 > v, \\ g\left(\frac{\alpha}{1-\gamma(x_2 - v_{dr})} + \beta + \eta(x_2 - v)^2\right) & \text{if} \quad x_2 < v. \end{cases} \tag{3-11}$$

It is known that for specific values of the excitation frequency ω, two stable periodic orbits and one saddle periodic orbit coexist. These periodic solutions correspond to a fixed points of the stroboscopic Poincaré map associated to the system of interest. For a detailed analysis of this system see [72, 41, 19]. By using the Filippov formalism (2-2), the dynamics in each partition of the state space are modeled by the vector fields

$$f_1(x) = \begin{pmatrix} x_2 \\ \frac{-kx_1 + A\cos(\omega t)}{m} - g\left(\frac{\alpha}{1+\gamma(x_2 - v)} + \beta + \eta(x_2 - v)^2\right) \end{pmatrix} \quad \text{if} \quad x_2 > v,$$

$$\tag{3-12}$$

$$f_2(x) = \begin{pmatrix} x_2 \\ \frac{-kx_1 + A\cos(\omega t)}{m} - g\left(\frac{\alpha}{1-\gamma(x_2 - v)} + \beta + \eta(x_2 - v)^2\right) \end{pmatrix} \quad \text{if} \quad x_2 < v,$$

with the zero-level set $\Sigma_2 = \{x \in \mathbb{R}^2 : x_2 - v = 0\}$ defined as the switching manifold. In this numerical study, we use the parameters $v = 1$, $\alpha = 0.3$, $\gamma = 1.42$, $\beta = 0.1$, $\eta = 0.01$, $A = 3.6$, $K = 1$, $g = 10$ and $\omega = 1.067$. We are interested in computing the BA for the stable periodic solutions $x_1^+ = (x_1, x_2) = (-0.685, 3.01)$ and $x_2^+ = (x_1, x_2) = (-0.295, 0.99))$. In order to use our numerical routine with periodically forced systems, it is necessary to set the integration time equal to the forcing period of the system, that is $T = 2\pi/\omega$ where ω is the excitation frequency. This effectively means that we are integrating the flow to obtain the stroboscopic Poincaré map associated to the system of interest.
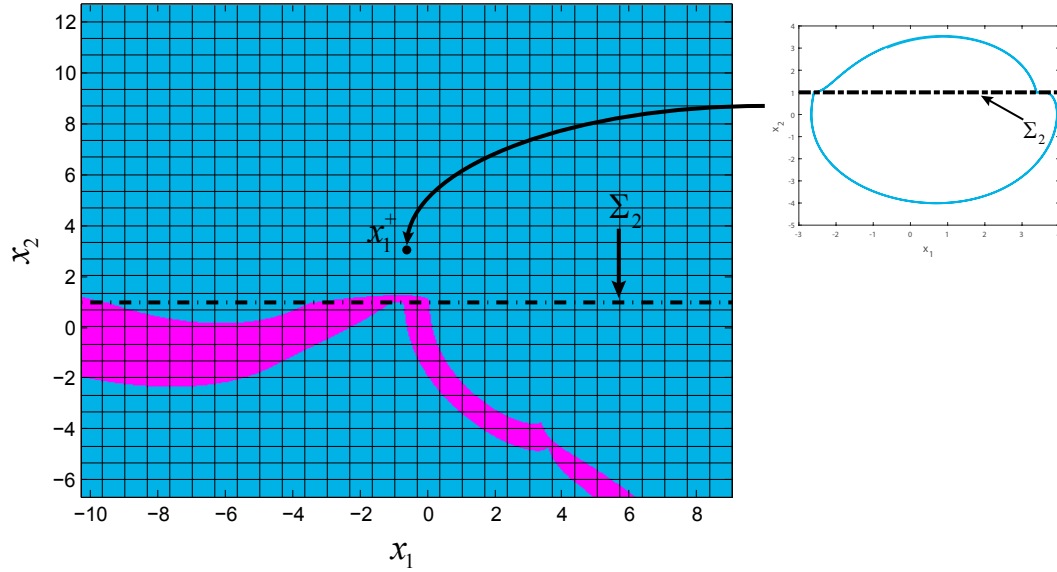
Figure 3-11: Basin of attraction of the periodic solution x_1^+, for an initial resolution of 29×29 grid of cells corresponding to a cell size of $\delta^{***} = 0.66$. The cell sizes of in the refinement stage is set $\delta^{****} = 0.125$. Numerical integrations corresponding to 3 periods were performed. The numerical solution x_1^+ is shown in the right panel.

The domain of attraction diagrams of the stable periodic orbits corresponding to the fixed points x_1^+, x_2^+ and its numerical solutions are displayed in Figures **3-11** and **3-12**. The blue regions represent the set of initial conditions for which the flow converges towards the periodic solutions x_1^+ in Figure **3-11** and x_2^+ in Figure **3-12**, while initial conditions in the magenta region map outside of the investigated periodic solution.
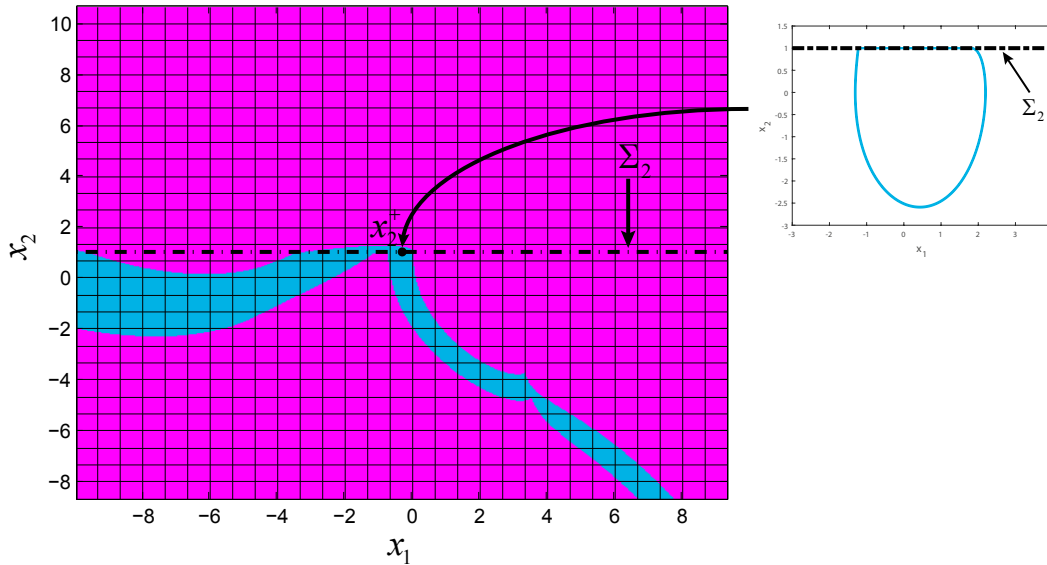
Figure 3-12: Basin of attraction of the periodic solution x_2^+. The ESCM algorithm was initialized selecting a small region 3×3 grid of cells with the equilibrium point as center of the grid. Then 13 layer of cells were added and analyzed at each iteration by ESCM algorithm. In the refinement stage, each cell belonging to the boundary of the BA was divided into a 16×16 grid of cells.

The computation of the BA reported in Figure 3-11 reveals that the invariant manifold that separates the basins of attraction of x_1^+ and x_2^+ is continuous but not differentiable due to the presence of sharp corners, a phenomenon reported in the literature on PWS systems, see e.g. [7].

Note that Figs. 3-11 and 3-12 provide essentially the same information, nevertheless, the ESCM-Ts algorithm was initialized in different regions of the state space in each case. It is worth noting that information regarding the dynamic behavior of the friction oscillator presented in this paper, is not novel; the reader is directed to [72, 41] for more complete details. Rather, it is the manner in which it is computed that is new.

3.5 Discussion

In this Chapter, we have presented a numerical routine for computing basins of attraction in bimodal Filippov systems based on simple cell mapping. We propose a new way to construct the cell state space is proposed in order to reduce the computational cost associated to the number of integrations performed by cell mapping methods. Another advantage is that

accurate basin boundaries can be found due to subdivision of the boundary cells. The ESCM algorithm was used for studying the BAs of a sliding control problem and a dry friction oscillator showing the stages of proposed methodology. We have shown that the computational effort of the ESCM is lower than the classic SCM with event-integration routines even if the ESCM uses fix simulation times. The structure of the algorithm can be easily implemented in a multi-core environment [8], so that not only one refinement stage can performed but also different refinement levels at different processors at the same time can be performed. In the case of high order systems the integration method used for the ESCM combined with the multidimensional cell mapping method (MDCM) [33, 9] can be addressed towards computing basins of attraction of high order Filippov systems. Next, we will perform a piecewise smooth analysis of two coupled mechanical oscillators subjected to friction. This model will be used to characterize the sliding motions along a co-dimension 2 switching surface given by the intersection of two switching surfaces of co-dimension 1. Moreover, nonlinear sliding surfaces will be consider in order to model a stiction friction model.

Piecewise Smooth Analysis of Two Heterogeneous Coupled Friction Oscillators

In Chapter 3 we carried out a numerical study of the stability of Filippov systems with a single switching manifold, through the computation of their basins of attraction. The implementation of the numerical tool for the computing the BA in bimodal Filippov systems was based on the full characterization of the entry and exit points of the sliding flows, existing in the literature of PWS systems [30, 28]. Therefore, understanding the main features underlying the behavior of switching is of great importance for developing tools that allow investigating such class of systems. In this Chapter we investigate the stability of Filippov systems with two switching manifolds, taking as an example two heterogeneous coupled mechanical oscillators subject to friction. In particular, we start analyzing the two coupled oscillators with classical Coulomb's friction force, then we extend the piecewise smooth analysis by making use of Hidden dynamics (Sec 2.2) approach in order to model friction forces with the Stribeck effect.

4.1 Problem statement

Here, we consider multimodal piecewise smooth systems (Sec 2.1.2) with two switching surfaces embedded in the switching terms s_1 and s_2, also known as Filippov systems of co-dimension 2. The state space of the Filippov system of co-dimension 2 is divided into four regions denoted by R_1, R_2, R_3 and R_4 as shown in Figure 4-1. According to the system dynamics, the sliding dynamics may evolve either along a single switching surface $\Sigma_{1,2}^{\pm}$ or

along the intersection of the two switching surfaces $\Sigma = \Sigma_1 \cap \Sigma_2$. In the following, we will refer the later one as sliding of co-dimension 2.
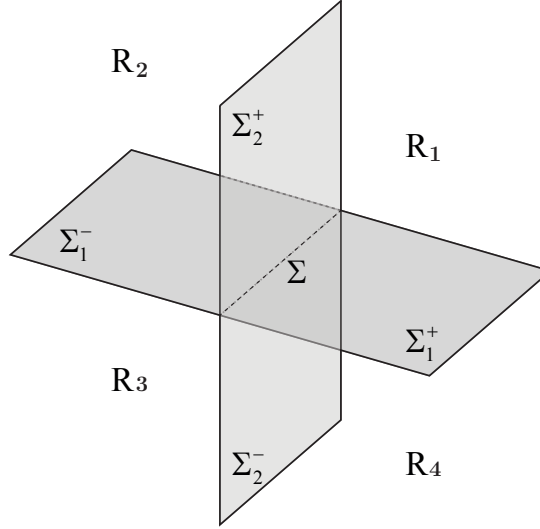
Figure 4-1: The discontinuity surfaces Σ_1 and Σ_2, their intersection Σ and the subsets R_i.

Formally, we define the discontinuity surfaces as

$$\Sigma_1 = \{x \in \mathbb{R}^n : h_1(x) = 0\}, \qquad \Sigma_2 = \{x \in \mathbb{R}^n : h_2(x) = 0\},$$

$$\Sigma = \left\{ x \in \mathbb{R}^n : h(x) = 0, \ h(x) = \left[\begin{array}{c} h_1(x) \\ h_2(x) \end{array} \right] \right\}.$$

(4-1)

Then, we have

$$\begin{array}{llll} R_1 : f_1 & \text{for} & h_1 > 0 \ h_2 > 0, & R_2 : f_2 \quad \text{for} \quad h_1 < 0, \ h_2 > 0, \\ R_3 : f_3 & \text{for} & h_1 < 0, h_2 < 0, & R_4 : f_4 \quad \text{for} \quad h_1 > 0, h_2 < 0, \end{array}$$

where the f_i, $i = 1, \ldots, 4$ are smooth vector fields. For later use, we adopt the notation $\Sigma_{1,2}^{\pm}$ to denote the set of points $x \in \Sigma_{1,2}$ for which have $h_{1,2}(x) > 0$ or $h_{1,2}(x) < 0$, as indicated in Figure 4-1. We also denote the sliding vector fields of co-dimension 1 as $f_{\Sigma_{1,2}^{\pm}}$ according to each switching sub-manifold $\Sigma_{1,2}^{\pm}$.

Now, assuming that we are following a trajectory on Σ, its the attractivity can be characterized by the first and second order exit conditions, which make reference to the cases in which the flow on Σ exits and remains either in one of the sub-sliding manifolds $\Sigma_{1,2}^{\pm}$ or in

one of the subregions of the state space R_i. Then according to the Definition 2.1.2 the first and second order exit conditions can be retrieve with the conditions listed in Table **4-3** and Table **4-4**, respectively.

	Exit Conditions
From Σ to $\Sigma_1^{\pm}$	$s_2 = \pm 1$
From Σ to $\Sigma_2^{\pm}$	$s_1 = \pm 1$

Table 4-1: Utkin's equivalent control method: first-order exit conditions from Σ.

	Exit Conditions
From Σ to R_1	$s_1 = s_2 = 1$
From Σ to R_2	$s_1 = -s_2 = -1$
From Σ to R_3	$s_1 = s_2 = -1$
From Σ to R_4	$s_1 = -s_2 = 1$

Table 4-2: Utkin's equivalent control method: second-order exit conditions from Σ.

The co-dimension 2 switching manifold Σ is defined as

$$\Sigma = \left\{ x \in \mathbb{R}^n : h(x) = 0, \ h(x) = \left[\begin{array}{c} h_1(x) \\ h_2(x) \end{array} \right] \right\}. \tag{4-2}$$

For constructing the sliding vector field on Σ we can use the Filippov convex method or the equivalent control as we remark in the Section 2.1.1. However, a lack of uniqueness arises in the multimodal case by using the Filippov convex method. In particular, following Filippov's convex method [37], the dynamics along Σ are express as

$$F_\Sigma(x) = \sum_{i=1}^{4} \lambda_i(x) f_i(x), \tag{4-3}$$

where

$$\lambda_i(x) \geq 0 \wedge \sum_{i=1}^{4} \lambda_i(x) = 1, \tag{4-4}$$

under the constraint that $F_\Sigma(x)$ must be tangent to Σ, i.e.

$$\mathcal{L}_{F_\Sigma} h_i(x) = 0, \qquad i = 1, 2. \tag{4-5}$$

It is immediately clear from equation (4-3)-(4-5) that we cannot uniquely select the coefficients $\lambda_i(x)$, since we have three equations in four unknowns.

Filippov (1988) [37] and Utkin (1977) [90] acknowledged this issue and claimed that their methods can be used just in some particular cases, for example in mechanical systems where the physics of the problem itself assures a unique solution, regardless of the nominal co-dimension of the sliding surface.

In [51, 50] was introduced a new way of constructing the dynamics on Σ (hidden dynamics) which allows to model complex dry friction forces such as the *Stiction friction force* which is not captured by the classical approaches.

Next, we investigate the dynamics of two coupled mechanical oscillators with dry friction. We use the equivalent control method to model the friction dynamics due to there is no exits ambiguity in selecting the sliding vector field regarding the physics of the system. Then, we employ the hidden dynamics approach revised in Section 2.2 with the aim of modeling a more complex static friction without needing to augment the Coulomb friction with a velocity dependence.

4.2 The mechanical model

We consider a system made of two blocks of equal mass m (namely block 1 and block 2) placed on a horizontal rough plane, as shown in Figure 4-2. Each block is linked by a spring of equal stiffness k_1 to a driving mechanism moving at constant velocity V in the horizontal direction. The blocks are connected to each other by a spring of stiffness k_p. The hypothesis of blocks of equal mass and springs of equal stiffness is made for the sake of simplicity and can be relaxed at the cost of introducing additional parameters in the model.
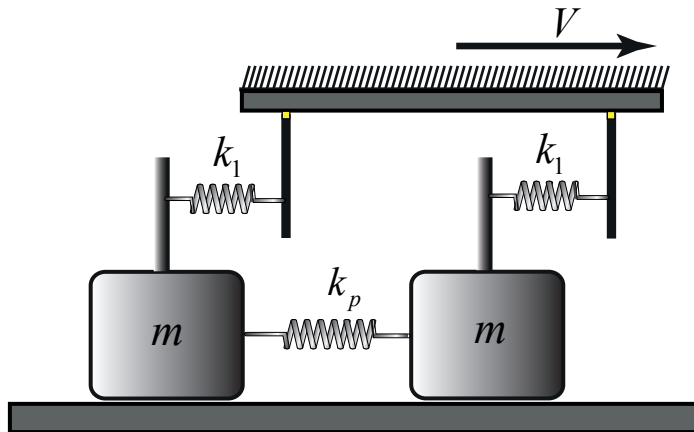
Figure 4-2: Sketch of the model.

The horizontal plane exerts a dry friction force on each block, so that they stick to the surface (sticking phase) until the elastic forces due to the springs exceed the maximum static friction force. At this point the blocks start slipping. The system can be described by the following equations of motion:

$$m\ddot{Y}_1 + k_p(Y_1 - Y_2) + k_1 Y_1 = T_1(v_{rel1})$$
$$m\ddot{Y}_2 + k_p(Y_2 - Y_1) + k_1 Y_2 = \beta T_2(v_{rel2})$$

(4-6)

where Y_1 and Y_2 denote the position coordinates of each block with respect to the velocity driver V, $T(v_{rel})$ stands for the dry friction, expressed as a function of the relative velocity $\dot{Y}_i$ of each block and the driver velocity V. According to each block, they are denoted by $v_{rel1} = V - \dot{Y}_1$ for the block 1 and $v_{rel2} = V - \dot{Y}_2$ for the block 2. The parameter β is the degree of symmetry between blocks in terms of the friction models.

Different models are proposed for the mathematical description of dry friction which mostly differ in the way the stick phase is modeled. Here, we consider two different friction laws displayed in Figure 4-3, the Coulomb's friction force which is mathematical represented by a set-valued function $\mu_F \operatorname{sgn}(v_{rel})$, defined as

$$T_c(v_{rel}) = \begin{cases} \mu_F & \text{if} \quad v_{rel} > 0 \\ [-\mu_F, \mu_F] & \text{if} \quad v_{rel} = 0 \\ -\mu_F & \text{if} \quad v_{rel} < 0 \end{cases} ,$$

(4-7)

where μ_F is the magnitude of the friction force. The other commonly used friction law is the *stiction* friction, defined as

$$T_s(v_{rel}) = \begin{cases} \mu_d & \text{if} \quad v_{rel} > 0 \\ \mu_s & \text{if} \quad v_{rel} = 0 \\ -\mu_d & \text{if} \quad v_{rel} < 0 \end{cases}$$

(4-8)

where μ_s and μ_F represent the magnitudes of the static and dynamic forces, respectively, with $\mu_s > \mu_d$. In this Chapter we use the hidden dynamics approach described in Section 2.2 to model the friction force (4-8) as a nonlinear set-valued function.
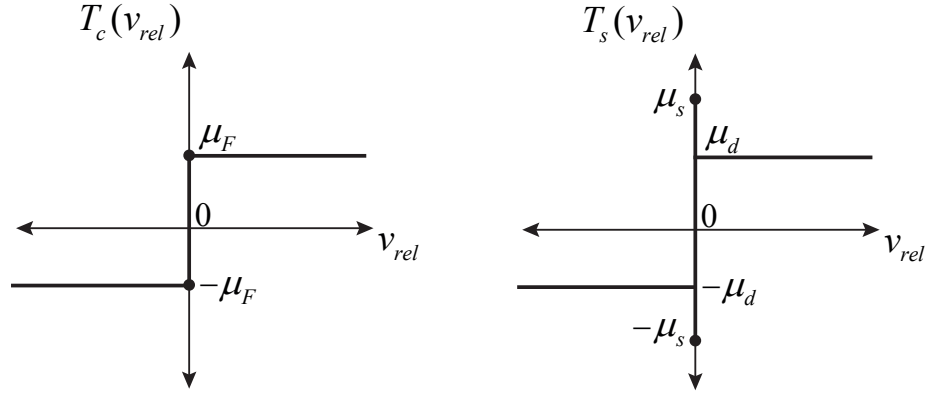
Figure 4-3: Friction models in terms of the relative velocities of each block v_{reli} : Coulomb friction, Stiction friction model.

4.2.1 Dynamic modes

According to the motions of each block the dynamics of the model (4-6) can be expressed in terms of four different modes, each one corresponding to a different ODE system. In particular, we have: mode 11 when both blocks are moving simultaneously, mode 01 and mode 10 when one of the blocks is stationary while the other is slipping and vice versa and finally mode 00 when both blocks are stationary.

4.3 Dynamics of coupled oscillators with Coulomb's friction force

Throughout this section we will characterize the conditions for the onset of motion of the two blocks regarding the Coulombs friction model. To begin with, let us rewrite the model (4-6) into the state space form by setting $x_1 = Y_1$, $x_2 = \dot{Y}_1$, $x_3 = Y_2$ and $x_4 = \dot{Y}_2$, then we have

$$\dot{x} = f(x) = \begin{pmatrix} x_2 \\ \mu_F s_1 - k_p(x_1 - x_3) - x_1 \\ x_4 \\ \beta \mu_F s_2 - k_p(x_3 - x_1) - x_3 \end{pmatrix} \tag{4-9}$$

where, s_1 and s_2 switch between -1 and 1 as $v_{rel1} = V - x_2$ and $v_{rel2} = V - x_4$ change their sign. Moreover, the switching surfaces are defined by

$$\Sigma_1 = \left\{ x \in \mathbb{R}^4 : v_{rel1} = 0 \right\}, \quad \Sigma_2 = \left\{ x \in \mathbb{R}^4 : v_{rel2} = 0 \right\}. \tag{4-10}$$

We shall now characterize the attractivity of the co-dimension 1 and 2 switching surfaces, focusing on the switching conditions from one mode to the others.

4.3.1 Slip-slip phase: mode 11

Regarding the direction of motion of each of the two blocks, the dynamics during the slip-slip phase (mode 11) are expressed by $\dot{x} = f(x)$ with

$$f_1(x) = \begin{pmatrix} x_2 \\ \mu_F - k_p(x_1 - x_3) - x_1 \\ x_4 \\ \beta\mu_F - k_p(x_3 - x_1) - x_3 \end{pmatrix}, \quad f_3(x) = \begin{pmatrix} x_2 \\ -\mu_F - k_p(x_1 - x_3) - x_1 \\ x_4 \\ -\beta\mu_F - k_p(x_3 - x_1) - x_3 \end{pmatrix} \quad (4\text{-}11)$$

where $f_1(x) \in R_1$ and $f_3(x) \in R_3$ correspond to the block moving in the same direction. In particular, $f_1(x)$ describes the forward slipping phases of the two blocks ($v_{rel1} > 0$, $v_{rel2} > 0$), while $f_3(x)$ describes the backward slipping phases ($v_{rel1} < 0$, $v_{rel2} < 0$). On the other hand, when the two blocks are moving in opposite direction they are governed by

$$f_2(x) = \begin{pmatrix} x_2 \\ -\mu_F - k_p(x_1 - x_3) - x_1 \\ x_4 \\ \beta\mu_F - k_p(x_3 - x_1) - x_3 \end{pmatrix}, \quad f_4(x) = \begin{pmatrix} x_2 \\ \mu_F - k_p(x_1 - x_3) - x_1 \\ x_4 \\ -\beta\mu_F - k_p(x_3 - x_1) - x_3 \end{pmatrix}. \quad (4\text{-}12)$$

4.3.2 Slip-stick phase: mode 10

In this mode, the block 2 is stationary while the block 1 flips between left and right slip without sticking. Thus, regarding the driver velocity V is equal to the relative velocity of block 2, i.e. x_2, the system dynamics evolve along the co-dimension 1 switching surface $\widehat{\Sigma}_2 \subset \Sigma_2$. The dynamics on $\widehat{\Sigma}$ can be retrieve using the Definition 2-15. Thus, the sliding vector field is described by

$$\dot{x} = f_{\Sigma_2^+} = \begin{pmatrix} x_2 \\ \mu_F - k_p(x_1 - x_3) - x_1 \\ x_4 \\ -k_p(x_3 - x_1) - x_3 \end{pmatrix} + \begin{pmatrix} 0 \\ 0 \\ 0 \\ \mu_F\beta \end{pmatrix} s_2, \quad \forall x \in \widehat{\Sigma}_2, \quad (4\text{-}13)$$

where s_2 is obtained by solving $\nabla h_2(x) \cdot f_{\Sigma_2^+}(x) = 0$, corresponding to

$$s_2 = \frac{k_p(x_3 - x_1) + x_3}{\beta\mu_F} \quad (4\text{-}14)$$

Replacing the "correction term" (4-14) into (4-13), we obtain

$$\dot{x} = f_{\Sigma_2^+} = \begin{pmatrix} x_2 \\ \mu_F - k_p(x_1 - x_3) - x_1 \\ x_4 \\ 0 \end{pmatrix}, \quad \forall x \in \widehat{\Sigma}_2, \tag{4-15}$$

By definition, $x_4 = v$ during sliding on Σ_2; therefore, we get the sliding vector field in mode 01 in compliance with the mechanical model (4-6):

$$f_{\Sigma_2^+} = \begin{pmatrix} x_2 \\ \mu_F - k_p(x_1 - x_3) - x_1 \\ V \\ 0 \end{pmatrix}, \quad \forall x \in \widehat{\Sigma}_2. \tag{4-16}$$

According to the exit conditions listed in Table **4-1**, the sliding motion on Σ_2 ceases when $|s_2| = 1$, i.e. either

$$k_p(x_3 - x_1) + x_3 = -\beta\mu_F \tag{4-17}$$

or

$$k_p(x_3 - x_1) + x_3 = \beta\mu_F. \tag{4-18}$$

In both cases, the system undergoes a switch in the dynamics from mode 10 to mode 11. Note that conditions (4-24) and (4-25) are in compliance with the mechanical model, that is, the force exerted by the springs must be bigger or equal than the friction exerted on the block 2 in order to it start moving.

We conclude that the mode 10 corresponds to sliding on the subset

$$\widehat{\Sigma} = \{x \in \mathbb{R}^4 : -\mu_F\beta + k_p x_1 \leq x_3(1 + k_p) \leq \beta\mu_F + k_p x_1, x_4 = V\} \subset \Sigma_2 \tag{4-19}$$

4.3.3 Stick-slip phase: mode 01

Now, we assume that the system lies in mode 01, which implies that the block 1 is in sticking phase or sliding whereas the block 2 is slipping. Again, the system undergoes a sliding motion of co-dimension 1, taking place on $\widehat{\Sigma}_1 \subset \Sigma$. The sliding dynamics reads

$$\dot{x} = f_{\Sigma_1^+} \begin{pmatrix} x_2 \\ -k_p(x_1 - x_3) - x_1 \\ x_4 \\ \mu_F\beta - k_p(x_3 - x_1) - x_3 \end{pmatrix} + \begin{pmatrix} 0 \\ \mu_F \\ 0 \\ 0 \end{pmatrix} s_1, \quad \forall x \in \widehat{\Sigma}_1 \tag{4-20}$$

where s_1 can be seen as the force that places the dynamics (4-20) into the tangent plane Σ_1. Now, by solving $\nabla h_1(x) \cdot f_{\Sigma_1^+} = 0$ for s_1, we obtain

$$s_1 = \frac{-k_p(x_1 - x_3) - x_1}{\mu_F}. \tag{4-21}$$

Finally, by replacing s_1 into (4-20), the sliding dynamics along $\widehat{\Sigma}_1$ are expressed by

$$\dot{x} = f_{\Sigma_1^+} = \begin{pmatrix} x_2 \\ 0 \\ x_4 \\ \beta\mu_F - k_p(x_3 - x_1) - x_3 \end{pmatrix}, \quad \forall x \in \widehat{\Sigma}_1. \tag{4-22}$$

By definition, $x_2 = V$ during sliding on Σ_1; therefore, we get the sliding vector field in mode 01 in compliance with the mechanical model (4-6):

$$\dot{x} = f_{\Sigma_1^+} = \begin{pmatrix} V \\ 0 \\ x_4 \\ \beta\mu_F - k_p(x_3 - x_1) - x_3 \end{pmatrix}, \quad \forall x \in \widehat{\Sigma}_1. \tag{4-23}$$

With the same reasoning as the previous section, sliding on Σ_1 ceases as soon as $|s_1| = 1$, i.e. providing that the force exerted by the springs reach the maximum friction force

$$k_p(x_1 - x_3) + x_1 = \mu_F \tag{4-24}$$

or the minimum threshold

$$k_p(x_1 - x_3) + x_1 = -\mu_F. \tag{4-25}$$

In both cases, the system undergoes a switch in the dynamics from mode 01 to mode 11 and the block 1 will eventually start to slip. Finally, we conclude that mode 01 corresponds to sliding on the subset

$$\widehat{\Sigma}_1 = \{x \in \mathbb{R}^4 : -\mu_F + x_1(1 + k_p) \leq k_p x_3 \leq \mu_F + x_1(1 + k_p), x_2 = V\} \tag{4-26}$$

4.3.4 Stick-stick phase: mode 00

When both blocks are stationary, the system dynamics take place on the co-dimension 2 sliding surface $\Sigma = \Sigma_1 \cap \Sigma_2$. In particular, the dynamics evolve in a state space region (x_1, x_3) delimited by the sticking conditions of both blocks (parallelogram), as we will see shortly. Our great interest now resides in the corner of the parallelogram that is when both

blocks start moving simultaneously, originating co-dimension 2 exit points. To retrieve the sliding dynamics along Σ, let us rewrite the system (4-9) as

$$\dot{x} = \mathcal{A}x + \mathcal{B}s_{12}, \tag{4-27}$$

where

$$\mathcal{A} = \begin{pmatrix} 0 & 1 & 0 & 0 \\ -1-k_p & 0 & k_p & 0 \\ 0 & 0 & 0 & 1 \\ k_p & 0 & -1-k_p & 0 \end{pmatrix}, \quad \mathcal{B} = \begin{pmatrix} 0 & 0 \\ \mu_F & 0 \\ 0 & 0 \\ 0 & \beta\mu_F \end{pmatrix} \tag{4-28}$$

and $s_{12} = [s_1 \ s_2]^T$ is a column vector composed by the switching parameters. In the multidimensional case, when two or more switching manifolds interact between each other, condition (2-13) becomes

$$s_{12} = -(G\mathcal{B})^{-1}G\mathcal{A}x = \begin{pmatrix} \frac{1+k_p}{\mu_F} & 0 & -\frac{k_p}{\mu_F} & 0 \\ -\frac{k_p}{\beta\mu_F} & 0 & \frac{1+k_p}{\beta\mu_F} & 0 \end{pmatrix} x \tag{4-29}$$

where the matrix G is composed by the normal vectors to each switching surface, $h_1(x) = V - x_2$, $h_2(x) = V - x_4$, corresponding to

$$G = \begin{pmatrix} 0 & -1 & 0 & 0 \\ 0 & 0 & 0 & -1 \end{pmatrix}. \tag{4-30}$$

Now, by replacing (4-29) into (4-27), the sliding dynamics along Σ are giving by

$$\dot{x} = \mathcal{A}x + \mathcal{B}s_{12} = \begin{pmatrix} 0 & 1 & 0 & 0 \\ 0 & 0 & 0 & 0 \\ 0 & 0 & 0 & 1 \\ 0 & 0 & 0 & 0 \end{pmatrix} x, \quad \forall x \in \Sigma = \Sigma_1 \cap \Sigma_2. \tag{4-31}$$

By definition, $x_2 = x_4 = V$ during sliding on Σ; therefore, we get the sliding vector field in mode 00 in compliance with the mechanical model (4-6):

$$\dot{x} = f_\Sigma = \begin{pmatrix} V \\ 0 \\ V \\ 0 \end{pmatrix}, \quad \forall x \in \Sigma = \Sigma_1 \cap \Sigma_2. \tag{4-32}$$

The system will evolve in mode 00 until the block 1 or block 2 or both start to slip, entering mode 10/01 or mode 11, respectively.

An alternative way to retrieve the sliding vector field on Σ is considering the bilinear combination method. The motion along the sliding surface is defined as

$$f_\Sigma = (1-a)(1-b)\,f_1 + b(1-a)\,f_2 + a(1-b)\,f_3 + ab\,f_4, \tag{4-33}$$

where the coefficients of the combination are the solution of the system

$$
\begin{cases}
(1-a)(1-b)\,\mathcal{L}_{f_1}h_1 + b(1-a)\,\mathcal{L}_{f_2}h_1 + a(1-b)\,\mathcal{L}_{f_3}h_1 + ab\,\mathcal{L}_{f_4}h_1 = 0 \\
(1-a)(1-b)\,\mathcal{L}_{f_1}h_2 + b(1-a)\,\mathcal{L}_{f_2}h_2 + a(1-b)\,\mathcal{L}_{f_3}h_2 + ab\,\mathcal{L}_{f_4}h_2 = 0
\end{cases}. \tag{4-34}
$$

We obtain

$$
a = \frac{\beta\mu_F - x_3(1+k_p) + k_p x_1}{2\beta\mu_F}, \qquad b = \frac{x_3(1+k_p+k_p\beta) - x_1(k_p+\beta+k_p\beta)}{2[x_3(1+k_p)-k_p x_1]}. \tag{4-35}
$$

Thus, replacing Eq. (4-35) in Eq. (4-33), we get

$$
f_\Sigma = \begin{pmatrix} V \\ 0 \\ V \\ 0 \end{pmatrix}, \qquad \forall x \in \Sigma = \Sigma_1 \cap \Sigma_2. \tag{4-36}
$$

in agreement with the results provided by the equivalent control method (4-32). We now wish to evaluate the first-order exit conditions

$$
\mathcal{L}_{f_{\Sigma_1^+}} h_2 = 0, \qquad \mathcal{L}_{f_{\Sigma_1^-}} h_2 = 0, \tag{4-37}
$$

$$
\mathcal{L}_{f_{\Sigma_2^+}} h_1 = 0, \qquad \mathcal{L}_{f_{\Sigma_2^-}} h_1 = 0, \tag{4-38}
$$

corresponding to trajectories leaving Σ and remaining on one of the four sub-sliding manifolds Σ_1^+, Σ_1^-, Σ_2^+ and Σ_2^-, respectively. All cases are summarized in Table 4-3.

	Exit conditions	Switching dynamics
From Σ to $\Sigma_1^\pm$	$k_p(x_3 - x_1) + x_3 = \pm\mu_F\beta$	mode 00 $\rightarrow$ mode 01
From Σ to $\Sigma_2^\pm$	$k_p(x_1 - x_3) + x_1 = \pm\mu_F$	mode 00 $\rightarrow$ mode 10

Table 4-3: First order exit conditions from sliding on Σ.

The exit conditions from Σ to $\Sigma_2^\pm$ and from Σ to $\Sigma_1^\pm$ define the onset of motion of block 1 and block 2 given in (4-24) - (4-18), respectively. We now turn to the second-order exit conditions

$$
\mathcal{L}_{f_1}h_1 = \mathcal{L}_{f_1}h_2 = 0, \qquad \mathcal{L}_{f_2}h_1 = \mathcal{L}_{f_2}h_2 = 0, \tag{4-39}
$$

$$
\mathcal{L}_{f_3}h_1 = \mathcal{L}_{f_3}h_2 = 0, \qquad \mathcal{L}_{f_4}h_1 = \mathcal{L}_{f_4}h_2 = 0, \tag{4-40}
$$

corresponding to trajectories leaving Σ and entering one of the four regions R_1, R_2, R_3 and R_4, respectively. All cases are summarized in Table 4-4 and coincide with switching from

mode 00 to mode 11.

	Exit Conditions	Switching dynamics
From Σ to R_1	$(2k_p + 1)(x_1 - x_3) = \mu_F(1 + \beta)$	mode $00 \to R_1$
From Σ to R_2	$(1 - 2k_p)(x_1 - x_3) = \mu_F(1 - \beta)$	mode $00 \to R_2$
From Σ to R_3	$2k_p(x_1 - x_3) + x_1 - x_3 = \mu_F(1 + \beta)$	mode $00 \to R_3$
From Σ to R_4	$-(2k_p - 1)(x_1 - x_3) = -\mu_F(1 + \beta)$	mode $00 \to R_4$

Table 4-4: Second order exit conditions from Σ.

Finally, accordingly to the conditions listed in Tables 4-3 and 4-4, we conclude that the region of phase space including the states in which both blocks are stationary (sticking region) is a parallelogram in the (x_1, x_3) plane, enclosed between the lines

$$\alpha x_3 - x_1(1 + k_p) = \pm\mu_F, \qquad k_p x_1 - x_3(1 + k_p) = \pm\beta\mu_F \tag{4-41}$$

The system passes from mode 00 to mode 11 when the orbit reaches one of the vertices

$$P_1 = \left(\frac{\mu_F(k_p\beta + k_p + 1)}{1 + 2k_p}, \frac{\mu_F(k_p\beta + k_p + \beta)}{1 + 2k_p} \right) \tag{4-42}$$

$$P_2 = \left(\frac{\mu_F(k_p\beta - k_p - 1)}{1 + 2k_p}, \frac{\mu_F(k_p\beta - k_p + \beta)}{1 + 2k_p} \right) \tag{4-43}$$

$$P_3 = \left(-\frac{\mu_F(k_p\beta + k_p + 1)}{1 + 2k_p}, -\frac{\mu_F(k_p\beta + k_p + \beta)}{1 + 2k_p} \right) \tag{4-44}$$

$$P_4 = \left(-\frac{\mu_F(k_p\beta - k_p - 1)}{1 + 2k_p}, -\frac{\mu_F(k_p\beta - k_p + \beta)}{1 + 2k_p} \right) \tag{4-45}$$

The sticking region is displayed in Figure 4-4. Finally, we note that each of the conditions listed in Table 4-4 identify one of the vertices of the sticking region: specifically, the system leaves Σ and enters the region R_i at the point P_i.

4.4 Dynamics of coupled oscillators with Stiction friction force

We shall now address the analysis of the spring block system presented in the previous Section regarding the stiction friction model (4-8). By doing so, we exploit the hidden dynamics approach revised in Section 2.2 to mathematical describe such a friction law. The
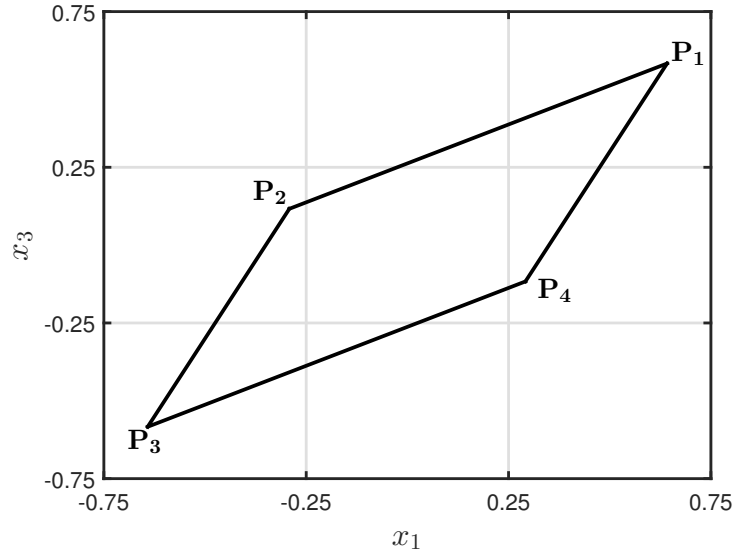
Figure 4-4: The sticking region of the system ($k_p = 1$, $\beta = 0.75$, $\mu_F = 0.7$).

state variables, the parameters and the tangential forces on the blocks are the same as described earlier. Accordingly, the system (4-6) is written as

$$\dot{x} = f(x) = \begin{pmatrix} x_2 \\ \mu_{d1} s_1 - \mu_1 s_1 (1 - s_1^2) - k_p(x_1 - x_3) - x_1 \\ x_4 \\ \beta \mu_{d2} s_2 - \beta \mu_2 s_2 (1 - s_2^2) - k_p(x_3 - x_1) - x_3 \end{pmatrix} \tag{4-46}$$

where, s_1 and s_2 switch between -1 and 1 as $v_{rel1} = x_2 - V$ and $v_{rel2} = x_4 - V$ change their sign. Moreover, the switching surfaces are defined by

$$\Sigma_1 = \left\{ x \in \mathbb{R}^4 : v_{rel1} = 0 \right\}, \quad \Sigma_2 = \left\{ x \in \mathbb{R}^4 : v_{rel2} = 0 \right\}. \tag{4-47}$$

Similar as in the above analysis, the dynamics of the model are described by the four dynamical modes, each one corresponding to a different ODE system. Due to the hidden approach is consistent with the Filippov analysis outside of the switching manifold Σ, we exclude the analysis of the mode 11, since is equal to performed analysis in the above section. In the following we will characterize the attractivity of the co-dimension 1 and 2 switching surfaces and their respective exit and entry points, focusing on the switching conditions from one mode to the others.

4.4.1 Slip-stick phase: mode 10

This mode occurs when the block 1 is slipping while the block 2 is stationary. Note that, in this mode the system becomes 4-dimensional with a co-dimension 1 switching surface given by $\Sigma_2 = \{x \in \mathbb{R}^4 : v_{rel2} = 0\}$. We consider forward slipping motion, that is only when the block 1 is moving in the positive direction, regarding $v_{rel1} > 0$, then we have

$$\dot{x} = \begin{pmatrix} x_2 \\ \mu_{d1} - k_p(x_1 - x_3) - x_1 \\ x_4 \\ \beta\mu_{d2}s_2 - \beta\mu_2 s_2(1 - s_2^2) - k_p(x_3 - x_1) - x_3 \end{pmatrix}, \quad s_2 \in [-1, 1]. \tag{4-48}$$

The sliding dynamics of (4-48) can be derived by following the Definition 2.1.2. As a consequence we have 3 solutions for s_2^*, that solve

$$0 = -\beta\mu_{d2}s_2 - \beta\mu_2 s_2(1 - s_2^2) - k_p(x_3 - x_1) - x_3, \tag{4-49}$$

each one, defining a sliding mode on Σ. The vector field underlying such a dynamics is then given by

$$\dot{x} = f_{\Sigma_2^+} = \begin{pmatrix} x_2 \\ -\mu_{d1} - k_p(x_1 - x_3) - x_1 \\ V \\ 0 \end{pmatrix}. \tag{4-50}$$

In order to determine whether the sliding modes are attracting or repelling, we will analyze the critical manifold of the regularized version of (4-48). Thus, by introducing the regularization parameter ε_2 and setting $z_2 = v_{rel2}/\varepsilon_2$ the system (4-48) becomes

$$\begin{aligned} \dot{x}_1 &= x_2 \\ \dot{x}_2 &= -\mu_{d1} - k_p(x_1 - x_3) - x_1 \\ \dot{x}_3 &= \varepsilon_2 z_2 - V \\ \varepsilon_2 \dot{z}_2 &= -\beta\mu_{d2}z_2 - \beta\mu_2 z_2(1 - z_2^2) - k_p(x_3 - x_1) - x_3 \end{aligned} \tag{4-51}$$

Now, by analyzing the limiting dynamics of the system (4-51), that is when $\varepsilon_2 = 0$, we find that the sliding dynamics on block 2 take place on the critical manifold defined by

$$\mathbb{C}_0 = \left\{ (x_1, x_2, x_3, z_2) \in \mathbb{R}^4 : -\beta\mu_{d2}z_2 - \beta\mu_2 z_2(1 - z_2^2) - \alpha(x_3 - x_1) - x_3 = 0 \right\}. \tag{4-52}$$

An illustration of the blowing up process regarding the sliding dynamics evolving along $\mathbb{C}_0$ is displayed in Figure 4.4.1. Note that the attractive region is delimited by the black dotted line which exactly corresponds to the point in which the critical manifold loses hyperbolicity. Therefore, once the flow reaches $\mathbb{C}_0$, it evolves until the manifold loses its attractivity, which
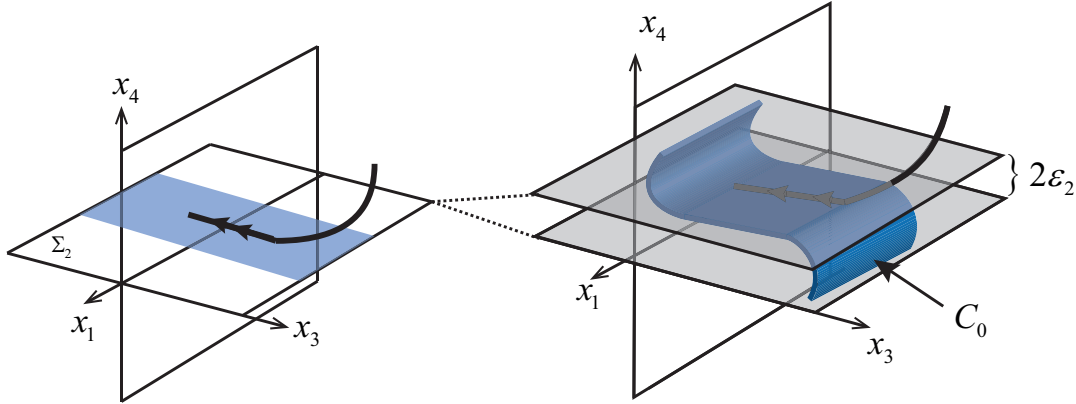
Figure 4-5: Sketch of a trajectory evolving along the critical manifold $\mathbb{C}_0$. Giving an initial condition x^+ outside of the switching layer (fast dynamics), the trajectory reaches z_2^+ (blue line) and then slides until the surface loses attractivity, that is when $z_2 = z_2^*$

is verified through the following relation

$$\frac{\partial}{\partial z_2}\left(-\beta\mu_{d2}z_2 - \beta\mu_2 z_2(1 - z_2^2) - k_p(x_3 - x_1) - x_3\right) = 0. \tag{4-53}$$

This occurs at

$$z_2^* = \pm\sqrt{\frac{\mu_{d2} + \mu_2}{3\mu_2}} \tag{4-54}$$

Now, replacing (4-54) into the critical manifold (4-52) we obtain the sliding region on Σ_2 given by

$$\widehat{\Sigma}_2 = \left\{x \in \mathbb{R}^4 : -\beta\left[\frac{2\mu_{d2} + 2\mu_2}{3}\right]\sqrt{\frac{\mu_{d2} + \mu_2}{3\mu_2}} \leq -k_p(x_3 - x_1) - x_3 \leq \beta\left[\frac{2\mu_{d2} + 2\mu_2}{3}\right]\sqrt{\frac{\mu_{d2} + \mu_2}{3\mu_2}}\right\}$$

The above relation is also consistent with the fact that the block 2 has to reach the maximun friction force μ_{s2} for starting moving, when this happens, the system goes from mode 10 to mode 11. Note that the sliding phase has a nonlinear growth, mainly induced by the selection of the $G(s)$ function.

A further characterization of the sliding phase can be achieved considering that, since the dynamics must take place on the critical manifold (4-52), the derivative with respect to the time

$$\frac{\partial}{\partial t}\left(-\beta\mu_{d2}z_2 - \beta\mu_2 z_2(1 - z_2^2) - k_p(x_3 - x_1) - x_3\right) \tag{4-55}$$

must be equal to zero throughout sliding. Thus, we have

$$\dot{z}_2 = \frac{V - k_p v_{rel1}}{-\beta\mu_{d2} - \beta\mu_2 + 3z_2^2} \tag{4-56}$$

where we took into account the definition of v_{rel1} and also that $\dot{x}_3 = x_4 = V$ during mode 10. A peculiar feature stands out: the rate of change of z_2 depends on the relative velocity v_{rel1} of block 1, reflecting the interaction of the blocks via the coupling spring. What is more, we notice that the sign of $\dot{z}_2$ is determined by the sign of v_{rel1}: accordingly, the slow dynamics on the critical manifold evolves towards the exit condition $z_2 = z_2^*$ or $z_2 = -z_2^*$ depending on the direction of motion of block 1. This in turn determines the specific region of the state space R_i in which the trajectory enters after leaving Σ_2. The four possible cases are listed in Table 4-5.

	$z_2 = z_2^*$	$z_2 = -z_2^*$
$v_{rel1} > 0$	$\Sigma_2 \rightarrow R_1$	$\Sigma_2 \rightarrow R_2$
$v_{rel1} < 0$	$\Sigma_2 \rightarrow R_3$	$\Sigma_2 \rightarrow R_4$

Table 4-5: Switching conditions from mode 10 to mode 11 according to the nonlinear sliding analysis.

4.4.2 Stick-slip phase: mode 01

This mode arises when the block 1 is stationary while the block 2 is slipping. Here we have also a 4 - dimensional system with one switching manifold, but now with respect to the v_{rel1},

$$\Sigma_1 = \left\{ x \in \mathbb{R}^4 : v_{rel1} = 0 \right\}.$$

We consider forward slipping for the second block $(v_{rel2} > 0)$, so that the system (4-46) becomes

$$\dot{x} = \begin{pmatrix} x_2 \\ -\mu_{d1}s_1 - \mu_1 s_1(1 - s_1^2) - k_p(x_1 - x_3) - x_1 \\ x_4 \\ -\beta\mu_{d2} - k_p(x_3 - x_1) - x_3 \end{pmatrix}, \quad s_1 \in [-1, 1], \qquad (4\text{-}57)$$

with s_1 varying from -1 to 1 as the relative velocity v_{rel1} changes its sign. The sliding dynamics along Σ_1 regarding Definition 2.1.2 provides 3 solutions for s_1^* which satisfy

$$0 = -\mu_{d1}s_1 - \mu_1 s_1(1 - s_1^2) - k_p(x_1 - x_3) - x_1. \qquad (4\text{-}58)$$

By replacing the values of s_1^* into equation (4-57) we obtain the sliding vector field

$$\dot{x} = f_{\Sigma_1^+} = \begin{pmatrix} V \\ 0 \\ x_4 \\ -\beta\mu_{d2} - k_p(x_3 - x_1) - x_3 \end{pmatrix}. \qquad (4\text{-}59)$$

Again, multiple sliding regimes arise on Σ_1, to characterize them we will use the slow and fast analysis. Thereby, we introduce a small parameter ε_1 and then by setting $z_1 = v_{rel1}/\varepsilon_1$ we get

$$\begin{aligned}
\dot{x}_1 &= \varepsilon_1 z_1 - V \\
\varepsilon_1 \dot{z}_1 &= -\mu_{d1} z_1 - \mu_1 z_1 (1 - z_1^2) - k_p(x_1 - x_3) - x_1 \\
\dot{x}_3 &= x_4 \\
\dot{x}_4 &= -\beta \mu_{d2} - k_p(x_3 - x_1) - x_3
\end{aligned}$$

(4-60)

By analyzing the regularized system (4-60) for $\varepsilon_1 = 0$ we find that the sliding dynamics on Σ_1 take place on the critical manifold defined by

$$\mathbb{C}_1 = \left\{ (x_1, z_1, x_3, x_4) \in \mathbb{R}^4 : -\mu_{d1} z_1 - \mu_1 z_1 (1 - z_1^2) - k_p(x_1 - x_3) - x_1 = 0 \right\} \quad \text{(4-61)}$$

which has a geometric interpretation illustrated in Figure 4.4.2.
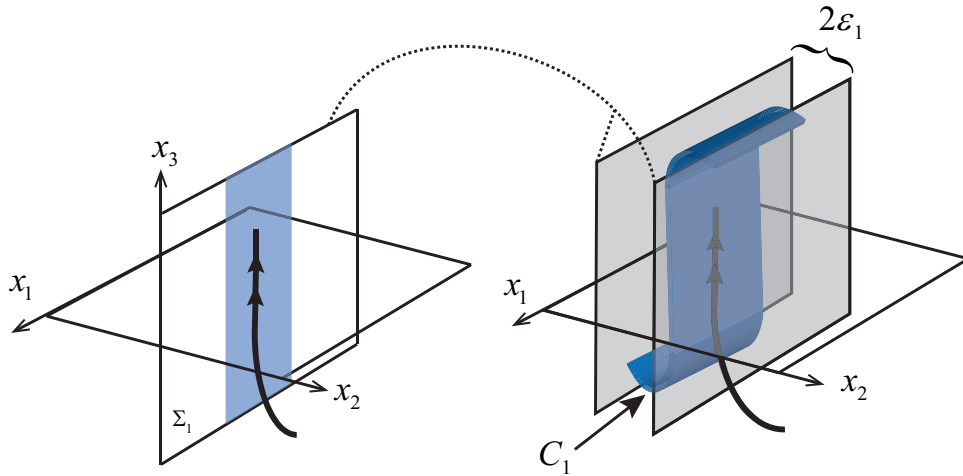
Figure 4-6: Sketch of a trajectory evolving along the critical manifold $\mathbb{C}_1$. Giving an initial condition x^* outside of the switching layer (fast dynamics), the trajectory reaches $\mathbb{C}_1$ (blue line) and then slides until the surface loses attractivity, that is when $z_1 = z_1^*$

Similarly, once the flow reaches the critical manifold $\mathbb{C}_1$, it remains there up to $\mathbb{C}_1$ loses hyperbolicity, that is when

$$\frac{\partial}{\partial z_1} \left(-\mu_{d1} z_1 - \mu_1 z_1 (1 - z_1^2) - k_p(x_1 - x_3) - x_1 \right) = 0 \quad \text{(4-62)}$$

This occurs at

$$z_1^* = \pm \sqrt{\frac{\mu_{d1} - \mu_1}{3\mu_1}} \quad \text{(4-63)}$$

Now, by replacing (4-63) into the critical manifold (4-61) we obtain the sliding region on Σ_1, expressed by

$$\widehat{\Sigma}_1 = \left\{ x \in \mathbb{R}^4 : -\left[\frac{2\mu_{d1} - 2\mu_1}{3}\right] \sqrt{\frac{\mu_{d1} - \mu_1}{3\mu_1}} \leq -k_p(x_1 - x_3) - x_1 \leq \left[\frac{2\mu_{d1} - 2\mu_1}{3}\right] \sqrt{\frac{\mu_{d1} - \mu_1}{3\mu_1}} \right\}$$

The sliding region $\widehat{\Sigma}_1$ express the fact that the block 1 has to reach the maximum friction force μ_{s1} for starting moving, when the system reach this threshold the transition from mode 01 to mode 11 occurs.

On the other hand, an extra characterization of the sliding phase can be achieved considering that, since the dynamics must take place on the critical manifold (4-61), the derivative with respect to the time

$$\frac{\partial}{\partial t}\left(-\mu_{d1}z_1 - \mu_1 z_1(1 - z_1^2) - k_p(x_1 - x_3) - x_1\right) \tag{4-64}$$

must vanish throughout sliding, for the dynamics to evolve on the critical manifold (4-61). Accordingly, we find

$$\dot{z}_1 = \frac{V - k_p v_{rel2}}{-\mu_{d1} - \mu_1 + 3z_1^2} \tag{4-65}$$

where we took into account the definition of v_{rel2} and also that $\dot{x}_1 = x_2 = V$ during mode 01. The interaction between the blocks emerges from the dependence of the rate $\dot{z}_1$ on the relative velocity v_{rel2} of block 2. Specifically, the sign of $\dot{z}_1$ is determined by the sign of v_{rel2}, so that the slow dynamics on the critical manifold evolves towards the exit condition $z_1 = z_1^*$ or $z_1 = -z_1^*$ depending on the direction of motion of block 2. This in turn determines the partition of the state space R_i in which the trajectory enters after leaving Σ_1, as summarized in Table 4-6.

	$z_1 = z_1^*$	$z_1 = -z_1^*$
$v_{rel2} > 0$	$\Sigma_1 \to R_1$	$\Sigma_1 \to R_4$
$v_{rel2} < 0$	$\Sigma_1 \to R_2$	$\Sigma_1 \to R_3$

Table 4-6: Switching conditions from mode 01 to mode 11 according to the nonlinear sliding analysis.

4.4.3 Stick-stick phase: mode 00

Now we focus on the 4-dimensional system with a co-dimension 2 switching surface Σ, corresponding to stationary blocks. In this mode, the sliding dynamics take place on the intersection of both surfaces, that is

$$\Sigma = \Sigma_1 \cap \Sigma_2 = \left\{ x \in \mathbb{R}^4 : v_{rel1} = 0, \ v_{rel2} = 0 \right\}$$

The corresponding dynamics along the intersection are given by

$$\dot{x} = f_\Sigma = \begin{pmatrix} x_2 \\ -\mu_{d1}s_1 - \mu_1 s_1(1 - s_1^2) - k_p(x_1 - x_3) - x_1 \\ x_4 \\ -\beta\mu_{d2}s_2 - \beta\mu_2 s_2(1 - s_2^2) - k_p(x_3 - x_1) - x_3 \end{pmatrix}, \quad s_1 \in [-1, 1], \quad s_2 \in [-1, 1]$$

(4-66)

where s_1 and s_2 are the solutions of the equations

$$\begin{cases} 0 = -\mu_{d1}s_1 - \mu_1 s_1(1 - s_1^2) - k_p(x_1 - x_3) - x_1 \\ 0 = -\beta\mu_{d2}s_2 - \beta\mu_2 s_2(1 - s_2^2) - k_p(x_3 - x_1) - x_3 \end{cases}$$

(4-67)

Note that, in this case there exist 9 possible solutions for the pair (s_1, s_2), all of them yielding to

$$\dot{x} = f_\Sigma = \begin{pmatrix} V \\ 0 \\ V \\ 0 \end{pmatrix}$$

(4-68)

The multiple solutions of (4-67) provide conditions linked with the exit conditions of Σ and also with the sliding mode. These conditions will be more evident from the point of view of slow and fast systems. Thereby, to blow up Σ, we introduce the small parameters ε_1 and ε_2 and then we set $z_1 = v_{rel1}/\varepsilon_1$ and $z_2 = v_{rel2}/\varepsilon_2$. The resulting dynamics are described by the multiple time scale system

$$\begin{aligned} \dot{x}_1 &= \varepsilon_1 z_1 - V \\ \varepsilon_1 \dot{z}_1 &= -\mu_{d1}z_1 - \mu_1 z_1(1 - z_1^2) - k_p(x_1 - x_3) - x_1 \\ \dot{x}_3 &= \varepsilon_2 z_2 - V \\ \varepsilon_2 \dot{z}_2 &= -\beta\mu_{d2}z_2 - \beta\mu_2 z_2(1 - z_2^2) - k_p(x_3 - x_1) - x_3 \end{aligned}$$

(4-69)

The limit dynamics of (4-69), for $\varepsilon_1 = 0$ and $\varepsilon_2 = 0$, provide a 4-dimensional critical manifold $\mathbb{C}_\Sigma$, which can be rewrite in terms of the static friction over two block

$$\mathbb{C}_\Sigma = \left\{ (x_1, z_1, x_3, z_2) \in \mathbb{R}^4 : -\hat{F}_{k_1} + \beta\hat{F}_{k_2} - 2k_p(x_1 - x_3) - x_1 + x_3 = 0 \right\}$$

(4-70)

where

$$\hat{F}_{k1} = -\mu_{d1}z_1 - \mu_1 z_1(1 - z_1^2), \qquad \hat{F}_{k2} = \mu_{d2}z_2 - \beta\mu_2 z_2(1 - z_2^2)$$

Expression (4-70) reflects the fact that, during a global sticking phase, friction on each block evolves in order to counteract the effect of both the external loading (x_1, x_3) and the force exerted via the coupling spring.

Now, in order to characterize the attractivity of the hyper-surface $\mathbb{C}_\Sigma$, we evaluate the eigenvaues of Jacobian matrix $J = \partial\mathbb{C}_\Sigma/\partial z$,

$$J = \begin{pmatrix} -\mu_{d1} - \mu_1 + 3\mu_1 z_1^2 & 0 \\ 0 & -\beta\mu_{d2} - \beta\mu_2 + 3\beta\mu_2 z_2^2 \end{pmatrix}.$$

where the eigenvalues are given by the real numbers

$$\lambda_1 = -\mu_{d1} - \mu_1 + 3\mu_1 z_1^2, \qquad \lambda_2 = -\beta\mu_{d2} - \beta\mu_2 + 3\beta\mu_2 z_2^2, \tag{4-71}$$

Therefore, the stability of C_Σ is assured if both λ_1 and λ_2 are negative, which yields to

$$-z_1^* < z_1 < z_1^* \quad \wedge \quad -z_2^* < z_2 < z_2^*. \tag{4-72}$$

Hence, sliding on the critical manifold (4-70) is attractive in the subset (4-72) and unstable elsewhere. A detailed characterization of stability in the z_1, z_2 plane is outlined in Table 4-7.

	$z_2 < -z_2^*$	$-z_2^* < z_2 < z_2^*$	$z_2 > -z_2^*$
$z_1 < -z_1^*$	Unstable Nodes	Saddles	Unstable nodes
$-z_1^* < z_1 < z_1^*$	Saddles	Stable nodes	Saddles
$z_1 > -z_1^*$	Unstable Nodes	Saddles	Unstable nodes

Table 4-7: Stability of sliding modes on the critical manifold corresponding to mode 00.

Accordingly, the critical manifold (4-70) can lose attractivity in two ways. First (unstable nodes), as soon as one of the following four conditions is reached:

$$z_1 = \pm z_1^* \quad \vee \quad z_2 = \pm z_2^* \tag{4-73}$$

which are consistent with the co-dimension 2 exit conditions. Second (Saddles), when the flow leaves Σ to enter in a co-dimension 1 surface. At this point, either block 1 or block 2 is in the sticking phase ($-z_{1,2}^* < z_{1,2} < z_{1,2}^*$), while the other is slipping (forward $z_{1,2} > -z_{1,2}^*$ or backward $z_{1,2} < z_{1,2}^*$). The conditions on z_1 and z_2 with respect to the state space partition and its corresponding vector field after switch from Σ are listed in Table 4-8.

	$z_2 < -z_2^*$	$-z_2^* < z_2 < z_2^*$	$z_2 > -z_2^*$
$z_1 < -z_1^*$	$R_3 : f_3$	$\Sigma_2^- : f_{\Sigma_2^-}$	$R_2 : f_2$
$-z_1^* < z_1 < z_1^*$	$\Sigma_1^- : f_{\Sigma_1^-}$	$\hat{\Sigma} : f_\Sigma$	$\Sigma_1^+ : f_{\Sigma_1^+}$
$z_1 > -z_1^*$	$R_4 : f_4$	$\Sigma_2^+ : f_{\Sigma_2^+}$	$R_1 : f_1$

Table 4-8: Exit conditions from the co-dimension 2 surface Σ

We can also characterize the switching from mode 00 to the others, as displayed in Table **4-9**. The blank spaces represent the conditions for which the blocks experiment backward slipping, which have not meaning from the physical point of view.

	$z_2 < -z_2^*$	$-z_2^* < z_2 < z_2^*$	$z_2 > -z_2^*$
$z_1 < -z_1^*$	——	——	——
$-z_1^* < z_1 < z_1^*$	——	mode 00	mode 01
$z_1 > -z_1^*$	——	mode 10	mode 11

Table 4-9: Switching conditions with respect to the dynamics modes.

Once again, we can gain an additional understanding of the characteristics of the sliding phase by taking the time derivative of the critical manifold (4-70) and setting it equal to zero. Subsequently, we can write the slow subsystem for z_1 and z_2 as

$$\begin{pmatrix} \dot{z}_1 \\ \dot{z}_2 \end{pmatrix} = V \begin{pmatrix} \frac{1}{\mu_{d1}+\mu_1-3\mu_1 z_1^2} \\ \frac{1}{\beta(\mu_{d2}+\mu_2-3\mu_2 z_2^2)} \end{pmatrix} \tag{4-74}$$

integrated by the condition $\dot{x}_1 = \dot{x}_3 = V$ when $\varepsilon_1 = 0$ and $\varepsilon_2 = 0$. From Eq. (4-74), we notice that the rates $\dot{z}_1$ and $\dot{z}_2$ increase with V: in fact, the condition for the onset of motion is reached faster if the velocity of the external loading is increased. What is more, a larger β determines a smaller $\dot{z}_2$ with respect to $\dot{z}_1$, reflecting the greater resistance to motion of friction on block 2 with respect to friction on block 1.

Finally, we noted that the effect of the external loading, forces the system to ignore some of the exit conditions, see Table **4-9**.

4.5 Summary

The analysis of the coupled mechanical oscillators shown that the ambiguity in selecting the sliding vector field regarding the Filippov convex method or the equivalent control does not appear. However the typical behavior such that stick-slip oscillations is not capture by these approaches. Instead, by adjusting the nonlinear switching terms we can introduce a difference between of the static and dynamic friction inducing the stick slip effect, without needing to augment the Coulomb friction with a velocity dependence. Next Chapter we further explore the effects of multiple switches from the point of view of synchronization. In particular we will analyze the convergence of a network of N friction oscillators via Lyapunov and contraction analysis.

Synchronization in Networks of Dry Friction Oscillators

In Chapter 4 we characterized the stick-slip dynamics of a Filippov system of co-dimension 2. As an important application we considered two dynamically coupled mechanical oscillators subject to dry friction. Now, we focus on the study of coupled friction oscillators from the point of view of synchronization, where the key problem is to steer the collective dynamics of a network of friction oscillators towards a common behavior.

In this chapter we present an extensive numerical analysis for studying synchronization in chaotic friction oscillators, characterizing the influence of dynamic coupling and providing an estimation of the synchronization region in terms of the coupling parameters. Initially, we consider the simple case of two coupled oscillators, then we extend the analysis to the case of larger networks of coupled systems with different network topologies. Moreover preliminary analytical results of the convergence of a network of N friction oscillators based on contraction analysis are presented. The obtained results are validated through a representative example.

5.1 Problem statement

Coupled mechanical oscillators exhibit different types of behavior: stick-slip motion, chaotic regimes and fixed points, hence they have been used for comprehend many physical phenomena, e.g. formation of traffic jams in a single-lane highway traffic [49], distribution

of earthquakes [14], suspension dynamics in vehicles [4]. It is then important to under-stand not only the single dynamics but also the collective behavior of two or more of these systems. There exist an extensive literature in the field of friction and stick slip systems [77, 5, 4, 92, 10], master-slave synchronization [74, 81, 93] however very few authors have worked on synchronization of stick-slip motion by just interconnect the agents through a communication protocol or coupling scheme [16, 17, 89, 78].

Here we consider a network of N identical friction oscillators governed by second order dynamics of the form

$$\dot{x}_i(t) = \begin{bmatrix} x_{i2}(t) \\ -k_1 x_{i1}(t) + T(v - x_{i2}(t)) + F\cos(\omega t) \end{bmatrix} + u_i(t), \quad \forall i \in [1, N]. \qquad (5\text{-}1)$$

where $x_{i1}(t), x_{i2}(t) \in \mathbb{R}^2$ denote the position and velocity of the ith oscillator, respectively. The function $T(v - x_{i2})$ models the friction force and it is defined in terms of the relative velocity $v_{rel} = v - x_{i2}$.

The systems are periodically excited by a force of amplitude F and frequency ω and $u_i(t)$ is the input through which the state of the i-th agent is affected by that of its neighbors.

The aim is to study the emergence of synchronization by considering different coupling dynamics. Different coupling schemes have been reported in the literature [2, 48], however the most of them are not physically implementable. In what follows, we will explore the effects of two possible coupling dynamics: static coupling which is mathematical described by

$$u_i(t) = \begin{bmatrix} 0 \\ k_p \sum_{j=1}^{N} (x_{i1}(t) - x_{j1}(t)) \end{bmatrix}, \qquad (5\text{-}2)$$

with k_p being a positive constant denoting the coupling gain. Physically this scheme represents that all oscillators are connected by springs of stiffness k_p and therefore they adjust their accelerations according to the position mismatches between their neighbors. The dynamic coupling incorporate to the network damping terms such that all oscillations adjust their accelerations with respect to their velocities mismatches, then we have

$$u_i(t) = \begin{bmatrix} 0 \\ k_d \sum_{j=1}^{N} (x_{i2}(t) - x_{j2}(t)) \end{bmatrix}, \qquad (5\text{-}3)$$

where the parameter k_d denotes the dynamic coupling strength. The problems addressed in this Chapter are

(i) To study the effect of dynamic coupling in networks of chaotic friction oscillators.

(ii) To investigate how the topology of the network changes the parameter region where synchronization can be attained.

(iii) To find sufficient conditions ensuring synchronization in networks of dry friction oscillators.

To address these issues, we perform numerical integrations making use of the regularization of PWS systems approach introduced in Section 2.2.1. Thus, by fixing an initial condition, we integrate the system during a time interval $[0\ T]$, known to have the transient solutions settled. Next, we assess synchronization according to the error between trajectories of all nodes $e(t) = [e_1(t)\, e_2(t), \ldots, e_N(t)]^T$, defined more explicitly as

$$e_i(t) = x_i(t) - \frac{1}{N}\sum_{j=1}^{N} x_j(t). \tag{5-4}$$

Hence, we say that the network (5-1) achieves complete synchronization if

$$\lim_{x \to \infty} \|e(t)\|_2 = 0.$$

The estimation of the synchronization charts is obtained by performing numerical integrations at each point of a selected region of the parameters k_p and k_d.

5.2 Synchronization in two coupled chaotic friction oscillators

In this section, we consider the two coupled friction oscillators shown in Figure 5-1. The system is composed by two blocks of equal mass m which are supported by a belt moving with constant velocity v. The blocks are interconnected with each other by a dynamic and static coupling functions (5-2)-(5-3), and both are subject to the same external harmonic force of magnitude F and frequency ω.

The state space equations governing the dynamics of the two coupled oscillators can be expressed in the form (5-1) as

$$\dot{x}_i(t) = \begin{bmatrix} x_{i2}(t) \\ -x_{i1}(t) + T(1 - x_{i2}(t)) + F\cos(\omega t) - k_p \sum_{j=1}^{2}(x_{i1}(t) - x_{j1}(t)) - k_d \sum_{j=1}^{2}(x_{i2}(t) - x_{j2}(t)) \end{bmatrix}$$
$$\tag{5-5}$$
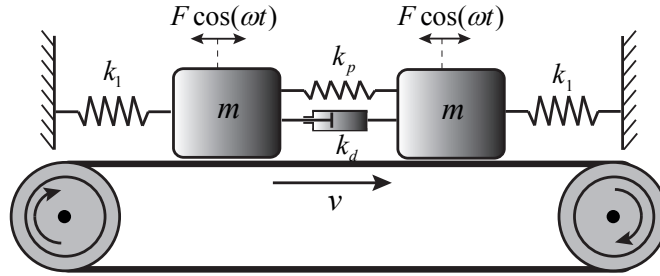
Figure 5-1: The mechanical model under investigation, the origin of the coordinate x is where the spring assumes its natural length.

where $x_{i1}(t), x_{i2}(t) \in \mathbb{R}^2$ denote the position and velocity of the ith block, for $i = 1, 2$, respectively. Here, the function $T(v - x_{i2})$ modeling the friction force, is chosen to be the nonlinear function studied in [98], which is expressed as

$$T(v - x_{i2}(t)) = \alpha_0 \text{sgn}(v - x_{i2}(t)) - \alpha_1(v - x_{i2}(t)) + \alpha_2(v - x_{i2}(t))^3. \tag{5-6}$$

The dynamics of a single uncoupled friction oscillator have been extensively studied in the literature, showing the existence of chaotic aperiodic stick-slip orbits for a parameters $\alpha_0 = 1.5$, $\alpha_1 = 1.5$, $\alpha_2 = 0.45$, $F = 0.5$, $\omega = 1.067$, as also depicted in Figure 5-2, see for more details e.g. [98, 26].

(a)

(b)

Figure 5-2: Time evolution of the state variables of a single system (5-5), (a) position x_{i1} (blue curve) and x_{i3} velocity (black curve). In (b) is shown an aperiodic chaotic trajectory crossing several times the switching manifold Σ.

5.2.1 Effect of dynamic coupling
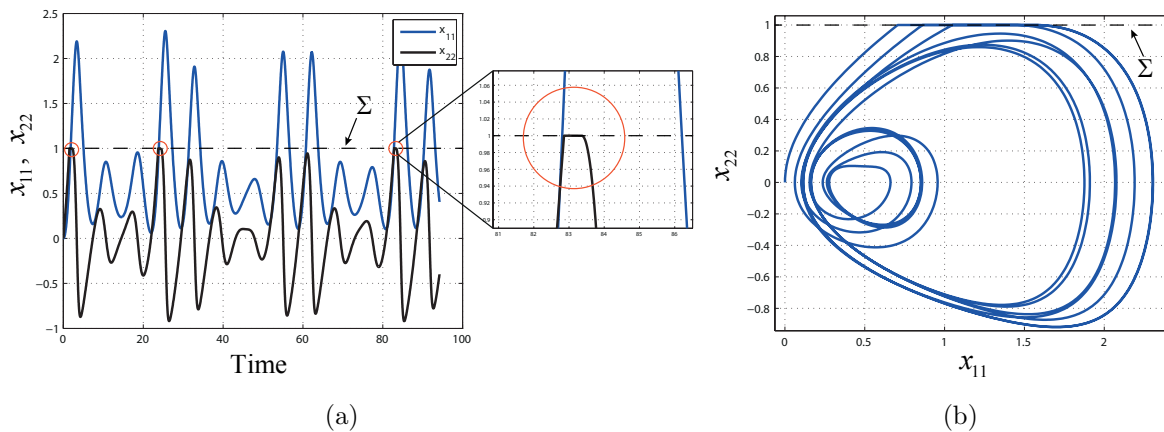
A numerical investigation of the two blocks system interconnected with springs and/or dampers is carried out in order to get information about the synchronous behavior. We follow the methodology explained in Section 5.1. In doing so, we integrate numerically the system equations (5-5) using a continuous approximation of the function $(2/\pi)\tan^{-1}(\varepsilon(v - x_{i2}))$ $(i = 1, 2)$. The initial conditions are selected so that the two blocks move in opposite direction and also considering the fact that when the blocks are stationary their respective velocities are equal to zero. The numerical solutions of the network regarding only the static coupling, $k_p = 1$ and $k_d = 0$ is shown in Figure **5-3**.
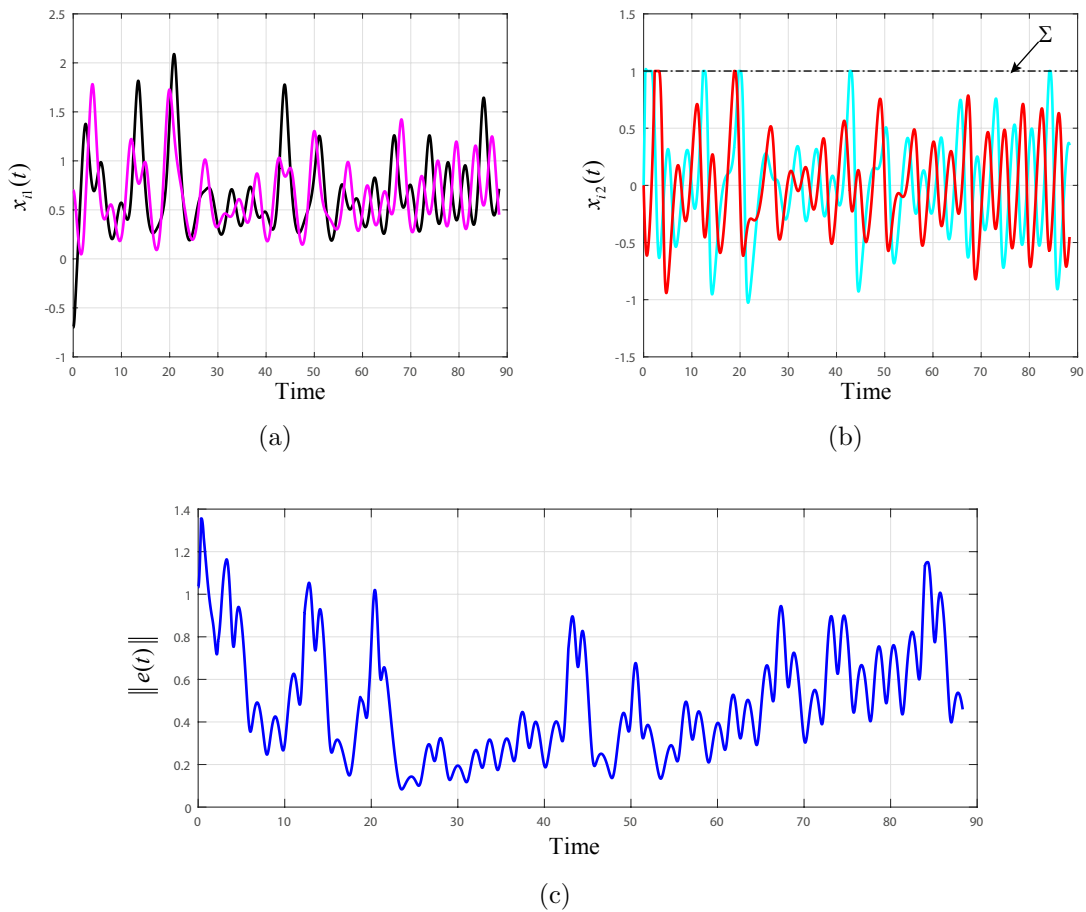

(a)

(b)

(c)

Figure 5-3: Numerical solutions for the positions and velocities of the two blocks: (a) positions x_{11} (black curve), x_{21} (magenta curve) and velocities x_{12} (black curve), x_{22} (cyan curve) (b). The evolution of the average synchronization error is shown in (c).

In Figure **5-3** it is observed the disagreement in the positions and the velocities of the two blocks, making evident the effect of static coupling alone is not enough to guarantee that the two blocks move with the same aperiodic stick-slip behavior. Despite the synchronization error remains relatively small and bounded the network exhibits irregular and unpredictable behavior.

Now, we perform the numerical analysis considering both dynamic and static coupling. Figure **5-4** shows the time evolution of the system trajectories, by setting the coupling parameters $k_p = 1$ and $k_d = 0.5$.
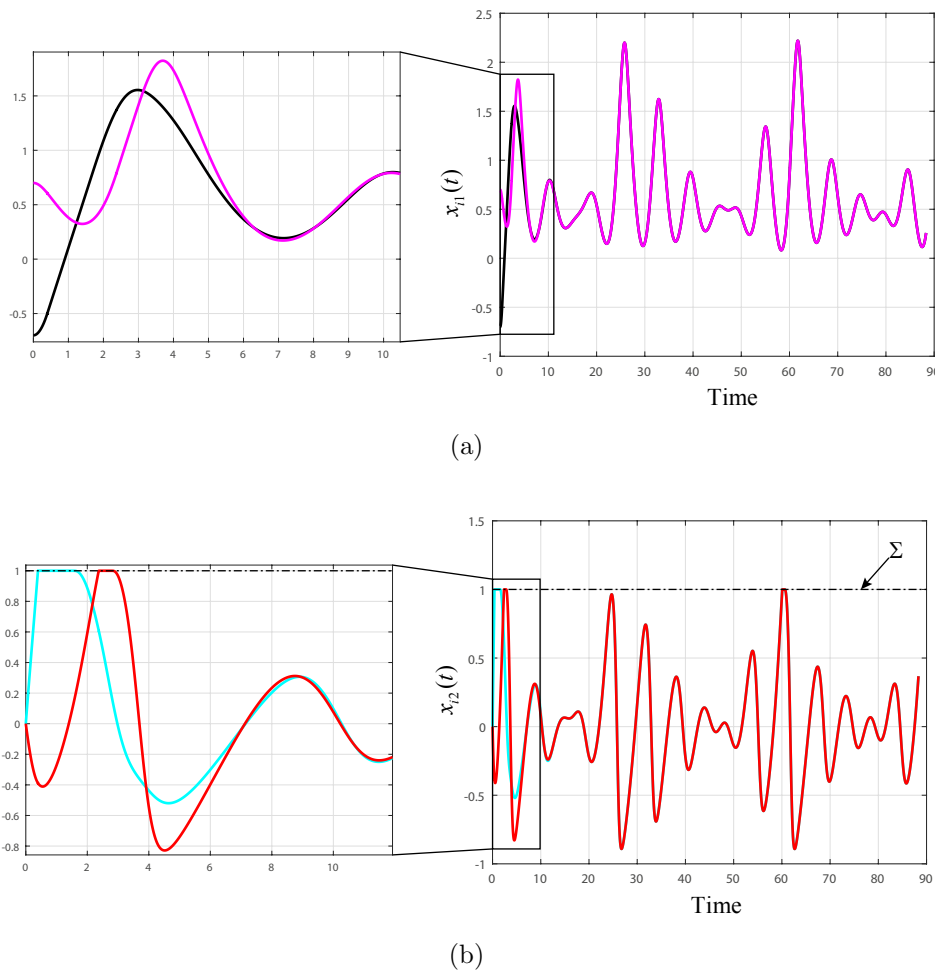

(a)

(b)

Figure 5-4: Time evolution of the systems trajectories: (a) positions x_{11}, x_{21} (magenta and black curves) and (b) velocities x_{12}, x_{22} (black and red curves, respectively)

In Figure **5-4** we can observe that after small transients, the network solutions converge towards a synchronous solution, indicating that a weak damping allows that the two block

enter into a coordinate motion.

The previous numerical analysis allows to guarantee the emergence of a synchronous behavior for the chosen coupling parameters. Thus, in order to estimate the critical parameters k_p and k_d for which the coupled oscillators achieves synchronization, we integrate numerically the network (5-5) over a range of parameters $k_p, k_d, \in [0\,;\,1]$ such that $\|e(t, x)\| = 0$. We integrate the network during a time interval of $[0\ 120]$ where the transients are known to be settled. Moreover, we perform the analysis for two different initial conditions close to each other in order to get local information about the stability of the synchronous network solution in the presence of small perturbations. Then by evaluating the synchronization error (5-4) across the selected grid for each initial condition, we obtain the estimate of the stability charts shown in Figure 5-5.

(a)   (b)
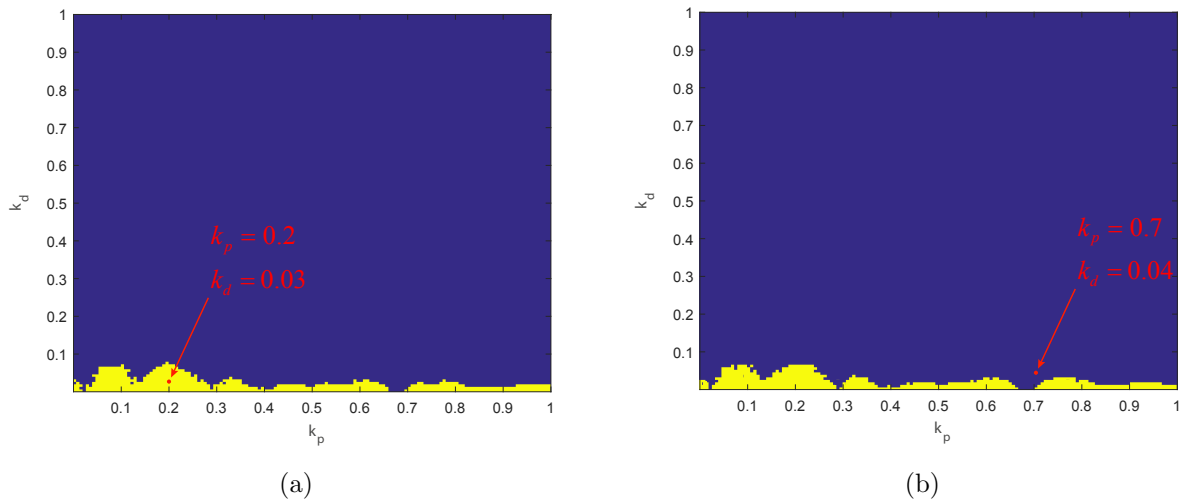
Figure 5-5: Synchronization diagram as a function of the coupling parameters k_p and k_d for two different initial conditions (a) $x^* = [-0.7\ 0\ 0.7\ 0]^T$ and (b) $x^+ = [-0.63\ 0\ 0.63\ 0]^T$. The blue region represents the set of values of k_p and k_d that guarantee synchronization. While yellow areas are regions of no synchronization.

The estimation of the synchronization region in Figure 5-5 shows that for small values of dynamic coupling k_d the network achieves synchronization. Hence, accordingly to the diagram in Figure 5-5 (a), if we choose the point $k_p = 0.2$ and $k_d = 0.03$ in the yellow region, we thus have that the network does not synchronize. The time response of the network is shown in Figure 5-6 (a). If instead we set $k_p = 0.7$ and $k_d = 0.04$ we have

that the network achieves synchronization as expected Figure. **5-6** (b). The synchronization charts do not show remarkable differences when we consider different initial conditions, which suggests that for a small region close to the selected initial conditions, the estimations are valid, as we saw earlier in Figure **5-6**.
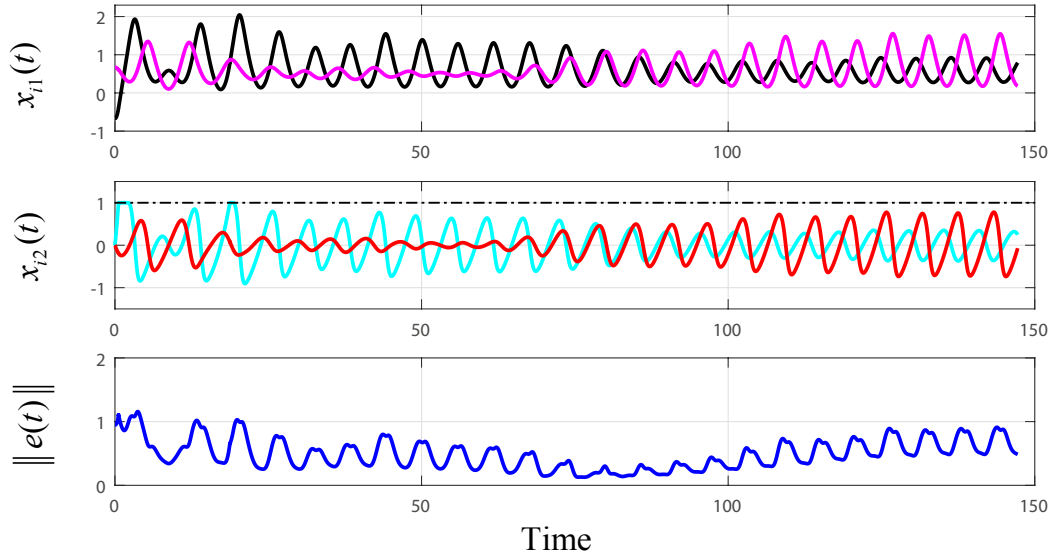
(a)
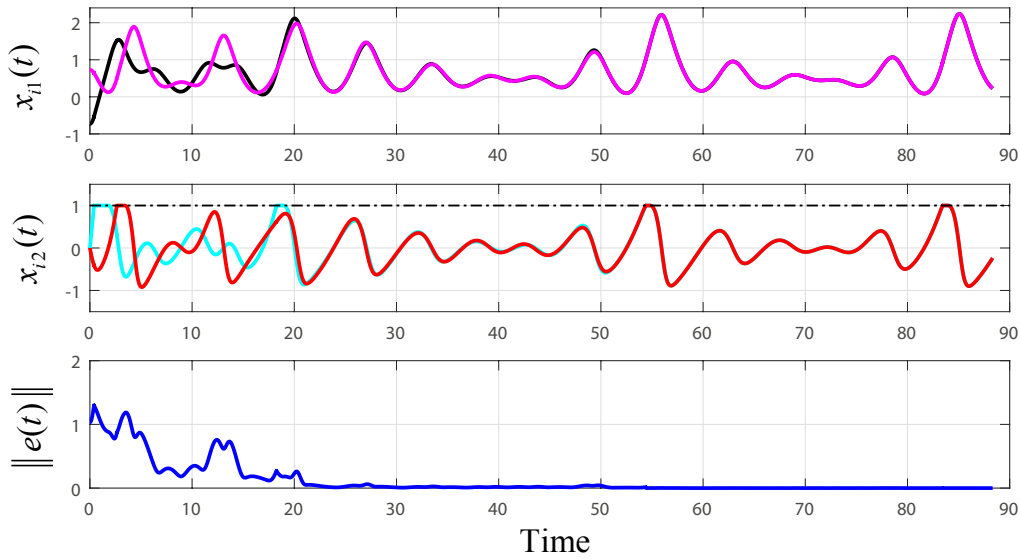
(b)

Figure 5-6: Time response of a network of two chaotic friction oscillators. (a) $k_p = 0.2$, $k_d = 0.03$ and (b) $k_d = 0.04$, $k_p = 0.7$

5.2.2 Effect of regularization

In this subsection, we investigate numerically how the synchronization region changes at varying the regularization parameter ε.
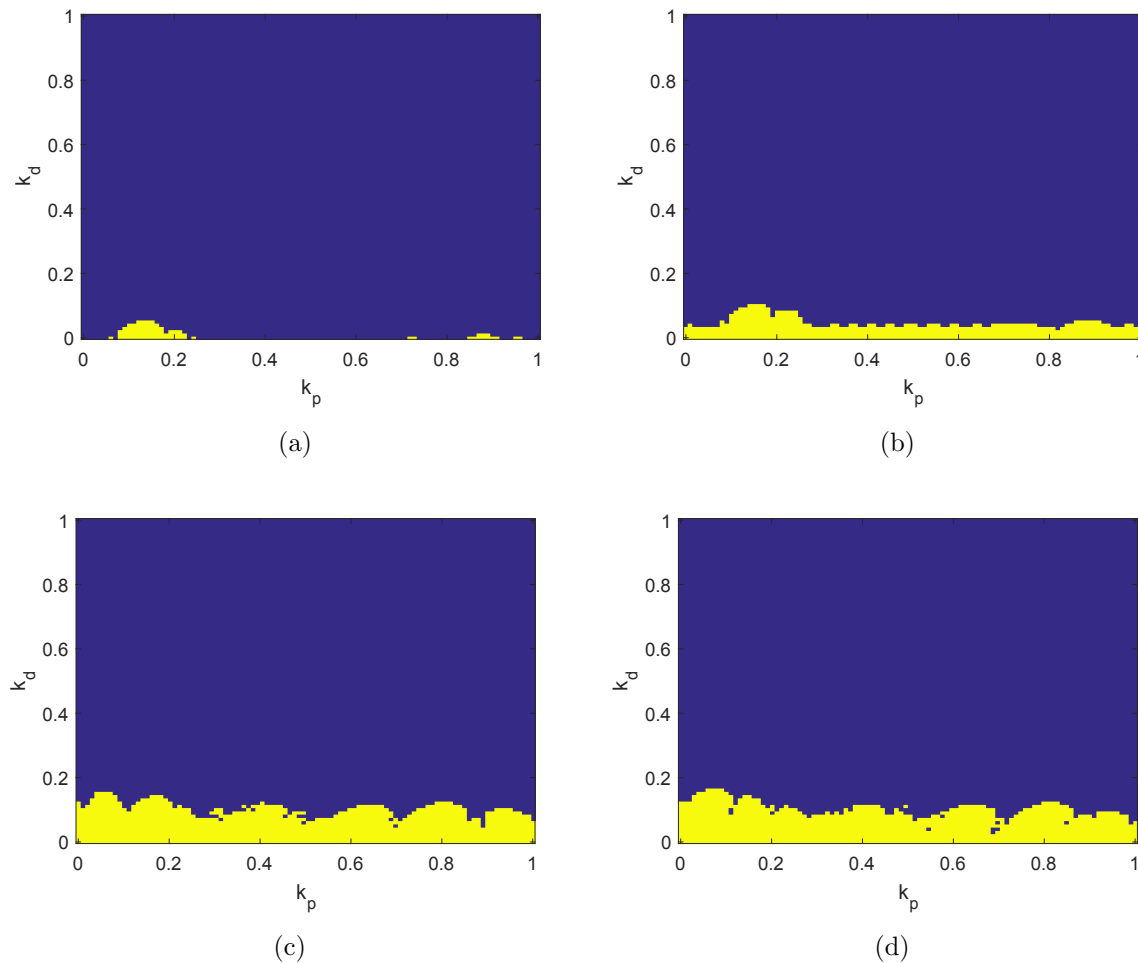
Figure 5-7: Synchronization region at varying the regularization parameter, (a) $\varepsilon = 10$, (b) $\varepsilon = 100$, (c) $\varepsilon = 1000$ and (d) $\varepsilon = 10000$

Note from Figure 5-7 that for values of $\varepsilon > 10^4$ the synchronization diagrams do not present significant changes, suggesting that the values of ε which was selected for the simulations gives accurate enough estimates of the true stability region.

5.3 Synchronization in networks of N dry friction oscillators

So far, we have investigated the synchronization of two coupled oscillators, providing some guidelines to select the coupling strengths. In this section we investigate the influence of the topology in a network of eight friction oscillators coupled dynamically.

5.3.1 Effect of the network topology

We consider a network of eight oscillators under two different architectures: a path graph and an all-to-all graph, known to have opposite connectivity properties.

5.3.1.1 All-to-all network of mechanical oscillators

The network topology is depicted in Figure 5-8, where each oscillators is interconnected by a spring of stiffness k_p and a damper of strength k_d. We start analyzing the system with dynamic coupling, since as we show previously, in the absence of the damping term, the network dynamics are unable to reach synchronization.
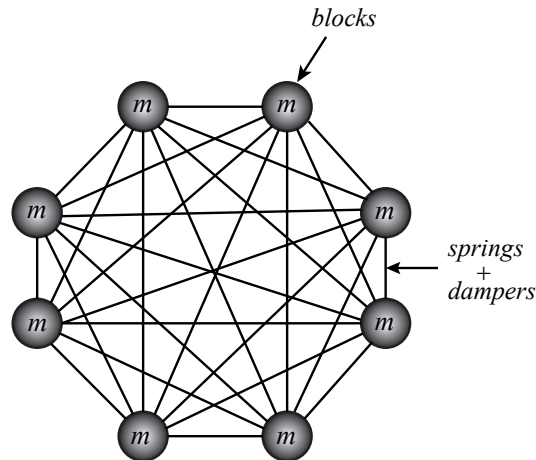
Figure 5-8: Network of 8 mechanical oscillators subjected to dry friction, within a all-to-all topology.

Figure 5-9: Synchronization diagram as a function of the coupling parameters k_p and k_d. The color blue indicates the parameter values that always imply synchronization. The yellow corresponds to the values which lead to no synchronization.

First, we set the parameter $k_p = 0.5$ and $k_d = 0.5$ and compute numerically the system response. The positions and velocities of all masses in the network are shown in Figure **5-10**.
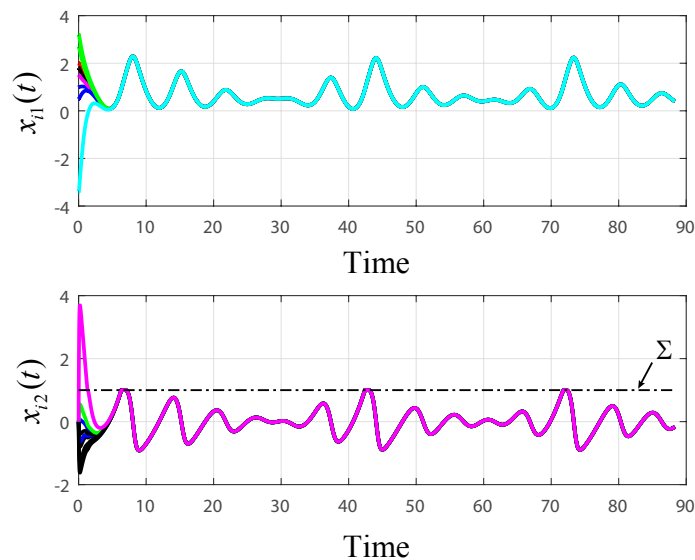
Figure 5-10: Time evolution of the chaotic oscillators network. The black dash-dot line represent the switching manifold.
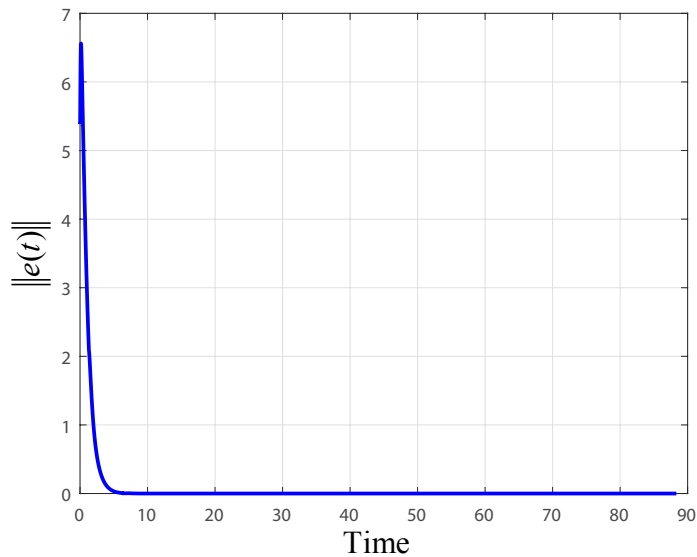
Figure **5-11**: Evolution of the norm of the synchronization error

In Figure **5-9** it is possible to observe that lower dynamic coupling is required for the network to synchronize as long as we increase the number of agents within the all-to-all topology.

5.3.1.2 Path-graph network of mechanical oscillators

We consider next a path graph network composed by 8 blocks connected by springs and dampers, shown in Figure **5-12**.
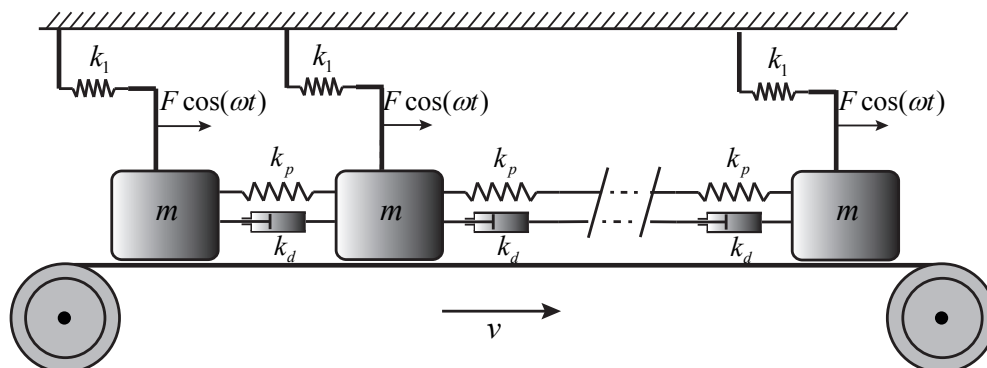
Figure **5-12**: Network of 8 periodically-forced dry friction oscillators

In Figure **5-14** we show that, when considering a path graph topology, the system takes more time to reach synchronization. This is also reflected by the long transient of corresponding error norm, in Figure **5-15**.

(a)   (b)

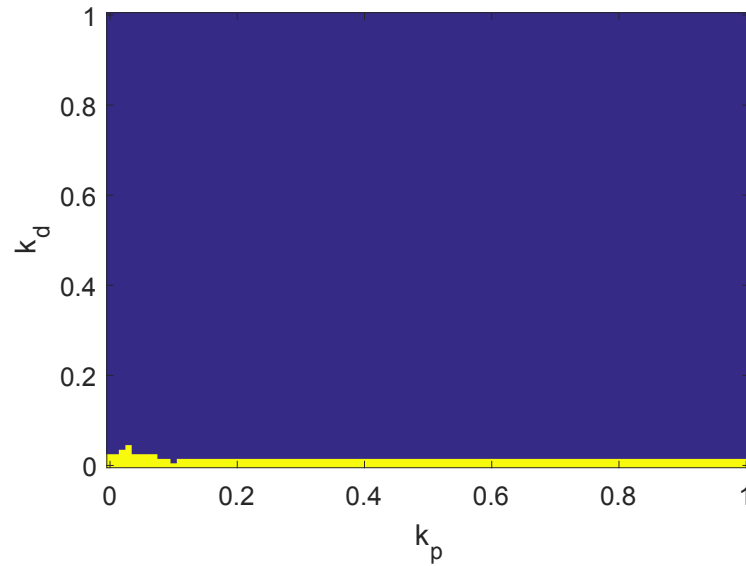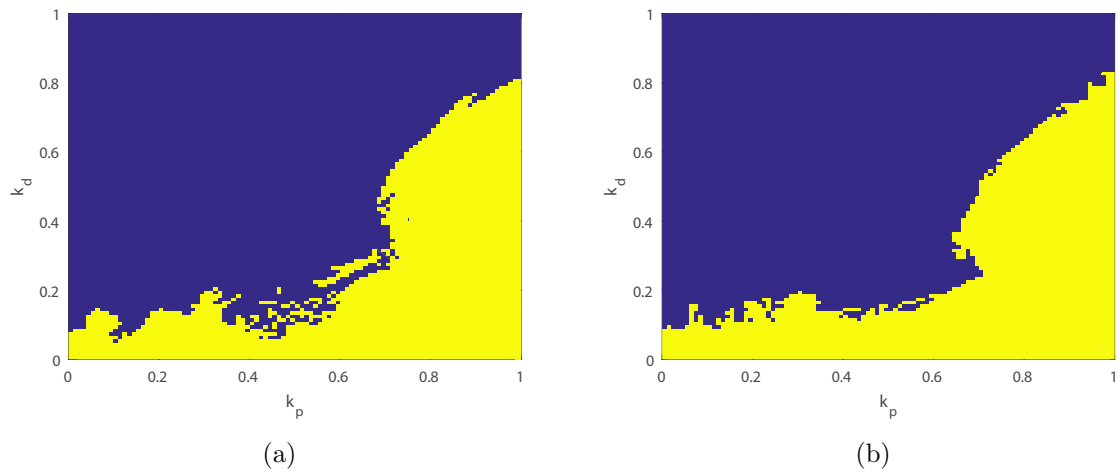**Figure 5-13**: Synchronization diagram as a function of the coupling parameters k_p and k_d. The color blue indicates the parameter values that always imply synchronization. The yellow corresponds to the values which lead to no synchronization.
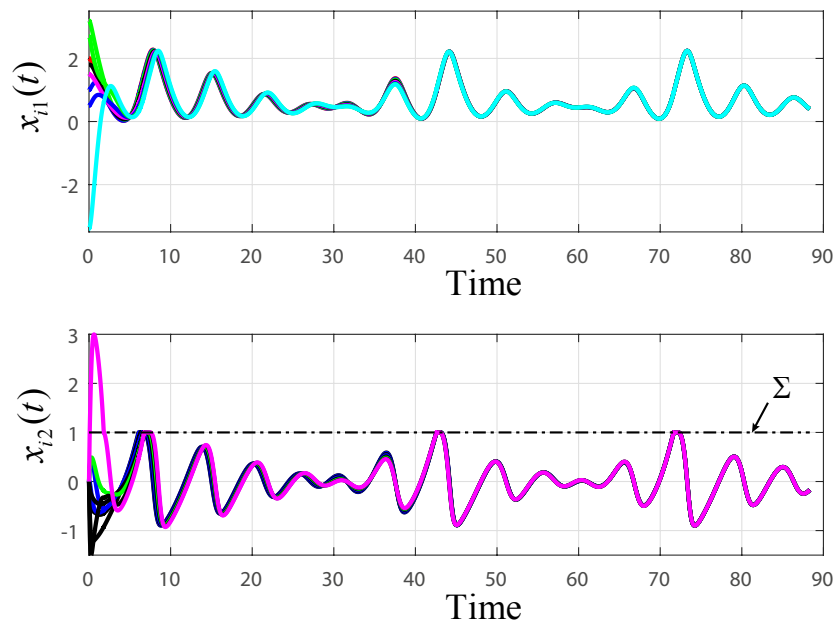
Figure 5-14: Time responses: positions x_{i1} and velocities x_{i2} in a dynamically coupled network of N $= 8$ mechanical oscillators.
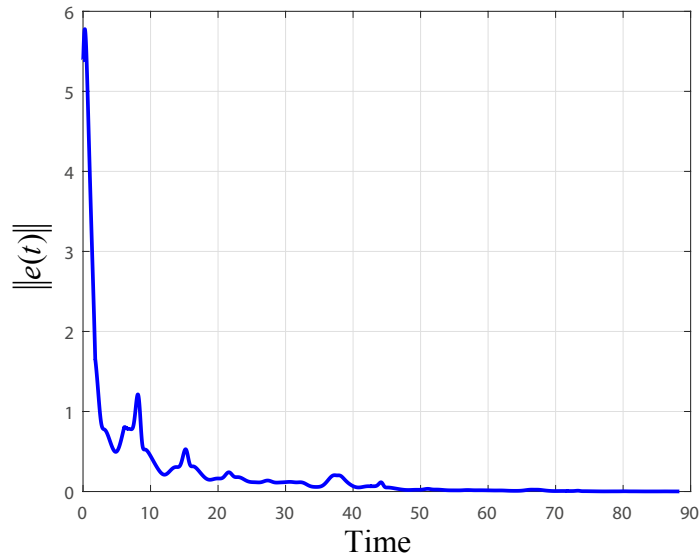
Figure 5-15: Synchronization error norm in a path-graph network of $N = 8$ mechanical
oscillators

Figure **5-13** shows that in the network of friction oscillators within the path-graph topology
as long as the stiffness of the springs is increased more damping is required for the network
to synchronize.

Table 5-1: Initial conditions

Chart	IC	Node 1	Node 2	Node 3	Node 4	Node 5	Node 6	Node 7	Node 8
1	x_{i1}	2	1	3.2	1.8	1.5	0.5	2.7	-3.4
	x_{i2}	0	0	0	0	0	0	0	0
2	x_{i1}	2.5	1.5	2.2	0.6	0	1.4	1.7	-2.4
	x_{i2}	0	0	0	0	0	0	0	0

5.4 Some preliminary results on convergence analysis

In this section we apply contraction analysis of switched systems, revised in Chapter 2 to
the problem of synchronizing networks of friction oscillators. In particular, we derive a set
of conditions that need to be satisfied in order to guarantee synchronization.

5.4.1 Convergence of an all-to-all network of mechanical oscillators

As discussed in Chapter 2, Section 2.3 the virtual system method can be used to study synchronization via contraction. Following this methodology, the synchronization problem is reduced to studying the convergence of a single system in the network which has an extra term representing the interaction with the other agents in the network. In the case of networks of switching systems, the auxiliary system is piecewise-smooth and thus the analysis requires proving convergence of a virtual switching system.

Here, we will use the approach based on contraction analysis via regularization presented in [38], to prove that the virtual system associated to the network of switching systems is contracting which in turns guarantee that the network achieves complete synchronization. To illustrate the methodology, let us consider a network of N friction oscillators described by the equations

$$
\dot{x}_i(t) = \begin{bmatrix} x_{i2}(t) - k_p \sum_{j=1}^{N} (x_{i1}(t) - x_{j1}(t)) \\ -k_1 x_{i1}(t) - \alpha_0 \mathrm{sgn}(v_{rel}) + F\cos(\omega t) - k_d \sum_{j=1}^{N} (x_{i2}(t) - x_{j2}(t)) \end{bmatrix} \tag{5-7}
$$

where $v_{rel} = v - x_{i2}(t)$.

Theorem 5.4.1. *Consider the group of N homogeneous friction oscillators coupled dynamically by springs of stiffness k_p and damping strengths k_d, described in equation (5-7). Let us also assume that the network topology is a complete graph. Then if the coupling strengths are selected so that*

$$
k_p > \frac{1}{N}, \quad k_d > \frac{1}{N}. \tag{5-8}
$$

then, complete synchronization is achieved for the network.

Proof: An auxiliary system for the network model (5-7) can be chosen as

$$
\dot{y} = \begin{bmatrix} y_2 - k_d N y_2 + k_d \sum_{j=1}^{N} x_{j2} \\ -y_1 - a_0 \mathrm{sgn}(\tilde{v}_{rel}) + F\cos(\omega t) - k_p N y_1 + k_p \sum_{j=1}^{N} x_{j1} \end{bmatrix}, \tag{5-9}
$$

where $\tilde{v}_{rel} = v - y_2$. Let us rewrite the auxiliary system into the form (2-2) with

$$
f_1(y) = \begin{bmatrix} y_2 - k_d N y_2 + k_p \sum_{j=1}^{N} x_{j2} \\ -y_1 - a_0 - k_p N y_1 + k_p \sum_{j=1}^{N} x_{j1} + F\cos(\omega t) \end{bmatrix}, \tag{5-10}
$$

$$f_2(y) = \begin{bmatrix} y_2 - k_p N y_2 + k_p \sum\limits_{j=1}^{N} x_{j2} \\ -y_1 + a_0 - k_d N y_1 + k_d \sum\limits_{j=1}^{N} x_{j1} + F\cos(\omega t) \end{bmatrix}. \tag{5-11}$$

and $\Sigma = \{x \in \mathbb{R}^2 : v - y_2 = 0\}$. Then, the Jacobian of the virtual is given by

$$J_1(y) = J_2(y) = \begin{bmatrix} -k_p N & 1 \\ -1 & -k_d N \end{bmatrix} \tag{5-12}$$

Then, from the Theorem 2.3.3 it follows that the trajectories of the nodes in the network (5-7) exponentially converge towards each other if

$$\mu_1(J_1) = \left(\begin{bmatrix} -k_p N & 1 \\ -1 & -k_d N \end{bmatrix} \right) \leq -c_1, \quad c_1 > 0, \tag{5-13}$$
$$= \max\{-k_d N + 1, -k_p N + 1\}.$$

the condition (2-54) reads

$$\mu_1\left([f_1 - f_2] \cdot \nabla h(x)\right) = \left(\begin{bmatrix} 0 \\ 2a_0 \end{bmatrix} \cdot \begin{bmatrix} 0 & -1 \end{bmatrix} \right) = \max\{0, -2a_0\} \tag{5-14}$$

Since $\max\{0, -2a_0\} = 0$, we can conclude that if the coupling strengths are chosen as $k_p > 1/N, k_d > 1/N$, the network of friction oscillators (5-7) achieves complete synchronization.

Note that different norms are appropriate to different problems, similar as different Lyapunov functions have to be carefully chosen when analyzing a nonlinear system. For instance, if we consider a different coupling in (5-7) e.g. $k_p = 0$, the corresponding matrix measures $\mu_1()$, $\mu_2()$, and $\mu_\infty()$ do not allow to verify that system is contracting. In this case, we need to look for an invertible matrix Θ such that

$$\mu\left(\Theta \frac{\partial f}{\partial x}(x)\Theta^{-1} \right) < -\hat{c}, \tag{5-15}$$

which is equivalent to the generalized contraction condition (2-47) with $\Theta(t, x)$ begin a constant matrix.

A methodology to find the metric Θ is an open problem and just few approaches for specific problems allow to find the metric Θ. In [83], the authors introduced a graphical method for checking or imposing contraction using matrix norms. In this method the matrix Θ is constructed by setting some conditions on the elements of the Jacobian matrix that guarantee

that the given system is contracting. Nevertheless, this approach does not apply when the first element of Jacobian matrix is zero.

In the case of piecewise linear systems i.e. when $\frac{\partial f}{\partial x}$ is constant, we can reformulate the results presented in [38] as an LMI problem, so that we can use convex optimization tools to search a candidate for the matrix Θ.

5.5 Summary

In this chapter, we have presented a preliminary study of synchronization in networks of dynamically coupled friction oscillators. The results suggest that dynamic coupling on its own can suffice to guarantee synchronization. Furthermore, synchronization diagrams under different topologies indicate that as long as the connectivity of the network is lower, larger dynamic coupling strength is required for the network achieve synchronization.

Conclusions

In this thesis we discussed a set of relevant analysis and modeling problems for dynamical systems with discontinuous right-hand side, taking coupled friction oscillators as a relevant illustrative case of study. Specifically in Chapter 2 we introduced the linear and nonlinear sliding solutions, together with the method of regularization of PWS dynamical systems. The basic concepts of contraction theory were presented for smooth systems together with an extension to the case of bimodal Filippov systems. A brief introduction of the synchronization problem in coupled networks with diffusive coupling is also provided.

Chapter 3 introduced a numerical tool for computing basins of attraction in Filippov systems. An extension of the simple cell mapping algorithm for planar Filippov systems is presented, detailing how the grid is selected and describing the numerical integration method used for dealing with sliding motions. The effectiveness of the algorithm is shown by computing the basins of attraction of a sliding control problem and a mechanical system with dry friction.

In Chapter 4 is presented the dynamics of two coupled mechanical oscillators subject to dry friction. Nonlinear sliding vector fields are used to model stiction friction force in systems with two discontinuity surfaces. This analysis provides a full characterization of the nonlinear siding dynamics of co-dimension 1 and higher order sliding modes, and more importantly the ambiguity in selecting the nonlinear sliding vector field in the co-dimension 2 surface is resolved by using the regularization approach.

In Chapter 5 the synchronization phenomena were studied numerically in networks of mechanical systems with friction coupled dynamically through different topologies. The effect of

regularization in the synchronization of networks of friction oscillators is discussed. Preliminary results of the convergence of a network of N friction oscillators along with an example validating the obtained results are presented.

Future work will need to address the cumbersome problem of studying convergence analytically in networks of coupled discontinuous systems. This is a challenging problem as coupling discontinuous systems together gives rise to large extended piecewise smooth systems whose dynamics is characterized by many intersecting switching manifolds in state space. Hence, this problem is tightly linked with that of studying and classifying singularities in discontinuous systems of higher order.

Bibliography

[1] James C Alexander and Thomas I Seidman. Sliding modes in intersecting switching surfaces, i: Blending. *Houston J. Math*, 24(3):545–569, 1998.

[2] B Andrievsky. Adaptive synchronization methods for signal transmission on chaotic carriers. *Mathematics and Computers in Simulation*, 58(4):285–293, 2002.

[3] David Angeli. A lyapunov approach to incremental stability properties. *IEEE Transactions on Automatic Control*, 47(3):410–421, 2002.

[4] Brian Armstrong-Helouvry, Pierre Dupont, and Carlos Canudas De Wit. A survey of models, analysis tools and compensation methods for the control of machines with friction. *Automatica*, 30(7):1083–1138, 1994.

[5] Jan Awrejcewicz and Pawel Olejnik. Stick-slip dynamics of a two-degree-of-freedom system. *International Journal of Bifurcation and Chaos*, 13(04):843–861, 2003.

[6] Erin M. Aylward, Pablo A. Parrilo, and Jean-Jacques E. Slotine. Brief paper: Stability and robustness analysis of nonlinear systems via contraction metrics and sos programming. *Automatica*, 44(8):2163–2170, 2008.

[7] Soumitro Banerjee and George C. Verghese. *Nonlinear Phenomena in Power Electronics: Bifurcations, Chaos, Control, and Applications.* IEEE Press, 2001.

[8] P Belardinelli and S Lenci. A first parallel programming approach in basins of attraction computation. *International Journal of Non-Linear Mechanics*, 80:76–81, 2016.

[9] Pierpaolo Belardinelli and Stefano Lenci. An efficient parallel implementation of cell mapping methods for mdof systems. *Nonlinear Dynamics*, 86(4):2279–2290, 2016.

[10] B Besselink, N Van De Wouw, and H Nijmeijer. A semi-analytical study of stick-slip oscillations in drilling systems. *Journal of Computational and Nonlinear Dynamics*, 6(2):021006, 2011.

[11] Martin Biák, Tomás Hanus, and Drahoslava Janovská. Some applications of filippov dynamical systems. *Journal of Computational and Applied Mathematics*, 254:132 – 143, 2013.

[12] Michael Borre and Henryk Flashner. Computation of periodic solutions and their regions of attraction for flexible structures under nonlinear feedback control. *Journal of Vibration and Control*, 2011.

[13] Shane J. Burns and Petri T. Piiroinen. A hybrid scheme for simulation of planar rigid bodies with impacts and friction using impact mappings. *International Journal of Non-Linear Mechanics*, 77:312 – 324, 2015.

[14] R Burridge and Leon Knopoff. Model and theoretical seismicity. *Bulletin of the seismological society of america*, 57(3):341–371, 1967.

[15] P.T. Piiroinen C. Erazo, M. Homer and M. di Bernardo. Dynamic cell-to-cell mapping algorithm for computing basins of attraction in bimodal filippov systems. *Conference on open problems in nonsmooth dynamics, Barcelona, Spain.*, 2016.

[16] T Chelidze, O Lursmanashvili, T Matcharashvili, and M Devidze. Triggering and synchronization of stick slip: waiting times and frequency-energy distribution. *Tectonophysics*, 424(3):139–155, 2006.

[17] T Chelidze, O Lursmanashvili, T Matcharashvili, N Varamashvili, N Zhukova, and E Mepharidze. High-order synchronization of stick–slip process: experiments on spring–slider system. *Nonlinear Dynamics*, 59(1):259–275, 2010.

[18] A Colombo, M Di Bernardo, SJ Hogan, and MR Jeffrey. Bifurcations of piecewise smooth flows: Perspectives, methodologies and open problems. *Physica D: Nonlinear Phenomena*, 241(22):1845–1860, 2012.

[19] A. Colombo and U. Galvanetto. Stable manifolds of saddles in piecewise smooth systems. *Computer Modeling in Engineering and Sciences (CMES)*, 53(3):235–254, 2009.

[20] Marius-F Danca. Synchronization of switch dynamical systems. *International Journal of Bifurcation and Chaos*, 12(08):1813–1826, 2002.

[21] Ashwin P Dani, Soon-Jo Chung, and Seth Hutchinson. Observer design for stochastic nonlinear systems via contraction-based incremental stability. *IEEE Transactions on Automatic Control*, 60(3):700–714, 2015.

[22] Pietro DeLellis, Mario Di Bernardo, Thomas E Gorochowski, and Giovanni Russo. Synchronization and control of complex networks via contraction, adaptation and evolution. *IEEE Circuits and Systems Magazine*, 10(3):64–82, 2010.

[23] R. Delpoux, L. Hetel, and A. Kruszewski. Parameter-dependent relay control: Application to pmsm. *IEEE Transactions on Control Systems Technology*, 23(4):1628–1637, July 2015.

[24] M. di Bernardo, C. J. Budd, A.R. Champneys, and P. Kowalczyk. *Piecewise-smooth Dynamical Systems Theory and Applications*. Springer Verlag, 2008.

[25] Mario di Bernardo, Davide Fiore, Giovanni Russo, and Francesco Scafuti. Convergence, consensus and synchronization of complex networks via contraction theory. In *Complex Systems and Networks*, pages 313–339. Springer, 2016.

[26] Mario di Bernardo, Piotr Kowalczyk, and A Nordmark. Sliding bifurcations: a novel mechanism for the sudden onset of chaos in dry friction oscillators. *International journal of Bifurcation and chaos*, 13(10):2935–2948, 2003.

[27] Mario di Bernardo, Davide Liuzza, and Giovanni Russo. Contraction analysis for a class of non differentiable systems with applications to stability and network synchronization. *SIAM Journal on Control and Optimization*, 52(5):3203–3227, 2014.

[28] L Dieci, C Elia, and L Lopez. A filippov sliding vector field on an attracting co-dimension 2 discontinuity surface, and a limited loss-of-attractivity analysis. *Journal of Differential Equations*, 254(4):1800–1832, 2013.

[29] Luca Dieci and Fabio Difonzo. The moments sliding vector field on the intersection of two manifolds. *Journal of Dynamics and Differential Equations*, pages 1–33, 2015.

[30] Luca Dieci and Luciano Lopez. Sliding motion in filippov differential systems: Theoretical results and a computational approach. *SIAM Journal on Numerical Analysis*, 47(3):2023–2051, 2009.

[31] Luca Dieci and Luciano Lopez. A survey of numerical methods for ivps of odes with discontinuous right-hand side. *Journal of Computational and Applied Mathematics*, 236(16):3967–3991, 2012.

[32] Florian Dorfler and Francesco Bullo. Synchronization and transient stability in power networks and nonuniform kuramoto oscillators. *SIAM Journal on Control and Optimization*, 50(3):1616–1642, 2012.

[33] R Parker Eason and AJ Dick. A parallelized multi-degrees-of-freedom cell mapping method. *Nonlinear Dynamics*, 77(3):467–479, 2014.

[34] C. Erazo, M. Homer, P.T. Piiroinen, and M. di Bernardo. Dynamic cell-to-cell mapping algorithm for computing basins of attraction in bimodal filippov systems. *International journal of Bifurcation and chaos, (submitted)*, 2017.

[35] C. Erazo, E. Lorenzano, M. Homer, and M. di Bernardo. Piecewise smooth analysis of coupled oscillators with nonlinear set-valued function as friction forces. *Nonlinear Dynamics (in preparation)*, 2017.

[36] Jiu Chao Feng. *Reconstruction of chaotic signals with applications to chaos-based communications*. World Scientific, 2008.

[37] A. F. Filippov. *Differential equations with discontinuous righthand sides*, volume 18. Springer Verlag, 1988.

[38] Davide Fiore, S John Hogan, and Mario Di Bernardo. Contraction analysis of switched systems via regularization. *Automatica*, 73:279–288, 2016.

[39] U Galvanetto and SR Bishop. Characterisation of the dynamics of a four-dimensional stick-slip system by a scalar variable. *Chaos, Solitons & Fractals*, 5(11):2171–2179, 1995.

[40] Ugo Galvanetto. Some remarks on the two-block symmetric burridge–knopoff model. *Physics Letters A*, 293(5):251–259, 2002.

[41] Ugo Galvanetto. Computation of the separatrix of basins of attraction in a non-smooth dynamical system. *Physica D: Nonlinear Phenomena*, 237(18):2263–2271, 2008.

[42] Christopher George, Lawrence N. Virgin, and Thomas Witelski. Experimental study of regular and chaotic transients in a non-smooth system. *International Journal of Non-Linear Mechanics*, 81:55 – 64, 2016.

[43] Gergely Gyebrószki and Gábor Csernák. Methods for the quick analysis of micro-chaos. In *Applied Non-Linear Dynamical Systems*, pages 383–395. Springer, 2014.

[44] Philip Hartman. On stability in the large for systems of ordinary differential equations. 13:480–492.

[45] Sira Ramírez Herbertt. On the dynamical sliding mode control of nonlinear systems. *International journal of control*, 57(5):1039–1061, 1993.

[46] L. Hetel, E. Fridman, and T. Fhquet. Variable structure control with generalized relays: A simple convex optimization approach. *IEEE Transactions on Automatic Control*, 60(2):497–502, Feb 2015.

[47] Chieh Su Hsu. *Cell-to-cell mapping: a method of global analysis for nonlinear systems*, volume 64. Springer Verlag, 1987.

[48] Makoto Itoh, Tao Yang, and Leon O Chua. Conditions for impulsive synchronization of chaotic and hyperchaotic systems. *International Journal of Bifurcation and Chaos*, 11(02):551–560, 2001.

[49] Ferenc Jarai Szabo and Neda Zoltan. Earthquake model describes traffic jams caused by imperfect driving styles. *Physica A: Statistical Mechanics and its Applications*, 391(22):5727 – 5738, 2012.

[50] Mike R Jeffrey. Dynamics at a switching intersection: hierarchy, isonomy, and multiple sliding. *SIAM Journal on Applied Dynamical Systems*, 13(3):1082–1105, 2014.

[51] Mike R. Jeffrey. Hidden dynamics in models of discontinuity and switching. *Physica D: Nonlinear Phenomena*, 273:34–45, 2014.

[52] Mike R Jeffrey. On the mathematical basis of solid friction. *Nonlinear Dynamics*, 81(4):1699–1716, 2015.

[53] Mike R Jeffrey. Smoothing tautologies, hidden dynamics, and sigmoid asymptotics for piecewise smooth systems. *Chaos: An Interdisciplinary Journal of Nonlinear Science*, 25(10):103125, 2015.

[54] Mike R Jeffrey. Hidden bifurcations and attractors in nonsmooth dynamical systems. *International Journal of Bifurcation and Chaos*, 26(04):1650068, 2016.

[55] Karl Henrik Johansson. Relay feedback and multivariable control. *PhD Thesis*, 1997.

[56] Jerome Jouffroy and J-JE Slotine. Methodological remarks on contraction theory. In *43rd IEEE Conference on Decision and Control, 2004. CDC.*, volume 3, pages 2537–2543. IEEE, 2004.

[57] Hassan K Khalil. *Noninear Systems.* 2004.

[58] P. Kowalczyk and P.T. Piiroinen. Two-parameter sliding bifurcations of periodic solutions in a dry-friction oscillator. *Physica D: Nonlinear Phenomena*, 237(8):1053 – 1073, 2008.

[59] E Kreuzer and B Lagemann. Cell mappings for multi-degree-of-freedom-systemsÂ—parallel computing in nonlinear dynamics. *Chaos, Solitons & Fractals*, 7(10):1683–1691, 1996.

[60] Christian Kuehn. *Multiple time scale dynamics*, volume 191. Springer, 2015.

[61] RI Leine, DH Van Campen, and WJG Keultjes. Stick-slip whirl interaction in drill-string dynamics. *Journal of Vibration and Acoustics*, 124(2):209–220, 2002.

[62] G.A. Leonov, N.V. Kuznetsov, M.A. Kiseleva, E.P. Solovyeva, and A.M. Zaretskiy. Hidden oscillations in mathematical model of drilling system actuated by induction motor with a wound rotor. *Nonlinear Dynamics*, 77(1-2):277–288, 2014.

[63] DC Lewis. Metric properties of differential equations. *American Journal of Mathematics*, 71(2):294–312, 1949.

[64] Xiaoyang Liu, Jinde Cao, and Wenwu Yu. Filippov systems and quasi-synchronization control for switched networks. *Chaos: An Interdisciplinary Journal of Nonlinear Science*, 22(3):033110, 2012.

[65] Jaume Llibre, Paulo R. da Silva, and Marco A. Teixeira. Regularization of discontinuous vector fields on r^3 via singular perturbation. *Journal of Dynamics and Differential Equations*, 19(2):309–331, 2007.

[66] Winfried Lohmiller and Jean-Jacques E Slotine. On contraction analysis for non-linear systems. *Automatica*, 34(6):683–696, 1998.

[67] Winfried Lohmiller and Jean-Jacques E Slotine. Nonlinear process control using contraction theory. *AIChE journal*, 46(3):588–596, 2000.

[68] David Lovelock and Hanno Rund. *Tensors, differential forms, and variational principles*. Courier Corporation, 1989.

[69] Chuen Kit Luk, Graziano Chesi, and Dongkun Han. Guaranteed estimates of the domain of attraction for a class of hybrid systems. In *IEEE 52nd Annual Conference on Decision and Control (CDC), 2013*, pages 2024–2029. IEEE, 2013.

[70] Joanna F Mason and Petri T Piiroinen. Interactions between global and grazing bifurcations in an impacting system. *Chaos: An Interdisciplinary Journal of Nonlinear Science*, 21(1):013113, 2011.

[71] Joanna F. Mason, Petri T. Piiroinen, R. Eddie Wilson, and Martin E. Homer. Basins of attraction in nonsmooth models of gear rattle. *International Journal of Bifurcation and Chaos*, 19(01):203–224, 2009.

[72] I. Merillas. *Modeling and numerical study of nonsmooth dynamical systems*. PhD thesis, Dept. Matematica Aplicada IV, Universitat Politecnica de Catalunya, 2006.

[73] N Mihajlovic, N Van de Wouw, MPM Hendriks, and H Nijmeijer. Friction-induced limit cycling in flexible rotor systems: An experimental drill-string set-up. *Nonlinear Dynamics*, 46(3):273–291, 2006.

[74] Henk Nijmeijer and Alejandro Rodriguez-Angeles. *Synchronization of mechanical systems*, volume 46. World Scientific, 2003.

[75] Douglas D Novaes and Mike R Jeffrey. Regularization of hidden dynamics in piecewise smooth flows. *Journal of Differential Equations*, 259(9):4615–4633, 2015.

[76] M Oestreich, N Hinrichs, and K Popp. Bifurcation and stability analysis for a nonsmooth friction oscillator. *Archive of Applied Mechanics*, 66(5):301–314, 1996.

[77] Henrik Olsson, Karl J Åström, C Canudas De Wit, Magnus Gäfvert, and Pablo Lischinsky. Friction models and friction compensation. *European journal of control*, 4(3):176–195, 1998.

[78] DeLellis Pietro, Di Bernardo Mario, and Liuzza Davide. Convergence and synchronization in heterogeneous networks of smooth and piecewise smooth systems. *Automatica*, 56:1 – 11, 2015.

[79] Petri T. Piiroinen and Yuri A. Kuznetsov. An event-driven method to simulate fil-ippov systems with accurate computing of sliding motions. *ACM Transactions on Mathematical Software (TOMS)*, 34(3):13, 2008.

[80] Wei Ren and Randal W Beard. Consensus seeking in multiagent systems under dy-namically changing interaction topologies. *IEEE Transactions on automatic control*, 50(5):655–661, 2005.

[81] Alejandro Rodriguez-Angeles and Henk Nijmeijer. Mutual synchronization of robots via estimated state feedback: a cooperative approach. *IEEE Transactions on control systems technology*, 12(4):542–554, 2004.

[82] Giovanni Russo and Mario di Bernardo. On contraction of piecewise smooth dynamical systems. *IFAC Proceedings Volumes*, 44(1):13299–13304, 2011.

[83] Giovanni Russo, Mario di Bernardo, and Jean-Jacques E Slotine. A graphical approach to prove contraction of nonlinear circuits and systems. *IEEE Transactions on Circuits and Systems I: Regular Papers*, 58(2):336–348, 2011.

[84] Ilya Shmulevich, Edward R Dougherty, and Wei Zhang. From boolean to probabilistic boolean networks as models of genetic regulatory networks. *Proceedings of the IEEE*, 90(11):1778–1792, 2002.

[85] J Sotomayor and MA Teixeira. Regularization of discontinuous vector fields. In *International Conference on Differential Equations, Lisboa*, volume 207, page 223, 1996.

[86] Jos F Sturm. Using sedumi 1.02, a matlab toolbox for optimization over symmetric cones. *Optimization methods and software*, 11(1-4):625–653, 1999.

[87] Jian-Qiao Sun and Albert CJ Luo. *Global Analysis of Nonlinear Dynamics*, volume 2. Springer Verlag, 2012.

[88] Mukund Thattai and Alexander Van Oudenaarden. Intrinsic noise in gene regulatory networks. *Proceedings of the National Academy of Sciences*, 98(15):8614–8619, 2001.

[89] DC Tsobgni-Fozap, A Kenfack-Jiotsa, GI Koumene-Taffo, and TC Kofané. Effect of coupling, synchronization of chaos and stick-slip motion in two mutually coupled dynamical systems. *Nonlinear Dynamics*, 78(2):1159–1177, 2014.

[90] V. Utkin. Variable structure systems with sliding modes. *IEEE Transactions on Automatic Control*, 22(2):212–222, 1977.

[91] Vadim Utkin, Jürgen Guldner, and Jingxin Shi. *Sliding mode control in electromechanical systems*, volume 34. CRC press, 2009.

[92] BL Van de Vrande, DH Van Campen, and A De Kraker. An approximate analysis of dry-friction-induced stick-slip vibrations by a smoothing procedure. *Nonlinear Dynamics*, 19(2):159–171, 1999.

[93] van de Wouw Nathan and Pavlov A. Tracking and synchronisation for a class of pwa systems. *Automatica*, 44(11):2909–2915, 2008.

[94] JAW Van Der Spek, CAL De Hoon, A De Kraker, and DH Van Campen. Application of cell mapping methods to a discontinuous dynamic system. *Nonlinear Dynamics*, 6(1):87–99, 1994.

[95] Josephus Antonius Wilhelmus Van der Spek. *Cell mapping methods: modifications and extensions*. PhD thesis, Technische Universiteit Eindhoven, 1994.

[96] L.N. Virgin and C.J. Begley. Grazing bifurcations and basins of attraction in an impact-friction oscillator. *Physica D: Nonlinear Phenomena*, 130(1Â–2):43 – 57, 1999.

[97] Wei Wang and Jean-Jacques E Slotine. On partial contraction analysis for coupled nonlinear oscillators. *Biological cybernetics*, 92(1):38–53, 2003.

[98] Yutaka Yoshitake and Atsuo Sueoka. Dry friction. *Applied nonlinear dynamics and chaos of mechanical systems with discontinuities*, 28:237, 2000.

[99] W. Yu, G. Chen, M. Cao, and J. Kurths. Second-order consensus for multiagent systems with directed topologies and nonlinear dynamics. *IEEE Transactions on Systems, Man, and Cybernetics, Part B (Cybernetics)*, 40(3):881–891, 2010.

[100] Huaguang Zhang, Yongxiang Zhang, and Guanwei Luo. Basins of coexisting multidimensional tori in a vibro-impact system. *Nonlinear Dynamics*, 79(3):2177–2185, 2015.

[101] Jun Zhao, David J Hill, and Tao Liu. Synchronization of complex dynamical networks with switching topology: A switched system point of view. *Automatica*, 45(11):2502–2511, 2009.